Water-equivalence of phantom materials in proton and carbon-ion dosimetry

by

Ana Mónica Ferreira De Almeida Lourenço

PhD Thesis
Submitted for the degree of
Doctor of Philosophy
from
University College London

Supervisors: Gary Royle
Hugo Palmans

Department of Medical Physics & Biomedical Engineering

2017

2

Declaration

I, Ana Mónica Ferreira De Almeida Lourenço, confirm that the work presented in this thesis was carried out by myself, except where explicitly stated. The work presented in this thesis was conducted from September 2013 to September 2016. The experiments detailed in Chapters 2-5 took place between February 2014 and September 2015 at the PTC Czech Proton Therapy Centre (Czech Republic), the Clatterbridge Cancer Centre (UK), the Gunma University Heavy Ion Medical Center (Japan) and the Trento Proton Therapy Center (Italy). Experiments were performed with the assistance of local contacts and the National Physical Laboratory (UK) staff. The water-equivalent plastics evaluated in Chapters 3 and 5 were designed by me and produced in collaboration with St Bartholomew's Hospital (UK). Geant4 simulations in Chapter 3 were conducted by David Shipley under my guidance.

....

4

Abstract

The growing interest in light-ion therapy in recent decades has led to a need for accurate dosimetry. At present, a calibration service based on a primary-standard calorimeter for the direct determination of absorbed dose to water for light-ion beams does not exist. Furthermore, the water-equivalent plastics currently used for light-ion beam dosimetry were designed to be used with high-energy photon and electron beams thus energy- and depth-dependent correction factors need to be applied to measurements of dose to water in plastic phantoms.

The first portable graphite calorimeter for light-ion beams was built at the National Physical Laboratory (NPL), UK. In this work, fluence correction factors required to convert absorbed dose to graphite, measured by graphite calorimetry, to absorbed dose to water were determined experimentally and compared with Monte Carlo simulations in proton and carbon-ion beams. Fluence corrections in high-energy light-ion beams could amount to as much as 4% and therefore need to be considered.

Novel water-equivalent plastics were specifically designed for light-ion beams and three test compositions were produced and experimentally characterised in proton and carbon-ion beams. Commercially available plastics were also simulated for comparison with the plastics tested experimentally. Experimental data showed that each of the novel water-equivalent plastics showed measurements of dose similar to water to within 1% across all depths. Monte Carlo simulations showed that one of the novel plastics had superior water-equivalence to commercially available plastics in carbon-ion beams, with a maximum fluence correction of 0.5%.

The accuracy of particle transport in the FLUKA Monte Carlo code for proton beams was assessed by performing a Fano cavity test. FLUKA was found to pass this test to within 0.1%. Ion-chamber perturbation factors were also computed for the PTW 34070 Bragg peak chamber typically used in clinical proton beams.

6

Acknowledgements

I would sincerely like to thank my supervisors, without whom this work would not have been possible. Their dedication, expertise, understanding and patience have added considerably to my project. I have the utmost respect for them and they are an inspiration to me as scientists and human beings. To Gary Royle (UCL) for giving me this unique opportunity, his clear guidance, generosity and great encouragement. To Hugo Palmans (NPL and MedAustron) for the many hours discussing dosimetry at NPL, through e-mail and Skype. I feel very fortunate and honoured to have worked with him, his great knowledge has enabled me to make the most of my project.

A very special thanks goes to Russell Thomas (NPL) for all his support in the experiments - his expertise definitely made all the difference in obtaining good data in the very limited beam time available to us. Thank you for being a good friend over the course of these three long years, who always knew how to lift my spirits with his enthusiasm. Also, thank you for the many fun hours we spent in the van on our way to the experiments, or in the pub.

I am also very grateful to Nigel Wellock (St Bartholomew's Hospital) for kindly helping me in the production of the plastic materials and for answering my many questions.

During the duration of my PhD, I was extremely lucky to collaborate with fantastic people from different research groups and backgrounds. I would like to thank the staff at the Clatterbridge Cancer Centre (UK), the PTC Czech Proton Therapy Centre (Czech Republic), the Trento Proton Therapy Center (Italy) and the Gunma University Heavy Ion Medical Center (Japan). A special thanks goes to Andrzej Kacperek (CCC), Marco Schwarz (TPTC), Michael Homer (NPL), Nigel Lee (NPL), Séverine Rossomme (Université Catholique de Louvain), Tatsuaki Kanai (GHMC) and Vladimir Vondracek (PTC Czech) for their assistance during experiments.

I would like to acknowledge David Shipley (NPL), Hugo Bouchard (Université de Montreal) and Sebastian Galer (NPL) for technical assistance with Monte Carlo simulations and always being willing to discuss Monte Carlo issues.

To everyone in the Radiation Dosimetry group at NPL, particularly to Simon Duane for useful discussions and Lauren Petrie for her friendship. Thank you all for all the good times, either in the office, kitchen, pub or outdoors!

Also I would like to acknowledge the use of the UCL Legion High Performance Computing Facility (Legion@UCL), and associated support services, in the completion of this work. I am also very grateful to the FLUKA developers and the FLUKA mailing list which was of great support with questions I had regarding the FLUKA code.

In addition, I would like to gratefully acknowledge the financial support received from NPL and UCL for me to carry out my PhD studies.

I also would like to express my gratitude to everyone who made my stay in UCL so special and rewarding, there are no words to describe how happy and proud I am to have met them and to have had the opportunity to contact and work with them. A special thanks to my friends Andria Doolan, Anna Zamir, Chiaki Crews, Dario Basta, George Randall, Ireneos Drakos, Marco Endrizzi, Nadia Konstantina Violaki and Paul Doolan.

A very emotional thanks to my #protongirls, Catarina Veiga, Reem Al-Samarraie and Esther Bär, who were always there to go for a coffee or drink, and who made this an amazing time of my life.

A big thank to my lifetime Portuguese friends in London, Andreia Silva (Dédé) and Sara Reis (Sásá) for being with me in the *Fantastic 3*, to António Ferreira (Toninho) for being like a brother to me, and Patrícia Araújo (Patyzinha) for always being there.

To Joanna Ridge and all her lovely family and her friends in the church who always prayed for me and gave me unconditional support.

To my amazing friends Ana Andrade, Ângelo Jesus, Inês Carreiras, Maria Correia, Mariana Bagulho and Rita Bagulho for their lifetime friendship and love. I am truly blessed to have them in my life, making me feel like I had never left.

Also to Danaki for looking after me in the last years, for cheering me up in the most difficult moments, for challenging me everyday and for being my family in London.

My most special thanks goes to my family for their unconditional love, support, generosity and enthusiasm and for fully supporting me and cheering for my success: my aunty and cousin, Goretty and Rafa, my grandmother Maria, my sisters Júlia and Cátia and my parents Júlio and Maria.

for Maria

Contents

List of Figures

List of Tables

List of Abbreviations

AM Analytical model.

BG Bragg-Gray.

CCC Clatterbridge Cancer Centre.
CPE Charged particle equilibrium.
CSDA Continuous slowing down approximation.

exp experiments.

FLUC Energy loss fluctuations.

GHMC Gunma University Heavy Ion Medical Center.

IAEA International Atomic Energy Agency.
ICRU International Commission on Radiation Units.

MC Monte Carlo.
MCS Multiple Coulomb scattering.

NUC Nuclear reactions.

PEANUT Pre-Equilibrium Approach to Nuclear Thermalization.
PMS Phenolic microspheres.
PPRIG Proton Physics Research Implementation Group.
PTC Czech PTC Czech Proton Therapy Centre.

SA	Spencer-Attix.
SDD	Source-to-detector distance.
SSD	Source-to-surface distance.
TPTC	Trento Proton Therapy Center.
TRS	Technical Report Series.
WET	Water-equivalent thickness.

Published work

The work presented in this thesis resulted in the following peer-reviewed journal papers:

- **A. Lourenço**, R. Thomas, H. Bouchard, A. Kacperek, V. Vondracek, G. Royle, and H. Palmans, "Experimental and Monte Carlo studies of fluence corrections for graphite calorimetry in low- and high-energy clinical proton beams", Medical Physics **43**, 4122-32 (2016)
- **A. Lourenço**, N. Wellock, R. Thomas, M. Homer, H. Bouchard, T. Kanai, N. MacDougall, G. Royle, and H. Palmans, "Theoretical and experimental characterization of novel water-equivalent plastics in clinical high-energy carbon-ion beams", Physics in Medicine and Biology **61**, 7623-38 (2016)
- **A. Lourenço**, R. Thomas, M. Homer, H. Bouchard, S. Rossomme, J. Renaud, T. Kanai, G. Royle, and H. Palmans, "Fluence correction factor for graphite calorimetry in a clinical high-energy carbon-ion beam" (currently under review in Physics in Medicine and Biology)
- **A. Lourenço**, D. Shipley, N. Wellock, R. Thomas, H. Bouchard, A. Kacperek, F. Fracchiolla, S. Lorentini, M. Schwarz, N. MacDougall, G. Royle, and H. Palmans, "Evaluation of the water-equivalence of plastic materials in low- and high-energy clinical proton beams" (currently under review in Physics in Medicine and Biology)

Oral presentations

- **A. M. Lourenço**, G. Royle, H. Bouchard and H. Palmans, "Water and tissue equivalent phantom materials for clinical proton beam dosimetry", UK Monte Carlo User Group Meeting (MCNEG) (Liverpool, UK, 2014)
- **A. M. Lourenço**, G. Royle and H. Palmans, "Water and tissue equivalent

phantom materials for clinical proton beam dosimetry", NPL PPRIG Proton Therapy Physics Workshop (London, UK, 2014)

- **A. M. Lourenço**, G. Royle, H. Bouchard and H. Palmans, "Fluence correction factors for non-water phantoms in high energy proton and carbon beams", Monte Carlo User Group Meeting (London, UK, 2015)
- **A. Lourenço**, G. Royle, and H. Palmans, "Evaluation of the water-equivalence of plastic materials in carbon-ion radiotherapy", Proceedings of the 55th Annual Conference Particle Therapy Co-Operative Group (PTCOG, Prague, Czech Republic, 2016)
- **A. Lourenço**, R. Thomas, H. Bouchard, A. Kacperek, V. Vondracek, G. Royle, and H. Palmans, "SU-D-BRC-06: Experimental and Monte Carlo Studies of Fluence Corrections for Graphite Calorimetry in Proton Therapy", Medical Physics **43**, 3337-3337 (AAPM, Washington DC, USA, 2016)

Poster presentations

- **A. M. Lourenço**, R. A. S. Thomas, N. Wellock, H. Bouchard, N. MacDougall, G. Royle, and H. Palmans, "Fluence correction factors for non-water phantom materials in clinical light-ion beams", Proceedings to the 54th Annual Meeting for the Particle Therapy Cooperative Group (PTCOG) and the 2nd Annual Meeting of PTCOG – North America, International Journal of Particle Therapy **2**, 316-317 (San Diego, USA, 2015)

I have also contributed to the following peer-reviewed journal papers:

- C. Veiga, J. McClelland, S. Moinuddin, **A. Lourenço**, K. Ricketts, J. Annkah, M. Modat, S. Ourselin, D. D'Souza, and G. Royle, "Toward adaptive radiotherapy for head and neck patients: feasibility study on using CT-to-CBCT deformable registration for "dose of the day" calculations", Medical Physics **41**, 031703 (2014)
- C. Veiga, **A. Lourenço**, S. Moinuddin, M. van Herk, M. Modat, S. Ourselin, D. D'Souza, G. Royle, and J. R. McClelland, "Toward adaptive radiotherapy for head and neck patients: uncertainties in dose warping due to the choice of deformable registration algorithm", Medical Physics **42**, 760-769 (2015)
- C. Veiga, J. Alshaikhi, R. Amos, **A. M. Lourenço**, M. Modat, S. Ourselin, G.

Royle, and J. R. McClelland, "CBCT and deformable registration based "dose of the day" calculations for adaptive proton therapy", International Journal of Particle Therapy **2**, 404-414 (2015)

- R. Ahmad, G. Royle, **A. Lourenço**, M. Schwarz, F. Fracchiolla, and K. Ricketts, "Investigation into the effects of high-Z nano materials in proton therapy", Physics in Medicine and Biology **61**, 4537-50 (2016)

Conference abstracts

- **A. M. Lourenço**, C. Veiga, G. Royle, and J. McClelland, "Dose remapping and summation for head and neck adaptive radiotherapy applications", NPL PPRIG Proton Therapy Physics Workshop (London, UK, 2014)
- D.R. Shipley, **A. M. Lourenço**, and H. Palmans, "OC-0159: Fluence correction factors for graphite calorimetry in clinical proton beams using Geant4", Radiotherapy & Oncology **115** (Suppl. 1), S77–S78
- R. Thomas, J. De Pooter, A. Krauss, N. Durny, S. Rossomme,A. Kacperek, V. Vondracek, L. Petrie, **A. Lourenço**, N.Lee, D. Shipley, and H. Palmans, "Calorimetry, ionometry and solid state dosimetry in scanned light-ion beams", Physica Medica **31**, e50 (2015)
- R. Ahmad, G. Royle, **A. M. Lourenço**, M. Schwarz, F. Francesco, and K. Ricketts, "Novel method to quantify physical dose enhancement due to gold nanoparticles in proton therapy", Proceedings of the 55th Annual Conference Particle Therapy Co-Operative Group (PTCOG, Prague, Czech Republic, 2016)

Chapter 1

Introduction

1.1 Context of the research project

Light-ion therapy is a form of cancer treatment that uses light-ion radiation. Light-ions have physical advantages in cancer therapy due to their finite range and the dose maximum near the end of the range. Figure 1.1 represents a comparison between dose distributions from a 175 MeV proton beam and a 6 MV x-ray beam. The burst of energy deposited by the end of the proton path is called the Bragg peak and, by controlling the energy of the beam, the Bragg peak depth can be adjusted to take place exactly within the tumour. This allows an optimal conformation of the maximum dose to the tumour with lower doses to the surrounding tissues in comparison with conventional radiotherapy. In light-ion beams the rate at which the projectiles lose energy by projectile-electron collisions increases as they slow down (at the Bragg peak region) because more energy is transferred to the electrons the longer the projectiles are in their vicinity [1]. Different energies of the incident proton beam are combined (modulated beam) in order to treat tumours with larger volumes.

Figure 1.2 represents depth-dose curves for a proton beam (left panel) and for a carbon-ion beam (right panel). Carbon-ion beams have a higher dose gradient at the Bragg peak than protons thus their peak is narrower and the falloff of the peak is steeper. Furthermore, carbon-ion beam depth-dose profiles are characterized by a dose tail behind the Bragg peak, known as fragmentation tail, which is due to the production of secondary fragments with larger ranges [3]. The fragmentation tail is a disadvantage in healthy tissue sparing.

Currently, no primary standards for the direct determination of absorbed dose to water in light-ion beams exist. Therefore, ionization chamber dosimetry under reference conditions is performed, where chambers are calibrated in terms of absorbed dose to water for a cobalt-60 beam [4]. The estimated uncertainty of the calibration coefficient is of the order of 0.6% plus other related uncertainties, and the uncertainty related to the beam quality correction factor, k_{Q}, is in the range of 1.7%-3.2%. These uncertainties combined give a total uncertainty for ionization chamber dosimetry within a range of 3.0%-3.4% for heavy-ion beams and 2.0%-2.3% for proton beams, while for a high-energy photon beam the uncertainty is 1.5%. [4]. Ionization chamber perturbation factors are assumed to be unity within an uncertainty in all dosimetry protocols for light-ion beams [5], which contribute to the larger uncertainty in k_{Q}. Ionization chamber perturbation factors are correction factors that account for the perturbation by the presence of the ionization chamber in the medium. They include the perturbation of the charged particle fluence due to the presence of an air cavity (p_{cav}) and the non-water equivalence of the ionization chamber wall (p_{wall}) [5]. Palmans *et al.* [6] showed that experimental perturbation corrections could amount to 0.5% to 1% for proton beams. Moreover, Palmans and Verhaegen [7] and Verhaegen and Palmans [8] showed that secondary electron perturbations could be of the order of 1% and suggested that perturbation effects caused by secondary particles from non-elastic nuclear interactions could be relevant.

The recommended primary standard instruments to measure absorbed dose are

Figure 1.1: Comparison between dose distributions from a 175 MeV proton beam (dashed-dot line), a modulated proton beam (solid line) and a 6 MV x-ray beam (dashed line) in water [2].

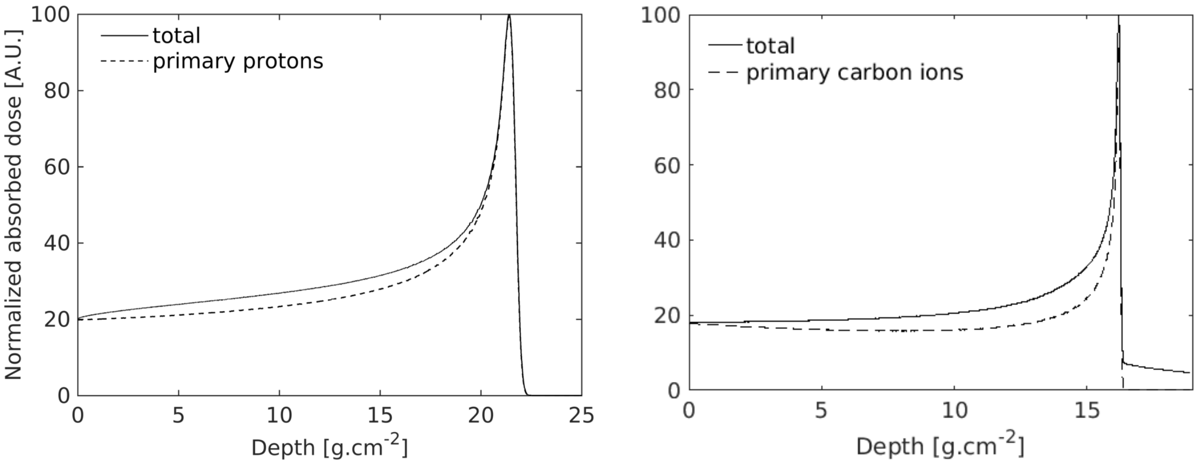

(a) (b)

Figure 1.2: Total and primary particles depth-dose curves in water for (a) a 180 MeV proton beam and (b) a 290 MeV/n carbon-ion beam using the FLUKA Monte Carlo code.

caloremeters [5] and they measure the temperature rise in a medium as a result of radiation. In calorimetry, absorbed dose to water (D_{w}) is obtained by multiplying the temperature rise in the medium m as result of radiation (ΔT_m) with the specific heat capacity of the medium (c_m), the water-to-medium stopping-power ratio ($s_{\mathrm{w},m}$) and the product of necessary corrections (k_i):

$$D_{\mathrm{w}} = c_m \cdot \Delta T_m \cdot \frac{1}{1-h} \cdot s_{\mathrm{w},m} \cdot \Pi k_i \tag{1.1}$$

c_m in J.K^{-1}.kg^{-1}. h is the heat defect that corrects for the change in temperature due to any physical or chemical changes of the medium (e.g. chemical reactions). Correction factors include heat transport away from or towards the measurement point, field uniformity, and the presence of non-water materials in the calorimeter. These measurements should be done with an overall uncertainty below 1%, therefore the uncertainty of correction factors should not contribute more than 0.5% to the overall uncertainty [1].

Graphite calorimetry has been developed as a dosimetry technique due to its sensitivity (the temperature rise in graphite is six times that of water), and its thermal diffusivity which is much larger than water (the heat dissipates quicker in graphite than in water which allows faster measurements). Moreover, in graphite the heat defect is assumed to be negligible. Although graphite calorimetry has advantages, the quantity measured is absorbed dose to graphite and the quantity of interest is absorbed dose to water. Therefore, conversion factors need to be calculated in order to convert doses between the two media. This conversion requires not only knowledge of the water-to-graphite stopping-power ratio, but also the fluence correction factor k_{fl}. In light-ion beams, nucleus-nucleus collisions (non-elastic nuclear interactions) can take place and (i) change the nature of the projectile, decreasing the primary beam fluence and (ii) produce secondary particles. The first mentioned process is called projectile fragmentation and the second is a nuclear absorption or intranuclear cascade event. The difference between non-elastic nuclear interactions for different elements leads to different production rates of secondary particles. Therefore, the particle fluence present in water compared with the target material (graphite) at an equivalent depth will be different. This difference is corrected by computing the fluence correction factor k_{fl}. Figure 1.2 shows a comparison between depth-dose curves due to primary particles (dashed line) and all charged particles (solid line) for a 180 MeV proton beam (left) and a 290 MeV/n carbon-ion beam (right) in water. Nuclear interactions decrease the primary beam fluence and the differences between the curves (total absorbed dose and dose deposited due to primaries) reveals the relative importance of secondary particles. For example, in a 250 MeV proton beam about 30% of primary protons are attenuated due to nuclear interactions and about 60% of their kinetic energy emerges as secondary charged particles.

In radiation dosimetry, dose conversion between different media is also of interest in the measurement of dose to water in a plastic phantom using ionization chambers calibrated in terms of dose to water for relative and reference dosimetry [9, 10]. For relative dosimetry, water-equivalent plastic phantoms are frequently used in the measurements for simplicity. These materials are well developed for conventional radiotherapy, such as high-energy photon and electron beams, however, for light-ion therapy beams the use of water-equivalent plastics is not recommended [4]. The main reason that low-Z materials - such as plastic materials – are not water-equivalent in light-ion beams is the difference of the nuclear interaction cross sections between oxygen and other nuclei.

1.2 Aim of the work

This project focuses on three main objectives:

(i) **Determination of fluence correction factors for graphite calorimetry in light-ion beams.**

Fluence correction factors were determined using the FLUKA Monte Carlo code and measured experimentally in 180 MeV and 60 MeV proton beams and in a 290 MeV/n carbon-ion beam. These experiments were performed in the PTC Czech Proton Therapy Centre (Prague), in the Clatterbridge Cancer Centre (UK), and in the Gunma University Heavy Ion Medical Center (Japan).

(ii) **Development of new water-equivalent phantom materials for relative dosimetry in light-ion beams.**

Based on the results obtained in the first year of research, three test compositions for water-equivalent plastics were produced and experimentally characterized in 226 MeV and 60 MeV proton beams and in a 290 MeV/n carbon-ion beam. These experiments were performed in the Trento Proton Therapy Center (Italy), in the Clatterbridge Cancer Centre (UK), and in the Gunma University Heavy Ion Medical Center (Japan).

(iii) **Investigation of ionization chamber perturbation factors in clinical proton beams.**

The accuracy of particle transport in the FLUKA Monte Carlo code was assessed by performing a Fano cavity test and ionization chamber perturbation factors were calculated for the PTW 34070 Bragg peak chamber used in the experiments described above, with particular attention to the influence of nuclear interaction cross sections.

1.3 Novel contributions of this work

The growing interest in light-ion therapy in recent decades has led to a need for accurate dosimetry. The following is a description of my contributions to this field of research during my PhD:

- While fluence correction factors between water and graphite were first measured in low-energy proton and carbon-ion beams by Palmans *et al.* [11] and Rossomme *et al.* [12], respectively, the work presented here was the first time these factors were measured experimentally in high-energy proton and carbon-ion beams, where corrections are more significant. Moreover, a more practical experimental setup was used and a mathematical formalism that relates fluence corrections derived from Monte Carlo simulations to fluence correction measured experimentally was established for proton and carbon-ion beams.
- The water-equivalence of existing plastic materials (designed for high-energy

photon and electron beam dosimetry) in light-ion beams was studied previously by Palmans *et al.* [10], Al-Sulaiti *et al.* [13, 14] and Lühr *et al.* [15]. This work represents the first attempt to design and produce novel water-equivalent plastics specifically designed for light-ion beams. Furthermore, three trial plastics produced in-house were experimentally characterised in clinical proton and carbon-ion beams.

- Palmans and Verhaegen [7] and Verhaegen and Palmans [8] calculated ionization chamber perturbation factors due to secondary electrons in proton beams and suggested that perturbation effects caused by secondary particles from non-elastic nuclear interactions could be relevant. This thesis reports for the first time the accuracy of particle transport in the FLUKA Monte Carlo code for proton beams using a Fano cavity test, with particular attention to the influence of nuclear interactions. Particle transport parameters were optimised to compute an accurate ionization chamber response. Ionization chamber perturbation factors were also computed for the PTW 34070 Bragg peak chamber typically used in clinical proton beams.

This thesis has resulted in the following peer-reviewed publications:

- **A. Lourenço**, R. Thomas, H. Bouchard, A. Kacperek, V. Vondracek, G. Royle, and H. Palmans, "Experimental and Monte Carlo studies of fluence corrections for graphite calorimetry in low- and high-energy clinical proton beams", Medical Physics **43**, 4122-32 (2016)

- **A. Lourenço**, N. Wellock, R. Thomas, M. Homer, H. Bouchard, T. Kanai, N. MacDougall, G. Royle, and H. Palmans, "Theoretical and experimental characterization of novel water-equivalent plastics in clinical high-energy carbon-ion beams", Physics in Medicine and Biology **61**, 7623-38 (2016)

- **A. Lourenço**, D. Shipley, N. Wellock, R. Thomas, H. Bouchard, A. Kacperek, F. Fracchiolla, S. Lorentini, M. Schwarz, N. MacDougall, G. Royle, and H. Palmans, "Evaluation of the water-equivalence of plastic materials in low- and high-energy clinical proton beams" (currently under review in Physics in Medicine and Biology)

- **A. Lourenço**, R. Thomas, M. Homer, H. Bouchard, S. Rossomme, J. Renaud, T. Kanai, G. Royle, and H. Palmans, "Fluence correction factor for graphite calorimetry in a clinical high-energy carbon-ion beam" (currently under review in Physics in Medicine and Biology)

1.4 Structure of this thesis

Chapter 2 and chapter 3 describe the measurements and simulations performed to compute fluence corrections between water and graphite in proton and carbon-ion beams, respectively. Chapter 4 and chapter 5 present the work done on the water-equivalent phantom project for proton and carbon-ion beams, respectively. Chapter 6 describes the implementation of the Fano cavity test in FLUKA and the calculation of ionization chamber perturbation factors. Finally, chapter 7 summarises the overall research, future work arising from this study and concluding remarks.

Chapter 2

Fluence corrections for graphite calorimetry in low- and high-energy clinical proton beams

The work presented in this chapter has been published in the Medical Physics journal:

- **A. Lourenço**, R. Thomas, H. Bouchard, A. Kacperek, V. Vondracek, G. Royle, and H. Palmans, "Experimental and Monte Carlo studies of fluence corrections for graphite calorimetry in low- and high-energy clinical proton beams", Medical Physics **43**, 4122-32 (2016)

My contributions to this publication were as follows; experiments at the Clatterbridge Cancer Centre (UK) and the PTC Czech Proton Therapy Centre (Czech Republic) were performed by me with the assistance of NPL staff and local contacts; analysis and interpretation of the results and Monte Carlo simulations were performed by me under guidance of my supervisors and NPL staff; the paper was written by me and proof-read by the co-authors and Tania Avgoulea.

2.1 Summary

The aim of this study was to determine fluence corrections necessary to convert absorbed dose to graphite, measured by graphite calorimetry, to absorbed dose to water. Fluence corrections were obtained from experiments and Monte Carlo simulations in low- and high-energy proton beams. Fluence corrections were calculated

to account for the difference in fluence between water and graphite at equivalent depths. Measurements were performed with narrow proton beams. Plane-parallel-plate ionization chambers with a large collecting area compared to the beam diameter were used to intercept the whole beam. High- and low-energy proton beams were provided by a scanning and double scattering delivery system, respectively. A mathematical formalism was established to relate fluence corrections, derived from Monte Carlo simulations using the FLUKA code [16, 17], to partial fluence corrections measured experimentally. A good agreement was found between the partial fluence corrections derived by Monte Carlo simulations and those determined experimentally. For a high-energy beam of 180 MeV, the fluence corrections from Monte Carlo simulations were found to increase from 0.99 to 1.04 with depth. In the case of a low-energy beam of 60 MeV, the magnitude of fluence corrections was approximately 0.99 at all depths when calculated in the sensitive area of the chamber used in the experiments. Fuence correction calculations were also performed for a larger area and found to increase from 0.99 at the surface to 1.01 at greater depths. Fluence corrections obtained experimentally are partial fluence corrections because they account for differences in the primary and part of the secondary particle fluence. A correction factor, F, has been established to relate fluence corrections defined theoretically to partial fluence corrections derived experimentally. The findings presented here are also relevant to water and tissue-equivalent-plastic materials given their carbon content.

2.2 Rationale

A portable primary-standard level graphite calorimeter for light-ion beams was built at the National Physical Laboratory (NPL) [18], UK, based on earlier experience obtained with a small-body calorimeter [19]. This calorimeter will enable the provision of a direct absorbed dose-to-water calibration service. Users of this service would be the national eye Clatterbridge Cancer Centre (CCC), UK, and the two high-energy proton centres, currently under construction, in the UK. Although graphite calorimetry has advantages [20–23], the quantity measured is absorbed dose to graphite, D_{g}. Therefore, a conversion factor is necessary to determine absorbed dose to water, D_{w}. The conversion factor for the determination of absorbed dose to water is the main source of uncertainty in graphite calorimetry.

Several studies have been performed to determine fluence corrections for graphite calorimetry in proton beams. Lühr *et al.* [15] determined fluence correction factors and stopping-power ratios for graphite, bone and PMMA with the Monte Carlo code SHIELD-HIT10A for several light-ion beams including low- and high-energy proton beams. The authors showed that the correction was material, energy and projectile particle-type dependent. They reported that fluence corrections for high-energy beams were approximately 5%. Palmans *et al.* [24] estimated fluence correction factors in a low-energy monoenergetic proton beam from an analytical model and simulations using five different Monte Carlo codes. Contributions from different types of charged particles were assessed, and it was shown that secondary particles should be included in calculations of fluence corrections. A comparison between numerical simulations and experimental data from water-to-graphite fluence corrections in light-ion beams was performed by Rossomme *et al.* [12] for a low-energy carbon-ion beam and by Palmans *et al.* [11] for a low-energy monoenergetic proton beam. Ding *et al.* [9] derived fluence corrections for electron beams using the EGS4 user-code BEAM for various plastic materials and compared their results to those from Kase *et al.* [25] and Thwaites [26].

This study aims to present a novel method to determine fluence corrections experimentally, and to apply this methodology to low- and high-energy proton beams. Fluence corrections were also obtained through Monte Carlo simulations, using the FLUKA code, [16, 17], for comparison with the experiments. Experimental information was obtained from ionization chamber measurements of doses at depth in a water tank with and without graphite slabs upstream of the front face of the water tank. One distinct advantage of this method, compared to earlier work [11], is that only ionization chamber readings for water are required. A mathematical formalism that relates fluence corrections derived from Monte Carlo simulations to partial fluence corrections measured experimentally is presented.

2.3 Theory

2.3.1 Relation between experimental and Monte Carlo calculated fluence corrections

A mathematical formalism is presented to relate fluence corrections calculated experimentally to those obtained from numerical simulations. The equations established here were employed to compute fluence corrections between water (w) and graphite (g). The term $K_A^{(n)}$ refers to a variable K, in a medium A, calculated using setup number n. The three different experimental setups under consideration are shown in figure 2.1. The quantities of interest are:

(i) Setup 1: dose to water in an homogeneous phantom of water, $D_{\mathrm{w}}^{(1)}$

(ii) Setup 2: dose to graphite in an homogeneous phantom of graphite, $D_{\mathrm{g}}^{(2)}$

(iii) Setup 3: dose to water in a phantom of water after passing through a thickness of graphite (t_{g}), $D_{\mathrm{w}}^{(3)}$

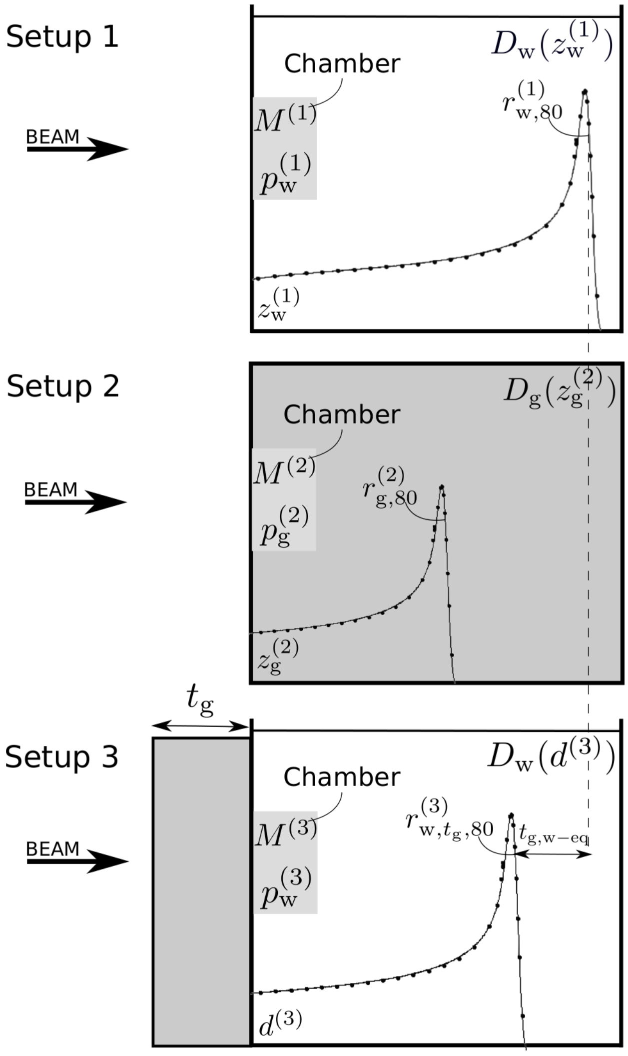

Figure 2.1: Schematic representation of the three experimental setups considered. The phantoms shown in white are filled with water. The grey color in setup 2 indicates a phantom composed of graphite while in setup 3 it depicts graphite slabs of variable thickness t_{g}.

As derived by Palmans *et al.* [10, 24], dose to water, $D_{\mathrm{w}}^{(1)}(z_{\mathrm{w-eq}})$, and dose to graphite, $D_{\mathrm{g}}^{(2)}(z_{\mathrm{g}}^{(2)})$, from a graphite calorimeter at equivalent depths, $z(_{\mathrm{eq}})$, are related by the water-to-graphite Bragg-Gray stopping-power ratio, $s_{\mathrm{w,g}}^{\mathrm{BG}}(\Phi_{\mathrm{g}}^{(2)})$, and the fluence correction factor, k_{fl},

$$D_{\text{w}}^{(1)}(z_{\text{w-eq}}) = D_{\text{g}}^{(2)}(z_{\text{g}}^{(2)}) \cdot s_{\text{w,g}}^{\text{BG}}(\Phi_{\text{g}}^{(2)}) \cdot k_{\text{fl}}, \tag{2.1}$$

A given depth in graphite is related to an equivalent depth in water by,

$$z_{\text{w-eq}} = z_{\text{g}}^{(2)} \cdot \frac{r_{\text{w},80}^{(1)}}{r_{\text{g},80}^{(2)}}, \tag{2.2}$$

where $r_{\text{w},80}^{(1)}$ and $r_{\text{g},80}^{(2)}$ are depths in water and graphite, respectively, at which the dose drops to 80% of its maximum at the distal edge of the Bragg peak. There is evidence [1] that the 80% distal value of the Bragg peak corresponds to the depth reached by 50% of primary protons, i.e. protons which did not undergo nuclear interactions. This depth is approximately independent of the energy spread of incident beams with the same mean energy [1].

Using Monte Carlo methods, Palmans *et al.* [24] calculated the fluence correction factor, $k_{\text{fl,dose}}^{\text{MC}}$ as a ratio of doses expressed as,

$$k_{\text{fl,dose}}^{\text{MC}}(z_{\text{w-eq}}) = \frac{D_{\text{w}}^{(1)}(z_{\text{w-eq}})}{D_{\text{g}}^{(2)}(z_{\text{g}}^{(2)}) \cdot s_{\text{w,g}}^{\text{BG}}(\Phi_{\text{g}}^{(2)})}, \tag{2.3}$$

and the fluence correction factor, $k_{\text{fl,fluence}}^{\text{MC}}$, from fluence distributions differential in energy in water and graphite,

$$k_{\text{fl,fluence}}^{\text{MC}}(z_{\text{w-eq}}) = \frac{\sum_i \left[\int_{E_{\min,i}}^{E_{\max,i}} \Phi_{E,\text{w},i}^{(1)}(E) \cdot \left(\frac{S_i(E)}{\rho}\right)_{\text{w}} \cdot dE\right]}{\sum_i \left[\int_{E_{\min,i}}^{E_{\max,i}} \Phi_{E,\text{g},i}^{(2)}(E) \cdot \left(\frac{S_i(E)}{\rho}\right)_{\text{w}} \cdot dE\right]}, \tag{2.4}$$

where i represents the charged particle types, $\Phi_E(E)$ the fluence differential in energy, and S/ρ the mass stopping power. The influence of secondary electron transport was not considered. A detailed description of equations 2.3 and 2.4 can be found in Palmans *et al.* [24]. In this work, cut-off energies for protons and heavier particles were set to 100 keV, with a typical continuous slowing down approximation (CSDA) range of 1.607×10^{-4} g.cm^{-2} for protons in water [27, 28].

The IAEA TRS-398 [4] Code of Practice defines the fluence scaling factor, h_{pl}, to account for the difference in charged particle fluence between homogeneous phantoms of water and plastics. Palmans *et al.* [11] applied this definition to proton beams, and Rossomme *et al.* [12] to carbon-ion beams using setups 1 and 2. In this work, in order to derive fluence corrections by experiment, $k_{\text{fl}}^{\text{exp}}$, depth-dose curves were measured using setups 1 and 3. The latter is preferable to setup 2 which requires sampling sufficient data points across the experimental range in graphite; a time consuming approach due to the steepness of the Bragg peak and the need to manually change the graphite thickness. Furthermore, the ratio of ion chamber perturbation correction factors in water and graphite are not well known for proton therapy beams. For setups 1 and 3, it can be assumed that by always measuring in water there is little variation in the ratio of ionization chamber perturbations.

A comparison between setups 1 and 3 should be made at a water-equivalent depth. For each slab, or set of slabs, an accurate value of the water-equivalent thickness (WET), $t_{\mathrm{g,w-eq}}$, was determined. Depth-dose measurements were made in water, with and without, graphite slabs upstream of the front wall of the water phantom. For each slab or each combination of slabs used, the WET, $t_{\mathrm{g,w-eq}}$, was determined by the shift of the Bragg peak as shown in figure 2.1,

$$t_{\mathrm{g,w-eq}} = r^{(1)}_{\mathrm{w},80} - r^{(3)}_{\mathrm{w},t_{\mathrm{g}},80} \tag{2.5}$$

In setup 1, and in keeping with the Bragg-Gray cavity theory, the dose $D^{(1)}_{\mathrm{w}}$ at a depth $z^{(1)}_{\mathrm{w}}$, is related to the ionization chamber reading at the same depth, $M^{(1)}$ by,

$$D^{(1)}_{\mathrm{w}}(z^{(1)}_{\mathrm{w}}) = M^{(1)}(z^{(1)}_{\mathrm{w}}) \cdot \frac{W^{(1)}_{\mathrm{air}}/e}{m_{\mathrm{air}}} \cdot s^{\mathrm{SA}}_{\mathrm{w,air}}(\Phi^{(1)}_{\mathrm{w}}) \cdot p^{(1)}_{\mathrm{w}}(z^{(1)}_{\mathrm{w}}) \tag{2.6}$$

where m_{air} is the mass of air in the cavity, W_{air}/e is the average energy required to form an ion pair in air, $s^{\mathrm{SA}}_{\mathrm{w,air}}$ is the water-to-air Spencer-Attix stopping-power ratio and $p^{(1)}_{\mathrm{w}}$ is the perturbation correction factor for the ionization chamber in water.

Similarly, in setup 3, the dose $D^{(3)}_{\mathrm{w}}$ at a depth in water $d^{(3)}$, for a graphite thickness t_{g} can be expressed as,

$$D^{(3)}_{\mathrm{w}}(d^{(3)}, t_{\mathrm{g}}) = M^{(3)}(d^{(3)}, t_{\mathrm{g}}) \cdot \frac{W^{(3)}_{\mathrm{air}}/e}{m_{\mathrm{air}}} \cdot s^{\mathrm{SA}}_{\mathrm{w,air}}(\Phi^{(3)}_{\mathrm{w}}) \cdot p^{(3)}_{\mathrm{w}}(d^{(3)}, t_{\mathrm{g}}), \tag{2.7}$$

where, $s^{\mathrm{SA}}_{\mathrm{w,air}}(\Phi^{(3)}_{\mathrm{w}})$ refers to a quantity $\Phi^{(3)}_{\mathrm{w}}$ that represents the fluence in water after passing through a layer of graphite, and $p^{(3)}_{\mathrm{w}}$ is the perturbation correction factor in water for the fluence $\Phi^{(3)}_{\mathrm{w}}$.

Depth in water is defined as, $z^{(1)}_{\mathrm{w}} = d^{(3)} + t_{\mathrm{g,w-eq}}$, where $d^{(3)}$ corresponds to an arbitrary depth in setup 3 and $d^{(3)} = 0$ at the interface between graphite and water. The ratio of ionization chamber readings $M^{(1)}$ and $M^{(3)}$ can be obtained from combining equations 2.6 and 2.7,

$$\frac{M^{(1)}(z^{(1)}_{\mathrm{w}})}{M^{(3)}(d^{(3)}, t_{\mathrm{g}})} = \frac{D^{(1)}_{\mathrm{w}}(z^{(1)}_{\mathrm{w}})}{D^{(3)}_{\mathrm{w}}(d^{(3)}, t_{\mathrm{g}})} \cdot \frac{W^{(3)}_{\mathrm{air}}/e}{W^{(1)}_{\mathrm{air}}/e} \cdot \frac{s^{\mathrm{SA}}_{\mathrm{w,air}}(\Phi^{(3)}_{\mathrm{w}})}{s^{\mathrm{SA}}_{\mathrm{w,air}}(\Phi^{(1)}_{\mathrm{w}})} \cdot \frac{p^{(3)}_{\mathrm{w}}(d^{(3)}, t_{\mathrm{g}})}{p^{(1)}_{\mathrm{w}}(z^{(1)}_{\mathrm{w}})} \tag{2.8}$$

It was assumed that:

(i) The difference in chamber perturbation between setups 1 and 3 is negligible, $p_{\mathrm{w}}^{(3)}(d^{(3)}, t_{\mathrm{g}}) \approx p_{\mathrm{w}}^{(1)}(z_{\mathrm{w}}^{(1)})$. Ionization chamber perturbation factors are close to unity and vary up to 1% from 0 to 250 MeV [8]. Therefore, the small differences in spectra between setups 1 and 3 have negligible influence.

(ii) The stopping-power ratio for $\Phi_{\mathrm{w}}^{(3)}$ and $\Phi_{\mathrm{w}}^{(1)}$ is equal, $s_{\mathrm{w,air}}^{\mathrm{SA}}(\Phi_{\mathrm{w}}^{(3)}) \approx s_{\mathrm{w,air}}^{\mathrm{SA}}(\Phi_{\mathrm{w}}^{(1)})$. The stopping power ratios vary little with energy so for the two spectra [27], which are very similar, the stopping power ratios are likely to be almost equal. This has been verified with Monte Carlo simulations and a maximum correction between the water-to-air stopping-power ratios for $\Phi_{\mathrm{w}}^{(3)}$ and $\Phi_{\mathrm{w}}^{(1)}$ was found to be 0.01% [24].

(iii) The variation of W_{air}/e between the two setups is negligible since the spectra are marginally different. At present, there is no experimental evidence that W_{air}/e varies with energy for proton therapy beams [29], however, model data from Grosswendt and Baek [30] suggest its variation with energy.

Using equation B.15 from IAEA TRS-398 [4] Code of Practice and model data from Grosswendt and Baek [30], the variation of W_{air}/e between setups 1 and 3 was calculated and maximum variations were of the order of 0.01% when considering the proton spectra (primary and secondary protons). Although, the contribution of other particles (alphas, deuterons, etc) was not considered due to the lack of data, the total contribution of these particles is small in comparison with protons and, therefore, they will have a smaller effect in the variation of W_{air}/e between the two setups.

The propagation of uncertainties of the assumptions described above was 0.1%.

Dose in setup 3, $D_{\mathrm{w}}^{(3)}(d^{(3)}, t_{\mathrm{g}}) = \sum_i \left[\int_0^{E_{\mathrm{max},i}} \Phi_{E,\mathrm{w},i}^{(3)}(E) \cdot \left(\frac{S_i(E)}{\rho}\right)_{\mathrm{w}} \cdot dE\right]$, is related with dose in setup 2, $D_{\mathrm{g}}^{(2)}(z_{\mathrm{g}}^{(2)}) = \sum_i \left[\int_0^{E_{\mathrm{max},i}} \Phi_{E,\mathrm{g},i}^{(2)}(E) \cdot \left(\frac{S_i(E)}{\rho}\right)_{\mathrm{g}} \cdot dE\right]$, by the water-to-graphite stopping-power ratio $s_{\mathrm{w,g}}^{\mathrm{BG}}(\Phi_{\mathrm{g}}^{(2)})$ and a correction factor $F(d^{(3)})$ that accounts for the difference in fluence between the setups, $D_{\mathrm{w}}^{(3)}(d^{(3)}, t_{\mathrm{g}}) = D_{\mathrm{g}}^{(2)}(z_{\mathrm{g}}^{(2)}) \cdot s_{\mathrm{w,g}}^{\mathrm{BG}}(\Phi_{\mathrm{g}}^{(2)}) \cdot F(d^{(3)})$, where

$$s_{\mathrm{w,g}}^{\mathrm{BG}}(\Phi_{\mathrm{g}}^{(2)}) = \frac{\sum_i \left[\int_{E_{\mathrm{min},i}}^{E_{\mathrm{max},i}} \Phi_{E,\mathrm{g},i}^{(2)}(E) \cdot \left(\frac{S_i(E)}{\rho}\right)_{\mathrm{w}} \cdot dE\right]}{\sum_i \left[\int_{E_{\mathrm{min},i}}^{E_{\mathrm{max},i}} \Phi_{E,\mathrm{g},i}^{(2)}(E) \cdot \left(\frac{S_i(E)}{\rho}\right)_{\mathrm{g}} \cdot dE\right]} \tag{2.9}$$

and

$$F(d^{(3)}) = \frac{\sum_i \left[\int_{E_{\mathrm{min},i}}^{E_{\mathrm{max},i}} \Phi_{E,\mathrm{w},i}^{(3)}(E) \cdot \left(\frac{S_i(E)}{\rho}\right)_{\mathrm{w}} \cdot dE\right]}{\sum_i \left[\int_{E_{\mathrm{min},i}}^{E_{\mathrm{max},i}} \Phi_{E,\mathrm{g},i}^{(2)}(E) \cdot \left(\frac{S_i(E)}{\rho}\right)_{\mathrm{w}} \cdot dE\right]} \tag{2.10}$$

Thus, considering the assumptions described above, equation 2.8 can be expressed as,

$$\frac{M^{(1)}(z_{\mathrm{w}}^{(1)})}{M^{(3)}(d^{(3)},t_{\mathrm{g}})} \approx \frac{D_{\mathrm{w}}^{(1)}(z_{\mathrm{w}})}{D_{\mathrm{g},i}^{(2)}(z_{\mathrm{g}}^{(2)}) \cdot s_{\mathrm{w,g},i}^{\mathrm{BG}}(\Phi_{\mathrm{g}}^{(2)}) \cdot F(d^{(3)})} \approx \frac{k_{\mathrm{fl,dose}}}{F(d^{(3)})} \tag{2.11}$$

Consequently, the measurement ratio is related to the total fluence correction factor, from equation 2.3, by a correction factor $F(d^{(3)})$. Therefore, in keeping with equation 2.3, the total fluence correction factor can be calculated experimentally by,

$$k_{\mathrm{fl}}^{\mathrm{exp}}(t_{\mathrm{g,w-eq}}) \approx \frac{M^{(1)}(z_{\mathrm{w}}^{(1)})}{M^{(3)}(d^{(3)},t_{\mathrm{g}})} \cdot F(d^{(3)}) \tag{2.12}$$

Accordingly, the ratio of ion chamber readings from setups 1 and 3 represents a partial fluence correction factor because it accounts for differences in the primary and part of the secondary particle fluence. For the conversion of dose to graphite to dose to water three main particles contribute to the fluence correction factor: primary protons, secondary protons and alpha particles [24]. In Fluka [16, 17], for incident proton energies of 60 MeV and 200 MeV, in a proton-^{16}O collision, the average emission energy of alpha particles are 5.0 MeV and 6.8 MeV and their corresponding CSDA ranges in water are 0.04 mm and 0.06 mm, respectively [27]. The range values are similar for proton-^{12}C collisions. These results are consistent with ICRU Report 63 data, where for the same incident proton energies and type of collision, the average emission energies of alpha particles are 5.8 MeV and 9.8 MeV, respectively. In keeping with ICRU Report 63, uncertainties for total non-elastic cross sections and angle-integrated production cross sections for secondary particles are 5%-10% and 20%-30%, respectively, which could explain the differences between the models. The range of alpha particles indicate that particles generated in the slab of graphite, t_{g}, do not have enough energy to penetrate the chamber wall. The same applies to a fraction of secondary protons with low energy while high-energy secondary protons do reach the chambers cavity and are thus accounted in the partial fluence correction factor. Therefore, the measurement ratio represents a partial fluence correction factor:

$$k_{\mathrm{fl,partial}}^{\mathrm{exp}}(t_{\mathrm{g,w-eq}}) \approx \frac{M^{(1)}(z_{\mathrm{w}}^{(1)})}{M^{(3)}(d^{(3)},t_{\mathrm{g}})}, \tag{2.13}$$

and from Monte Carlo methods,

$$k_{\mathrm{fl,partial}}^{\mathrm{MC}}(t_{\mathrm{g,w-eq}}) \approx \frac{D_{\mathrm{w}}^{(1)}(z_{\mathrm{w}}^{(1)})}{D_{\mathrm{w}}^{(3)}(d^{(3)},t_{\mathrm{g}})} \tag{2.14}$$

Assuming that the change in fluence from the surface to the measurement point is not different from setups 1 and 3, then $k_{\mathrm{fl,partial}}$ for a specific $t_{\mathrm{g,w-eq}}$ is the same value at every depth $d^{(3)}$ and a mean value can be derived for N depths experimentally, expressed as,

$$k^{\mathrm{exp}}_{\mathrm{fl,partial}}(t_{\mathrm{g,w-eq}}) \approx \frac{1}{N}\sum_{j=1}^{N}\frac{M^{(1)}(z^{(1)}_{\mathrm{w}})}{M^{(3)}(d^{(3)}_{j}, t_{\mathrm{g}})} \tag{2.15}$$

Also, using Monte Carlo methods,

$$k^{\mathrm{MC}}_{\mathrm{fl,partial}}(t_{\mathrm{g,w-eq}}) \approx \frac{1}{N}\sum_{j=1}^{N}\frac{D^{(1)}_{\mathrm{w}}(z^{(1)}_{\mathrm{w}})}{D^{(3)}_{\mathrm{w}}(d^{(3)}_{j}, t_{\mathrm{g}})} \tag{2.16}$$

This has been verified with Monte Carlo simulations and it avoids statistical errors. For each slab of graphite with thickness t_{g} tested experimentally, its water-equivalent thickness was calculated from equation 2.5. The ratio between water and graphite-water ionization readings was calculated at equivalent depths and a mean value was computed to represent $k^{\mathrm{exp}}_{\mathrm{fl,partial}}$ for a given slab t_{g} of graphite.

2.4 Methods

2.4.1 Measurements

Measurements were performed at two separate clinical sites: the 60 MeV proton cyclotron at the Clatterbridge Cancer Centre (CCC), UK and the 226 MeV proton cyclotron at the PTC Czech Proton Therapy Centre (PTC Czech), using a beam of 180 MeV. Narrow beams were used without any range modulation. In the CCC beam a collimator of 4 mm diameter was used, whereas in the case of the PTC Czech beam a single spot was used. A PTW type 7862 transmission chamber was placed in front of the beam exit for monitoring purposes. A water phantom with an entrance window of 3.7 mm WET of PMMA was placed in front of the beam exit with the phantom surface aligned with the isocentre. Low-energy beam measurements were performed using a PTW 34001 Roos chamber with a sensitive diameter of 15 mm. High-energy beam measurements were carried out with a PTW 34070 Bragg peak chamber with sensitive diameter of 81.6 mm. The sensitive diameter of both chambers was large in comparison to the beams diameter to ensure that all particles were intercepted. Since measurements were acquired for a laterally integrated fluence there was no correction required for the inverse square law. The chambers were kept at a constant source-to-detector distance, SDD, in order to avoid corrections for the divergence of the beam. The water phantom was moved towards the gantry by a moving platform in order to vary the amount of water in front of the chamber.

Measurements were repeated with graphite plates of variable thicknesses attached to the front window of the water tank.

2.4.2 Monte Carlo Simulations

All the Monte Carlo simulations described in this chapter were performed with the FLUKA-2011.2c.2 code [16, 17]. FLUKA uses the best data available and it is continuously developed and benchmarked against recent LHC data. Furthermore, FLUKA nuclear models have been validated against experimental data for proton and carbon-ion beams [31, 32]. The fluence correction factor was computed using three approaches based on: dose thus establishing $k_{\text{fl,dose}}^{\text{MC}}$ from equation 2.3, fluence thus obtaining $k_{\text{fl,fluence}}^{\text{MC}}$ from equation 2.4 and partial fluence where $k_{\text{fl,partial}}^{\text{MC}}$ is derived from equation 2.16. For the dose and fluence approaches, measurements were performed in a pure water and graphite phantoms whereas in the case of the partial fluence method measurements were performed in a water phantom.

The entire geometry of the CCC scattering beam line was simulated as described in [33–35]. The PTC Czech beam line configuration was not considered in the numerical simulations because it consists of a scanning system and therefore the influence of the beam line geometry on the calculation of the fluence correction factor is negligible [12].

Depth-dose distributions and fluence differential in energy were simulated for the 60 MeV beam and for the 180 MeV beam in cylindrical phantoms of water ($\rho = 1.0\,\text{g.cm}^{-3}$) and graphite ($\rho = 1.8\,\text{g.cm}^{-3}$). The default card HADROTHErapy was activated with a delta-ray production set to infinite threshold such that delta-ray production was not considered in the simulations. The most energetic secondary electrons have a short range of <1 mm and therefore all energy transferred to electrons can be regarded as absorbed locally. Full transport of light and heavy ions was included. For the CCC beam simulations, transport of neutrons was not considered because these particles are mainly generated in the materials of the beam line and neutron dose has been reported to be less than 0.001% of the treatment dose [35]. CCC beam simulations were performed on cylindrical phantoms of 10 cm radius and 3.5 cm thickness. The absorbed doses were scored in 0.01 cm bins. For the calculation of $k_{\text{fl,fluence}}^{\text{MC}}$ and $k_{\text{fl,dose}}^{\text{MC}}$ the phantom was positioned with its surface at the isocentric plane (7 cm from the collimator exit). For each material, 5×10^{8} primary particles were simulated. PTC Czech beam simulations were performed in a cylindrical phantom of 10 cm radius and 26 cm thickness. Absorbed doses for the latter were also scored in 0.01 cm bins and for each material 5×10^6 primary particles were simulated. Fluence differential in energy was scored in 0.1 cm thick slabs throughout the phantoms. Absorbed doses and fluences differential in energy were also scored in smaller volumes, equal to the sensitive area as the chambers used in the experiments.

In order to compute $k_{\text{fl,partial}}^{\text{MC}}$, absorbed doses were scored in the water phantom of setup 1 and compared to those from setup 3. Although during experiments the SDD was kept constant, it is significantly more efficient to perform Monte Carlo simulations with a constant source-to-surface distance (SSD). The latter only requires a single simulation to calculate dose with depth, whereas the SDD setup requires a simulation for each depth. Consequently, SDD values were derived from SSD values as follows. Figure 2.2 shows a schematic representation of the setups to obtain depth-dose curves with SSD constant ($D^{\text{SSD}}(z_{\text{w}}^{(1)}, x_k)$) and SDD constant ($D^{\text{SDD}}(z_{\text{w}}^{(1)}, x_k)$). In both situations, dose is a function of $z_{\text{w}}^{(1)}$, which is the depth in water, and x_k, which is a discrete variable that corresponds to the distance from the phantom surface to the reference plane (for which $x_k = 0$). For the setup with SSD constant, $x_k = 0$, and for the setup with SDD constant, $z_{\text{w}}^{(1)} = x_k$. $D^{\text{SDD}}(z_{\text{w}}^{(1)}, x_k)$ was calculated at a discrete set of x_k values and a correction $C(z_{\text{w}}^{(1)})$ was calculated

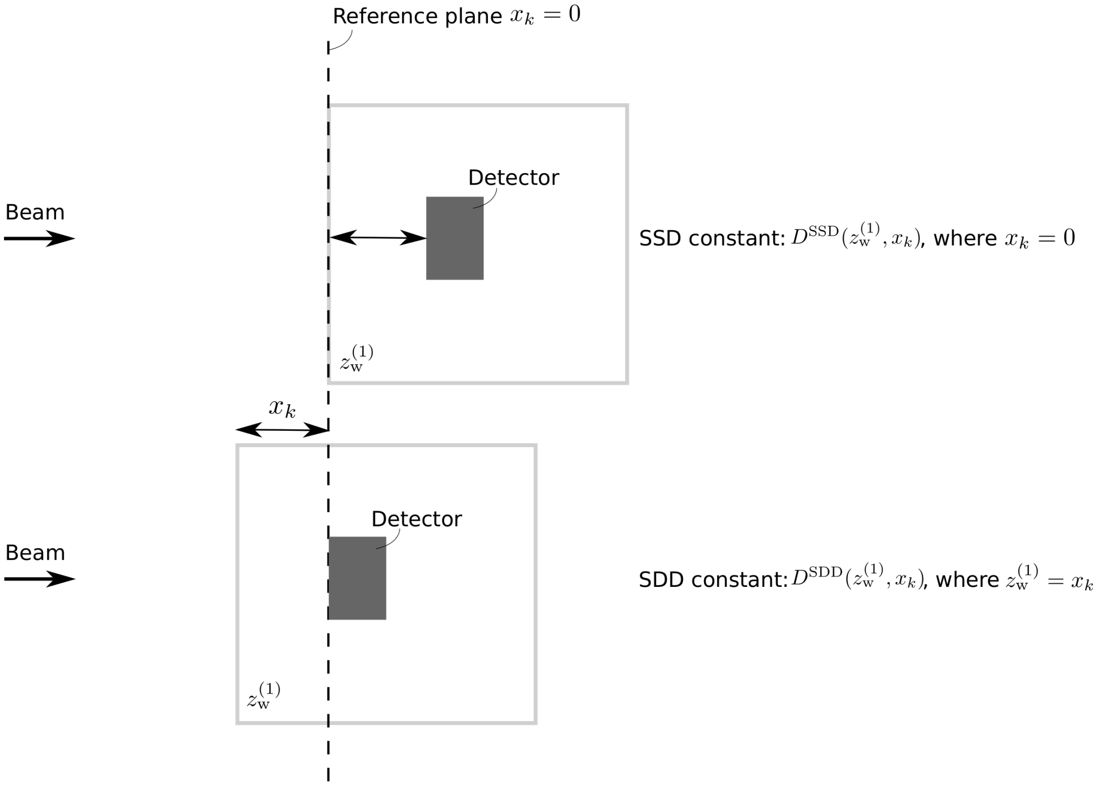

Figure 2.2: Schematic representation of the experimental setups to obtain depth-dose curves with SSD constant (top) and SDD constant (bottom).

to derive $D^{\mathrm{SDD}}(z_{\mathrm{w}}^{(1)}, x(k))$, where $x(k)$ represents a continuous variable, therefore,

$$D^{\mathrm{SDD}}(z_{\mathrm{w}}^{(1)}, x(k)) \approx D^{\mathrm{SSD}}(z_{\mathrm{w}}^{(1)}, 0) \cdot C(z_{\mathrm{w}}^{(1)}) \tag{2.17}$$

Where $C(z_{\mathrm{w}}^{(1)}) = D^{\mathrm{SDD}}(z_{\mathrm{w}}^{(1)}, x_k)/D^{\mathrm{SSD}}(z_{\mathrm{w}}^{(1)}, 0)$. A cubic spline was fitted to $C(z_{\mathrm{w}}^{(1)})$ to obtain a continuous correction for all values $z_{\mathrm{w}}^{(1)}$. Figure 2.3 shows the calculated ratio of $D^{\mathrm{SDD}}(z_{\mathrm{w}}^{(1)}, x_k)$ and $D^{\mathrm{SSD}}(z_{\mathrm{w}}^{(1)}, 0)$. For the PTC Czech beam the correction is very small, therefore, real depth-dose curves were calculated where the SSD was constant. For the CCC beam, the primary protons scattered at low angles, by the collimator edges, increase with decreasing collimator diameter [35]. Therefore, the beam size used was such that the contribution from the protons scattered at low angles was not negligible [35] and a correction was applied for the derivation of SDD from SSD.

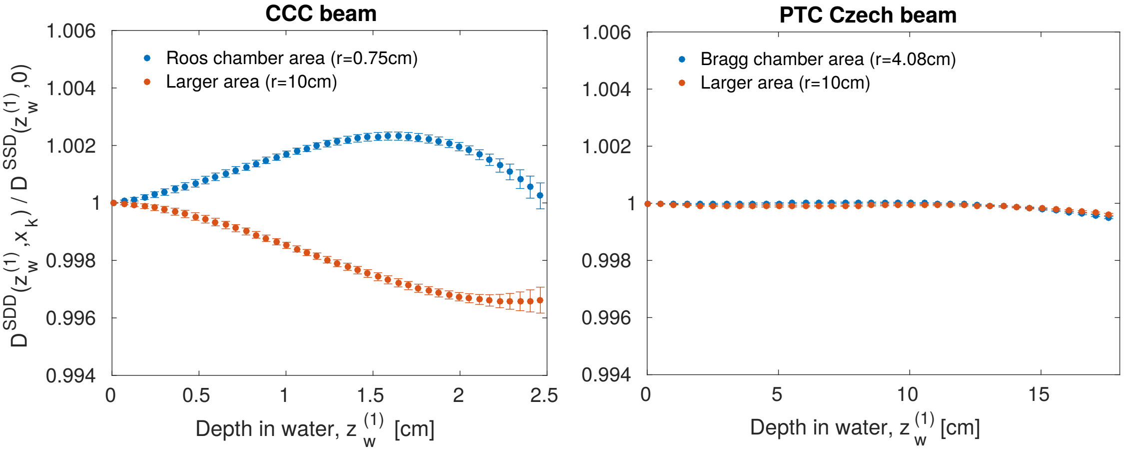

(a) (b)

Figure 2.3: Correction for the derivation of SDD from SSD for (a) the CCC beam and (b) the PTC Czech beam. The correction for the PTC Czech beam is very small.

2.4.3 Assessing uncertainties

Uncertainties were calculated as the standard deviation of the mean of repeated observations [36]. The sources of experimental uncertainties to determine $k_{\mathrm{fl,partial}}^{\mathrm{exp}}$ are presented in table 2.1 for the measurements performed with the PTC Czech and the CCC beams. All uncertainties are expressed as relative standard uncertainties. The overall uncertainty is quoted to 1σ and was calculated by combining type A and B uncertainties in quadrature. Type A and Type B uncertainties were determined following guidelines of the *Guide to the Expression of Uncertainty in Measurements* (GUM) [36].

Table 2.1: Experimental relative standard uncertainties for the PTC Czech and CCC beams.

	PTC Czech		**CCC**	
Source of uncertainty	Type A (%)	Type B (%)	Type A (%)	Type B (%)
Repeatability	0.03	-	0.65	-
Temperature	-	0.05	-	0.05
Pressure	-	0.05	-	0.05
$s_{\overline{k_{\mathrm{fl,partial}}^{\mathrm{exp}}}}$	-	0.42	-	0.30
Variations in chamber position	-	0.79	N/A	N/A
Total	**0.030**	**0.898**	**0.650**	**0.308**
Overall (%)	**0.9**		**0.7**	

The repeatability was considered as type A and the uncertainty in temperature, pressure and standard deviation of the mean value of $k_{\mathrm{fl,partial}}^{\mathrm{exp}}$ with depth as type B. The same type of electrometer was used and thus for a given ratio of two readings, for example, standard chamber/monitor chamber, any type B uncertainty related to the electrometer was correlated and cancelled out. The same applies to ion recombination corrections. Uncorrelated uncertainties, such as fluctuations and drifts, were considered negligible. For the PTC Czech experiments variations in chamber position were also considered. During the experiments, the water pressure exerted on the Bragg chamber when the water phantom was moving resulted in an uncertainty in chamber position. This was because the chamber support was not suitable to accommodate a chamber of that size. Variations in chamber position were estimated based on position checks performed in the experiments.

It was more challenging to estimate type B uncertainties in the Monte Carlo simulations than type A. Type B uncertainties include propagation of uncertainties from stopping-power data, material data and interaction cross sections. In the high-energy region, uncertainties in the stopping powers for elemental materials are smaller than 1%. In the low-energy region, uncertainties become as large as 5%-25% [27]. Material-data uncertainties include uncertainties in stopping powers and mean excitation energy (I-values). Nuclear data files can vary depending on the models implemented in a given Monte Carlo code and, at present, estimates of these type of uncertainties are not provided. However, in keeping with ICRU Report 63 [37] uncertainties for total non-elastic cross sections and angle-integrated production cross sections for secondary particles are 5%-10% and 20%-30%, respectively. Type A uncertainties for the fluence correction factor computed by numerical simulations were below 0.2%. Uncertainties become larger when approaching the depth of the

Bragg peak because positioning in depth becomes very critical due to the steep gradient. Therefore, those points were not considered in the calculation of the fluence correction factor.

2.5 Results and discussion

2.5.1 Depth-dose curves

In the experiments, laterally integrated measurements were performed in narrow beams. In the CCC beam a collimator of 0.4 cm diameter was used, whereas in the case of the PTC Czech beam a single spot was used with FWHM = 1.3 cm. The measurements at CCC were performed with a chamber with a sensitive diameter of 1.5 cm, while measurements at PTC Czech were performed with a chamber with a sensitive diameter of 8.16 cm. The sensitive diameter of both chambers was large in comparison to the beams diameter to ensure that all primary particles were intercepted. However, for the CCC beam the primary protons scattered at low angles, by the collimator edges, increase with decreasing collimator diameter. Therefore, the beam size used was such that the contribution from the primary protons scattered at low angles was not negligible. In the case of the PTC Czech beam, secondary protons, generated from non-elastic nuclear interactions escape the sensitive area of the chamber. Thus, the contribution of particles scattered outside the sensitive area of the chambers was studied using Monte Carlo simulations.

The ratio between the energy deposited inside the chamber sensitive area and the energy deposited in a larger area was calculated and the results are shown in figure 2.4 for water and graphite.

For the PTC Czech beam, the ratio is very close to unity for primary protons because the deflection of the primary beam is small. Secondary protons, generated from non-elastic nuclear interactions, emerge with larger angles with respect to the incident proton direction and thus escape the sensitive area of the chamber. Accordingly, their contribution is not taken into account. Furthermore, water contains free hydrogen with which the projectile protons can undergo elastic collisions and produce secondary protons with larger scatter angles. The maximum total energy loss occurs in the build-up region and amounts to 2.5% and 0.8% for water and graphite, respectively. In addition, for graphite, the lateral projected range is shorter because its density is higher than that of water.

For the CCC beam, primary protons were scattered at low angles from the edges of the collimator and thus approximately 30% of the primary protons were not detected inside the area of the chamber.

Experimental depth-dose distributions acquired are compared with Monte Carlo simulations in figure 2.5. The WET of the front window of the water phantom and the water-equivalent-window thickness of the chambers were considered when defining the depths at which experimental measurements were carried out. Curves were normalized to unity at the first measurement depth because chamber readings were expressed in units of Coulomb (C) and absorbed doses from Monte Carlo simulations were in units of Gray (Gy). Numerical simulations were tuned for 62.5 MeV at the source and 180 MeV, assuming energy spreads of $\sigma = 0.28\,\mathrm{MeV}$ and 0.9 MeV for the CCC and PTC Czech beams, respectively.

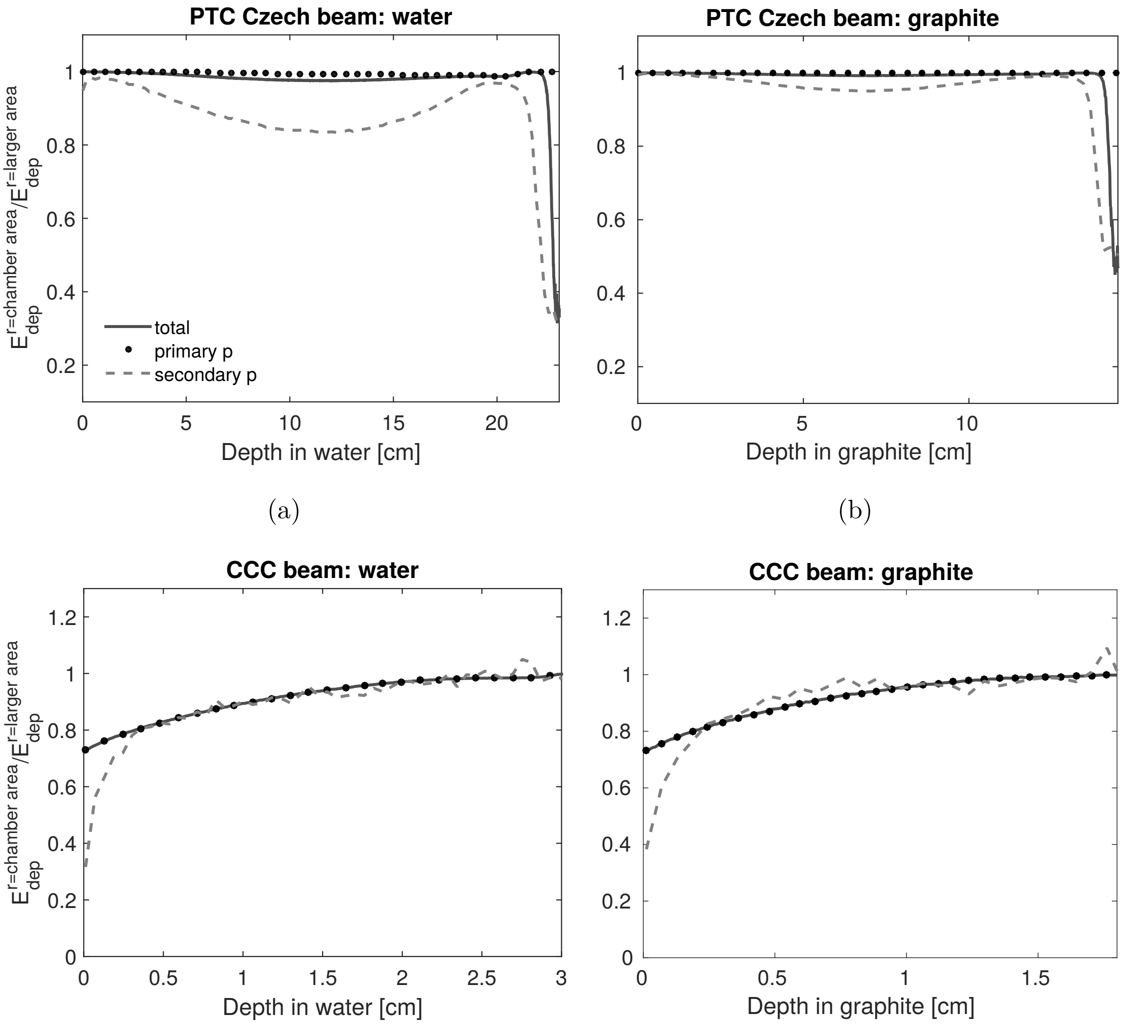

(a) (b)

(c) (d)

Figure 2.4: Ratio between energy deposited inside the area of the ionization chambers used in the experiments and energy deposited in a larger area. The graphs represent ratio of the total energy and energy due to the contribution of primary and secondary protons in water (left) and graphite (right).

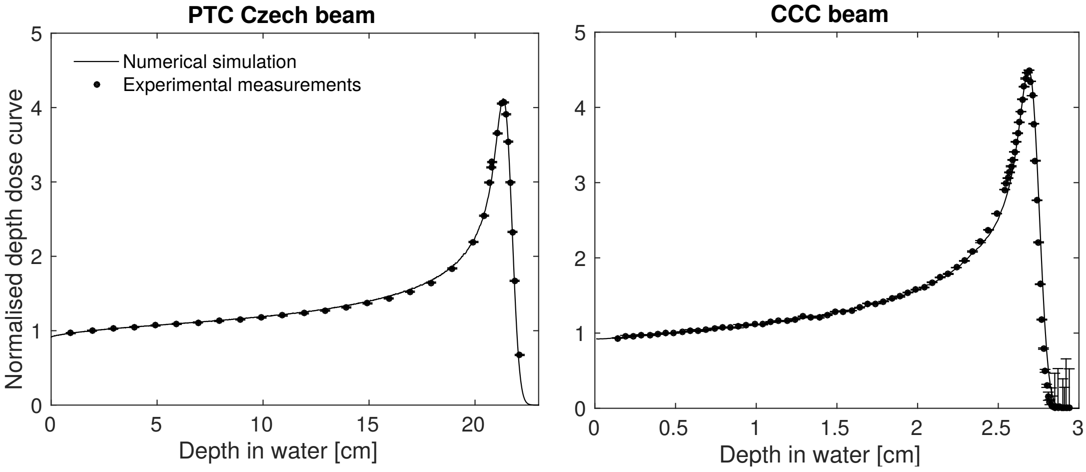

Figure 2.5: Experimental and Monte Carlo depth-dose curves in water for (a) the 180 MeV PTC Czech beam and (b) for the 62.5 MeV CCC beam. Maximum differences between experimental points and Monte Carlo were of the order of 2%.

2.5.2 Dose from primary and secondary particles

The three main particle types that contribute to the fluence correction factor between water and graphite are: primary protons, secondary protons and alpha particles [24]. Figure 2.6 shows the contributions of these particles. The major contribution to the total dose stems from primary and secondary protons. The contribution of secondary particles is higher in graphite than in water due to a larger total non-elastic nuclear interaction cross section per atomic mass [4]. Particles scored for the calculation of the fluence correction factor were: primary and secondary protons, alphas, ^{3}He ions, deuterons and tritons.

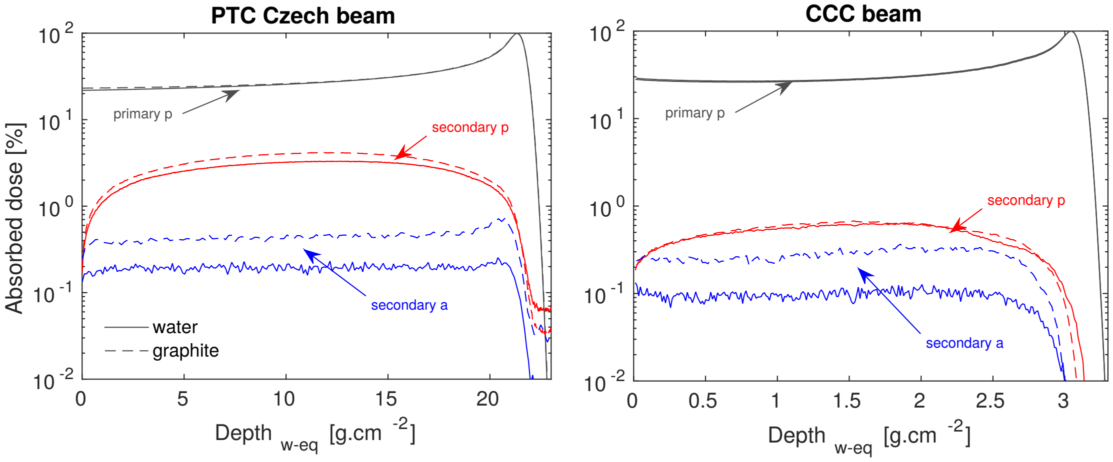

Figure 2.6: Monte Carlo simulations of the absorbed dose curves as a function of depth for (a) the PTC Czech beam and (b) for the CCC beam in water (straight line) and graphite (dashed line). The graphs show the contribution of each particle in a percentage of absorbed dose (p = protons and a = alphas).

2.5.3 Fluence corrections

2.5.3.1 PTC Czech beam

The fluence correction results for the PTC Czech beam as derived from the fluence and dose based methods are presented in figure 2.7. The quantities of interest were calculated in an area equal to the sensitive area of the chamber used experimentally. A calculation of fluence corrections in a larger area was also performed to account for particles that scatter outside the sensitive area of the chamber. Primary protons that undergo elastic nuclear interactions were considered as primary particles and in a p-H elastic collision, the largest energy proton was considered as primary. At the surface (depth = 0 cm), primary proton fluence is the same in both phantoms and the ratio of the fluences in water and graphite increases gradually with depth. This is because more primary particles are removed from the beam in graphite than in water at equivalent depths. To illustrate the effect of elastic nuclear interactions, two curves for primary protons are shown in figure 2.7(b); representing simulations where the elastic nuclear interactions were included and switched off by setting the energy threshold for these interactions very high. Primary protons which are elastic scattered have lower energy and larger scattering angles, therefore, their contribution is larger in the plateau region. Primary protons that are not elastic scattered have larger ranges and their contribution is larger in the Bragg peak region.

The contribution of secondary particles is different in water and in graphite, and these differences become apparent as soon as the secondary particles are produced at the surface. The difference of 1% at the surface can be mainly attributed to the contribution of alpha particles as can be seen in figure 2.6. Most of these particles travel a certain distance in the direction of the incident particles. However, given their very short range, close to the surface there is already a difference between the alpha fluence in water and graphite. As is shown in figure 2.6, the dose contribution due to alpha particles is higher in graphite than in water because the production cross section of these particles per atomic mass is larger for graphite than for water. This is consistent with data from ICRU Report 63 [37], where for an 180 MeV proton beam the alpha production cross section is approximately 25% larger in graphite than in water.

When all charged particles are considered, the fluence correction factor increases from 0.99 to 1.04 with depth. The results presented here are in agreement with the previous work performed by Lühr *et al.* [15] who found fluence corrections to be of the order of 5% in depth for high-energy proton beams using SHIELD-HIT10A Monte Carlo code. At larger depths the energy deposition from secondary particles becomes negligible in comparison with the energy deposition from primaries and all the curves converge to the value obtained for primary particles. As illustrated in figure 2.4, secondary protons escape the collecting area of the chamber and this affects the fluence corrections. This difference is about 1% in the build-up region and is in agreement with the results shown in figures 2.4 and 2.7.

For simplification and due to the good agreement between fluence method and dose method, the data of the latter have been excluded from the graphs presented in figure 2.8. A comparison between experimental data and numerical simulations of the fluence correction factor is shown in figure 2.8. The $k_{\mathrm{fl,partial}}^{\mathrm{MC}}$ factor was computed

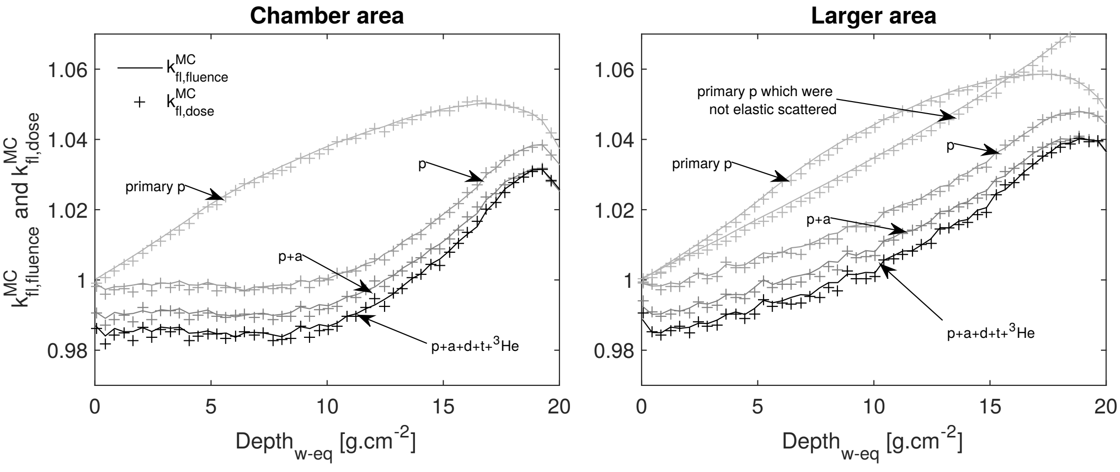

(a) (b)

Figure 2.7: Monte Carlo simulations of the fluence correction factor between water and graphite for the PTC Czech beam. Straight lines represent the fluence method (equation 2.4) and crosses represent the dose method (equation 2.3), (a) inside the area of the Bragg peak chamber and (b) in a larger area. The curves indicate the contributions of primary and secondary particles (primary p = primary protons, p = primary and secondary protons, a = alphas, d = deuterons, t = tritons and ^{3}He ions.)

to simulate the experimental setup by Monte Carlo and to study the variation of the fluence correction factor at depth, $d^{(3)}$, for a specific thickness of graphite, t_g. In the numerical simulations, absorbed doses were scored for setup 1 and compared to absorbed doses in water from setup 3. For setup 3, graphite slabs were simulated to have the same thickness and density of those used in the experiments, along with other thicknesses to obtain a more complete data set. For each slab of graphite with thickness t_g tested, its WET was calculated from the difference in ranges and the ratio between water and graphite-water absorbed dose curves was calculated at equivalent depths. For each slab of graphite, the fluence correction factor was found to be constant as a function of depth. Its variation was estimated to be 0.8% due to the statistics of the Monte Carlo simulations. When $k^{\mathrm{MC}}_{\mathrm{fl,partial}}$ is calculated in an area equal to the sensitive area of the chamber, the variation of $k^{\mathrm{MC}}_{\mathrm{fl,partial}}$ with depth increases for thicker slabs of t_g due to the difference in scattering between water and graphite. A mean value was computed to represent $k^{\mathrm{MC}}_{\mathrm{fl,partial}}$ as a function of WET, in keeping with equation 2.16. Figure 2.8 shows that $k^{\mathrm{exp}}_{\mathrm{fl,partial}}$ follows the same trend as $k^{\mathrm{MC}}_{\mathrm{fl,partial}}$. The ratio of ion chamber readings from setups 1 and 3, determined experimentally, and a ratio of doses from setups 1 and 3, calculated using Monte Carlo methods, represent a partial fluence correction factor that accounts for differences of primary and secondary proton spectra. As defined by equation

2.12, the partial fluence correction is related to the fluence correction factor, when accounting all charged particles, by the factor $F(d^{(3)})$. The range of alpha particles is very short and the ones produced in the slab of graphite, t_g, do not penetrate the water phantom in setup 3. Consequently their contribution is not accounted for in the expression of $k^{\mathrm{MC}}_{\mathrm{fl,partial}}$. All alpha particles detected in the chamber cavity were generated within the chamber geometry (wall and cavity). Therefore, for a given proton fluence, the same amount of alpha particles will be observed in the cavity irrespective of the material of the phantom is. The results show that $F(d^{(3)})$ varies from 0.98-1.00 at depth. In order to quantify $F(d^{(3)})$ experimentally, an alternative detector such as a thin-window ion chamber detector could be used to sample the generated alpha particles contribution.

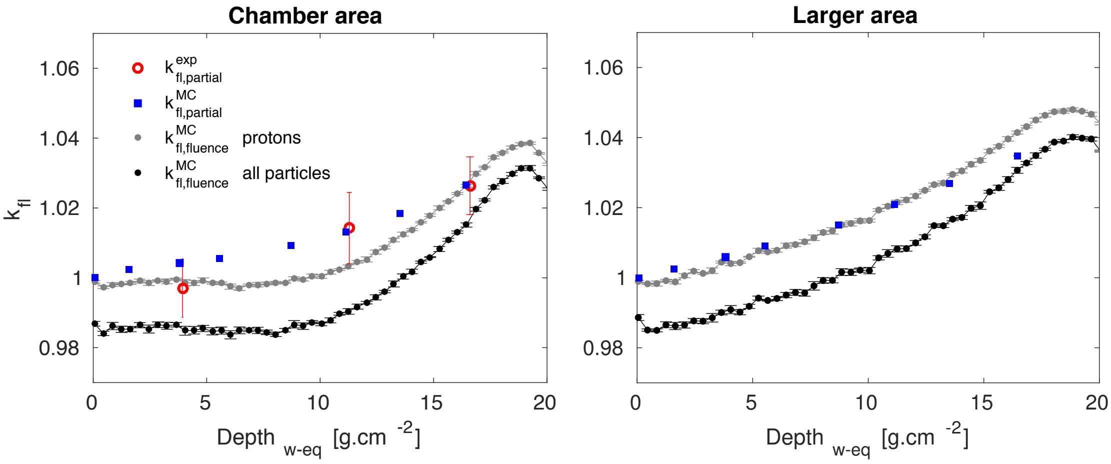

(a) (b)

Figure 2.8: Comparison between numerical simulations and experimental data of the fluence correction factor between water and graphite for the PTC Czech beam. Circles represent the values of $k^{\mathrm{exp}}_{\mathrm{fl,partial}}$ calculated experimentally (refer to equation 2.15), squares represent the values of $k^{\mathrm{MC}}_{\mathrm{fl,partial}}$ calculated using Monte Carlo methods (equation 2.16), and solid circles represent the values of $k^{\mathrm{MC}}_{\mathrm{fl,fluence}}$ (refer to equation 2.4) when taking into account the proton spectra, primary and secondary particles, in gray, and all charged particles spectra in black; (a) inside the area of the Bragg peak chamber and (b) in a larger area.

2.5.3.2 CCC beam

The results from the fluence and dose based methods are presented in figure 2.9 for the CCC beam. Quantities of interest were calculated in a volume with a sensitive area identical to that of the Roos ionization chamber and were also scored in a larger area to study the contribution of particles that scatter outside the effective area of the chamber.

The fluence corrections calculated in this study are in agreement with those of Palmans *et al.* [24]. The statistical Monte Carlo noise between the fluence and dose models is due to the scattering delivery system whose main disadvantage is the loss of a significant number of primary protons at the collimator exit. This is especially pronounced when small fields are employed as only about 3% of the initial protons are used for treatment [38]. The magnitude of the fluence correction factor, when accounting for all charged particle spectra, is approximately 0.99 at all depths inside the chamber area. When considering a larger area, it increases from 0.99 to 1.01 with depth.

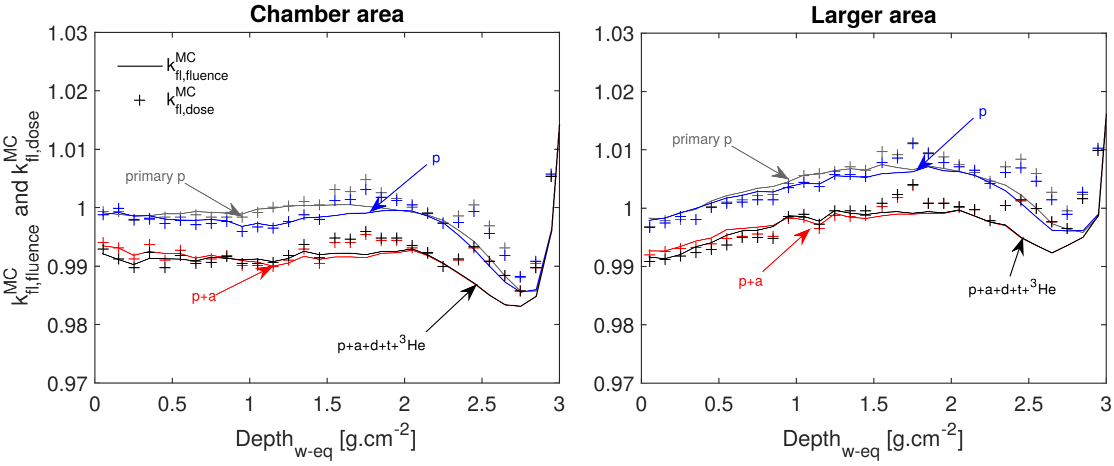

(a) (b)

Figure 2.9: Monte Carlo simulations of the fluence correction factor between water and graphite for the CCC beam. The solid lines represent the fluence method (equation 2.4) and the crosses represent the dose based method (equation 2.3), (a) inside the area of the Roos chamber and (b) in a larger area. The contributions of primary protons, primary and secondary protons, protons and alpha particles, and all charged particles are depicted in grey, blue, red and black, respectively.

A comparison between experimental data and numerical simulations of the fluence correction factor is shown in figure 2.10. A good agreement was found between partial fluence corrections measured in the experiments ($k^{\mathrm{exp}}_{\mathrm{fl,partial}}$), and those derived using Monte Carlo methods ($k^{\mathrm{MC}}_{\mathrm{fl,partial}}$). Partial fluence corrections ($k_{\mathrm{fl,partial}}$) are related with fluence corrections defined by theory ($k^{\mathrm{MC}}_{\mathrm{fl,dose}}$ and $k^{\mathrm{MC}}_{\mathrm{fl,fluence}}$) by a factor $F(d^{(3)})$ which takes values from 0.99-1.00 at depth.

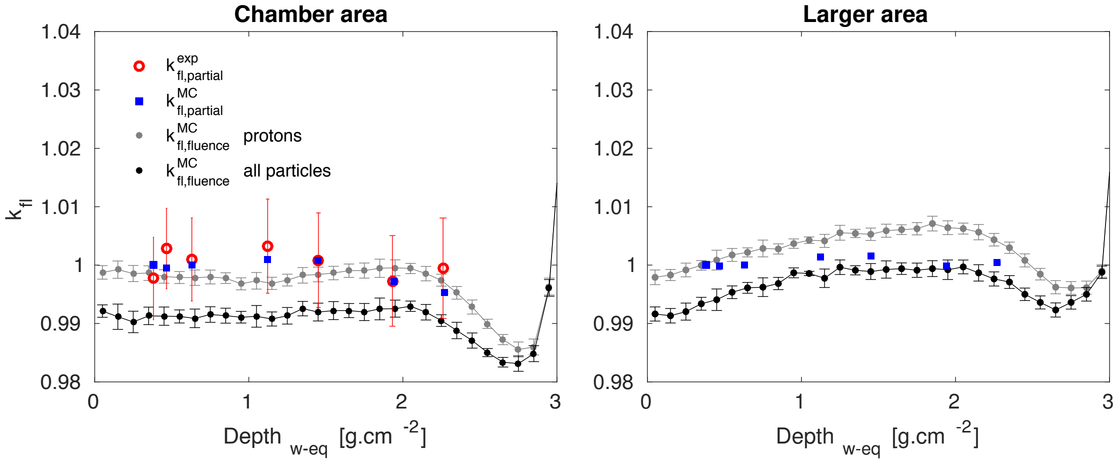

(a) (b)

Figure 2.10: Comparison between numerical simulations and experimental data of the fluence correction factor for the CCC beam. Open circles represent the values of $k^{\mathrm{exp}}_{\mathrm{fl,partial}}$ calculated experimentally (equation 2.15), squares represent the values of $k^{\mathrm{MC}}_{\mathrm{fl,partial}}$ calculated using Monte Carlo methods (equation 2.16), and solid circles represent the values of $k^{\mathrm{MC}}_{\mathrm{fl,fluence}}$ (equation 2.4) when taking into account the proton spectra, primary and secondary protons, in grey, and all charged particles spectra in black; (a) inside the area of the Roos chamber and (b) in a larger area.

2.6 Conclusions

In this work, fluence correction factors to convert absorbed dose to graphite to absorbed dose to water were determined for graphite calorimetry. Measurements were performed with a 60 MeV energy beam at CCC, and an 180 MeV at the PTC Czech and compared with Monte Carlo simulations. A mathematical formalism was presented which relates fluence corrections derived by numerical simulations using the FLUKA Monte Carlo code [16, 17] to partial fluence corrections determined experimentally.

Fluence corrections calculated by experiments are partial because they account for differences in the primary and part of the secondary particles' fluence. A correction factor, $F(d^{(3)})$, was established to relate fluence corrections as defined by theory and partial fluence corrections derived by experiment. For the PTC Czech beam, fluence corrections increased from 0.99 to 1.04 with depth. For the CCC beam, the magnitude of the fluence correction factor was approximately 0.99 at all depths when derived in an area equal to the sensitive area of the chamber used in the experiments. A larger area was also considered to study the contribution of particles that scatter outside the effective area of the chamber and fluence corrections were found to increase from 0.99 towards 1.01 in depth. Measurements were performed with narrow beams without any range modulation. Reference dosimetry in scanned proton beams is usually performed using pristine Bragg peaks, while scattered beams usually use spread-out Bragg peaks. Future investigation on the fluence correction factors will be performed with spread-out Bragg peaks.

The results are relevant to the use of water and tissue-equivalent-plastic materials in the clinic given their carbon content. The work presented here is a first step for the conversion between dose to graphite to dose to water in low- and high-energy proton beams. This work will also contribute to improved absolute proton dosimetry using a graphite calorimeter and its establishment as a primary standard.

Chapter 3

Fluence corrections for graphite calorimetry in a clinical high-energy carbon-ion beam

The work presented in this chapter is currently under review in the Physics in Medicine and Biology journal:

- **A. Lourenço**, R. Thomas, M. Homer, H. Bouchard, S. Rossomme, J. Renaud, T. Kanai, G. Royle, and H. Palmans, "Fluence correction factor for graphite calorimetry in a clinical high-energy carbon-ion beam" (currently under review in Physics in Medicine and Biology)

My contributions to this publication were as follows; experiments at the Gunma University Heavy Ion Medical Center (Japan) were performed by me with the assistance of NPL staff and local contacts; analysis and interpretation of the results and Monte Carlo simulations were performed by me under guidance of my supervisors and NPL staff; the paper was written by me and proof-read by the co-authors.

3.1 Summary

The aim of this work was to develop and adapt a formalism to determine absorbed dose to water from graphite calorimetry measurements in carbon-ion beams, as was previously proposed for proton beams in chapter 2. Fluence correction factors, k_{fl}, needed when using a graphite calorimeter to derive dose to water, were determined in a clinical high-energy carbon-ion beam. Measurements were performed in a 290 MeV/n carbon-ion beam with a field size of 11 x 11 cm^2, without modulation. In order to sample the beam, a plane-parallel Roos ionization chamber was chosen for its small collecting volume in comparison with the field size. Experimental information on fluence corrections was obtained from depth-dose measurements in water. This procedure was repeated with graphite plates in front of the water phantom. Fluence corrections were also obtained with Monte Carlo simulations through the implementation of three methods based on (i) the fluence distributions differential in energy, (ii) a ratio of calculated doses in water and graphite at equivalent depths and (iii) simulations of the experimental setup. The k_{fl} term increased in depth from 1.00 at the entrance toward 1.02 at a depth near the Bragg peak, and the average difference between experimental and numerical simulations was about 0.13%. Compared to proton beams, there was no reduction of the k_{fl} due to alpha particles because the secondary particle spectrum is dominated by projectile fragmentation. This work contributes to improving the determination of absolute dose to water from graphite calorimetry in carbon-ion beams by developing a more practical dose conversion technique.

3.2 Rationale

The quantity of interest in radiation therapy dosimetry is absorbed dose to water. The determination of this quantity must be accurate, reproducible and traceable in order to assure tumour control and mitigate normal tissue complications. Calorimeters are the recommended primary standards to measure absorbed dose in x-ray and electron beams and numerous efforts have been reported on the establishment of calorimeters as primary standard instruments for light-ion beams as well [18, 19, 39–42]. Graphite calorimeters have been developed due to their advantageous higher sensitivity and good tissue-equivalence [20–23]. However, a conversion procedure is required to determine absorbed dose to water. The latter is the disadvantage of graphite calorimetry because it increases the total uncertainty in the determination of absorbed dose to water. As mentioned in chapter 2, the conversion requires (i) the stopping-power ratio between water and graphite and (ii) the fluence correction factor, k_{fl}, that corrects for the difference between the fluence distributions at equivalent depths in the two materials [12, 15, 24]. In addition to graphite calorimetry, fluence corrections are also relevant when water-equivalent plastics are used in dosimetry [10, 15, 43, 44] and in the comparison of dose calculations performed with Monte Carlo codes, which calculate dose to tissue, and treatment planning systems, which typically calculate dose to water [45].

Rossomme *et al.* [12] performed an experimental and numerical comparison of k_{fl} values between water and graphite for an 80 MeV/n carbon-ion beam, where experimental information was obtained from ionization chamber measurements in water and graphite. In their work, the ratio of ionization chamber perturbation factors between water and graphite was assumed negligible. However, small inconsistencies between numerical and experimental data were reported which suggested that perturbation factors should be considered.

In this work, k_{fl} was determined experimentally and compared with Monte Carlo simulations for graphite calorimetry, extending previous work [12] by adding an alternative experimental setup that is independent of ionization chamber perturbation correction factors as well as by studying this topic in a broad high-energy carbon-ion beam.

3.3 Theory

3.3.1 Calculation methods for the fluence correction factor, k_{fl}

In this section the calculation methods to compute k_{fl} numerically and experimentally will be summarised.

3.3.1.1 Monte Carlo approach

In section 2.3.1 two methods to calculate fluence correction factors in proton beams, using Monte Carlo methods [24], were described. The same methods were used in this chapter for carbon-ion beams. The methods consisted of the following. The fluence method based on the fluence distributions differential in energy, $\Phi_E(E)$, in water (w) and graphite (g) at equivalent depths:

$$k_{\text{fl,fluence}}^{\text{MC}}(z_{\text{w-eq}}) = \frac{\sum_i \left[\int_{E_{\min,i}}^{E_{\max,i}} \Phi_{E,\text{w},i}^{(1)}(E) \cdot \left(\frac{S_i(E)}{\rho}\right)_{\text{w}} \cdot dE\right]}{\sum_i \left[\int_{E_{\min,i}}^{E_{\max,i}} \Phi_{E,\text{g},i}^{(2)}(E) \cdot \left(\frac{S_i(E)}{\rho}\right)_{\text{w}} \cdot dE\right]} \tag{3.1}$$

where i is the charged particle type and S/ρ is the mass stopping power. The numbers in superscript (i.e. 1 and 2) identify the setups used. In setup 1, quantities were scored in a homogenous phantom of water and in setup 2 quantities were scored in a homogenous phantom of graphite. An alternative method was also used to compute fluence correction factors based on a ratio of calculated doses:

$$k^{\mathrm{MC}}_{\mathrm{fl,dose}}(z_{\mathrm{w-eq}}) = \frac{D^{(1)}_{\mathrm{w}}(z_{\mathrm{w-eq}})}{D^{(2)}_{\mathrm{g}}(z^{(2)}_{\mathrm{g}}) \cdot s^{\mathrm{BG}}_{\mathrm{w,g},i}(\Phi^{(2)}_{\mathrm{g}})} \tag{3.2}$$

where $D^{(1)}_{\mathrm{w}}$ and $D^{(2)}_{\mathrm{g}}$ are the doses in water and graphite, respectively, and $s^{\mathrm{BG}}_{\mathrm{w,g},i}(\Phi^{(2)}_{\mathrm{g}})$ is the water-to-graphite Bragg-Gray stopping-power ratio. Depths in setups 1, $z^{(2)}_{\mathrm{w}}$, and 2, $z^{(2)}_{\mathrm{g}}$, are related by the ratio of ranges in each setup. These methods were first implemented by Palmans *et al.* [24] for low-energy proton beams.

3.3.1.2 Graphite phantom approach

Similar to Palmans *et al.* [24], Rossomme *et al.* [12] calculated fluence correction factors between water and graphite using setups 1 and 2. Experimental information on fluence corrections was obtained from ionization chamber measurements employing the following formalism. By application of the Bragg-Gray cavity theory with a Spencer-Attix stopping power ratio, absorbed dose to medium $D^{(n)}_{m}$, in a given setup n and at a depth of measurement $z^{(n)}_{m}$, is related to the ionization chamber readings $M^{(n)}$:

$$D^{(n)}_{m}(z^{(n)}_{m}) = M^{(n)}(z^{(n)}_{m}) \cdot \frac{W^{(n)}_{\mathrm{air}}/e}{m_{\mathrm{air}}} \cdot s^{\mathrm{SA}}_{m,\mathrm{air}}(\Phi^{(n)}_{m}) \cdot p^{(n)}_{m}(z^{(n)}_{m}) \tag{3.3}$$

where $W^{(n)}_{\mathrm{air}}$ is the mean energy to form an ion pair in air, e is the charge of the electron, m_{air} is the mass of air in the chamber, $s^{\mathrm{SA}}_{m,\mathrm{air}}(\Phi^{(n)}_{m})$ is the medium-to-air Spencer-Attix stopping-power ratio for the fluence in medium m, and $p^{(n)}_{m}$ the perturbation correction factor for the chamber in medium m. Note that Spencer-Attix stopping powers consider the production of secondary electrons (or delta-rays) that have enough energy to travel away from the point where they were generated before their energy is deposited. An energy threshold is defined above which secondary electrons are transported and their energy is deposited away from the initial site of interaction and restricted stopping powers are used to account for such energy exchanges. On the other hand, Bragg-Gray stopping powers consider that secondary electrons deposit their energy locally. The energy threshold is set to infinity and unrestricted stopping powers are used.

Using equation 3.3, the ratio of ionization chamber readings between water and graphite at equivalent depths is given by:

$$\frac{M^{(1)}(z_{\mathrm{w-eq}})}{M^{(2)}(z_{\mathrm{g}}^{(2)})} = \frac{D_{\mathrm{w}}^{(1)}(z_{\mathrm{w-eq}})}{D_{\mathrm{g}}^{(2)}(z_{\mathrm{g}}^{(2)}) \cdot \frac{W_{\mathrm{air}}^{(1)}/e}{W_{\mathrm{air}}^{(2)}/e} \cdot \frac{s_{\mathrm{w,air}}^{\mathrm{SA}}(\Phi_{\mathrm{w}}^{(1)})}{s_{\mathrm{g,air}}^{\mathrm{SA}}(\Phi_{\mathrm{g}}^{(2)})} \cdot \frac{p_{\mathrm{w}}^{(1)}(z_{\mathrm{w-eq}})}{p_{\mathrm{g}}^{(2)}(z_{\mathrm{g}}^{(2)})}} \tag{3.4}$$

By multiplying and dividing the denominator on the right hand side by $s_{\mathrm{w,air}}^{\mathrm{BG}}(\Phi_{\mathrm{w}}^{(1)}) \cdot s_{\mathrm{g,air}}^{\mathrm{BG}}(\Phi_{\mathrm{g}}^{(2)}) \cdot s_{\mathrm{w,air}}^{\mathrm{BG}}(\Phi_{\mathrm{g}}^{(2)})$, one obtains:

$$\frac{M^{(1)}(z_{\mathrm{w-eq}})}{M^{(2)}(z_{\mathrm{g}}^{(2)})} = \frac{D_{\mathrm{w}}^{(1)}(z_{\mathrm{w-eq}})}{D_{\mathrm{g}}^{(2)}(z_{\mathrm{g}}^{(2)}) \cdot s_{\mathrm{w,g},i}^{\mathrm{BG}}(\Phi_{\mathrm{g}}^{(2)})} \cdot \frac{W_{\mathrm{air}}^{(2)}/e}{W_{\mathrm{air}}^{(1)}/e} \cdot \frac{\frac{s_{\mathrm{g,air}}^{\mathrm{SA}}(\Phi_{\mathrm{g}}^{(2)})}{s_{\mathrm{g,air}}^{\mathrm{BG}}(\Phi_{\mathrm{g}}^{(2)})}}{\frac{s_{\mathrm{w,air}}^{\mathrm{SA}}(\Phi_{\mathrm{w}}^{(1)})}{s_{\mathrm{w,air}}^{\mathrm{BG}}(\Phi_{\mathrm{w}}^{(1)})}} \cdot \frac{s_{\mathrm{w,air}}^{\mathrm{BG}}(\Phi_{\mathrm{g}}^{(2)})}{s_{\mathrm{w,air}}^{\mathrm{BG}}(\Phi_{\mathrm{w}}^{(1)})} \cdot \frac{p_{\mathrm{g}}^{(2)}(z_{\mathrm{g}}^{(2)})}{p_{\mathrm{w}}^{(1)}(z_{\mathrm{w-eq}}^{(1)})} \tag{3.5}$$

The following assumptions were made: (i) the ratio of W_{air} values between the two setups differed from unity by a negligible amount, (ii) the ratio of two ratios of Spencer-Attix and Bragg-Gray stopping-power ratios differed from unity by a negligible amount, (iii) the ratio of Bragg-Gray stopping-power ratios for different fluences differed from unity by a negligible amount and (iv) perturbation factors between water and graphite differed from unity by a negligible amount. Based on these principles, fluence correction factors were calculated experimentally in a low-energy carbon-ion beam by a ratio of ionization curves in water ($M^{(1)}$) and graphite ($M^{(2)}$) [12]:

$$k_{\mathrm{fl,Rossomme}}^{\mathrm{exp}}(z_{\mathrm{w-eq}}) = \frac{M^{(1)}(z_{\mathrm{w-eq}})}{M^{(2)}(z_{\mathrm{g}}^{(2)})} \approx k_{\mathrm{fl,dose}}^{\mathrm{MC}} \tag{3.6}$$

The first assumption is supported by the fact that the spectra between setups at equivalent depths are marginally different and the short range of secondary electrons supports the second assumption. The third assumption is supported by the fact that the stopping-power ratios vary little with energy so for the two spectra, which are very similar, the stopping-power ratios are likely to be almost equal [4, 15]. The fourth assumption cannot be satisfied; small inconsistencies between numerical and experimental data were reported by Rossomme *et al.* [12], who suggested that perturbation factors should be included in the analysis.

3.3.1.3 Depth-averaging method

In chapter 2, another approach was introduced to measure fluence correction factors experimentally between water and graphite in proton beams. Here, the same formalism was applied to calculate fluence corrections between water and graphite in carbon-ion beams. The application of this methodology to carbon-ion beams is detailed in chapter 5.

In this approach an alternative setup was used over setup 2. In this alternative setup, referred to as setup 3, measurements were performed in a water phantom after passing through graphite slabs of variable thicknesses (figure 3.1). Rewriting equation 3.4 using setups 1 and 3 gives:

$$\frac{M^{(1)}(z_{\mathrm{w}}^{(1)})}{M^{(3)}(d^{(3)},t_{\mathrm{g}})} = \frac{D_{\mathrm{w}}^{(1)}(z_{\mathrm{w}}^{(1)})}{D_{\mathrm{w}}^{(3)}(d^{(3)},t_{\mathrm{g}}) \cdot \frac{W_{\mathrm{air}}^{(1)}/e}{W_{\mathrm{air}}^{(3)}/e} \cdot \frac{s_{\mathrm{w,air}}^{\mathrm{SA}}(\Phi_{\mathrm{w}}^{(1)})}{s_{\mathrm{w,air}}^{\mathrm{SA}}(\Phi_{\mathrm{w}}^{(3)})} \cdot \frac{p_{\mathrm{w}}^{(1)}(z_{\mathrm{w}}^{(1)})}{p_{\mathrm{w}}^{(3)}(d^{(3)},t_{\mathrm{g}})}} \tag{3.7}$$

where $d^{(3)}$ is the depth of measurement in setup 3 for a particular graphite thickness t_{g}. Depths in setups 1 and 3 are related by the difference of ranges. The assumptions were made that (i) the ratio of W_{air} values between setups 1 and 3 differed from unity by a negligible amount, (ii) the ratio of Spencer-Attix stopping-power ratios for $\Phi_{\mathrm{w}}^{(1)}$ and $\Phi_{\mathrm{w}}^{(3)}$ differed from unity by a negligible amount, (iii) the ratio of ionization chamber perturbation factors differed from unity by a negligible amount and (iv) when $d^{(3)} = 0$ and $z_{\mathrm{g}}^{(2)} = t_{\mathrm{g}}$, the fluence in setup 3 equals the fluence in setup 2, $\Phi_{\mathrm{w}}^{(3)}(0,t_{\mathrm{g}}) \approx \Phi_{\mathrm{g}}^{(2)}(t_{\mathrm{g}})$ (figure 3.1). Similar arguments to those described in section 3.3.1.2 support the first and second assumptions, and the fact that ionization chamber measurements are always performed in water supports the third assumption. Moreover, Verhaegen and Palmans [8] showed that ionization chamber perturbation factors have only a slight variation with energy.

Based on assumption (iv), it will be shown in chapter 5 (section 5.3.2) that for carbon-ion beams the ratio between dose in setup 3, $D_{\mathrm{w}}^{(3)}(0,t_{\mathrm{g}})$, and dose in setup 2, $D_{\mathrm{g}}^{(2)}(t_{\mathrm{g}})$, is approximately equal to the water-to-graphite Bragg-Gray stopping-power ratio, $s_{\mathrm{w,g}}^{\mathrm{BG}}(\Phi_{\mathrm{g}}^{(2)})$. Therefore, the fluence correction factor can be calculated by the ratio of ionization chamber readings in setups 1 and 3:

$$k_{\mathrm{fl,depth}}^{\mathrm{exp}}(t_{\mathrm{g,w-eq}}) = \frac{M^{(1)}(z_{\mathrm{w}}^{(1)})}{M^{(3)}(0,t_{\mathrm{g}})} \approx \frac{D_{\mathrm{w}}^{(1)}(z_{\mathrm{w}}^{(1)})}{D_{\mathrm{w}}^{(3)}(0,t_{\mathrm{g}})} \approx \frac{D_{\mathrm{w}}^{(1)}(z_{\mathrm{w-eq}})}{D_{\mathrm{g}}^{(2)}(z_{\mathrm{g}}^{(2)}) \cdot s_{\mathrm{w,g},i}^{\mathrm{BG}}(\Phi_{\mathrm{g}}^{(2)})} \approx k_{\mathrm{fl,dose}}^{\mathrm{MC}} \tag{3.8}$$

where $t_{\mathrm{g,w-eq}}$ is the water-equivalence thickness of the graphite slab t_{g}, derived from the difference of ranges between setups 1 and 3. For a particular graphite slab t_{g} tested experimentally, the results indicated that the ratio $M^{(1)}(z_{\mathrm{w}}^{(1)})/M^{(3)}(d^{(3)},t_{\mathrm{g}})$ varies little with the depth of measurement $d^{(3)}$, thus a mean value was derived for N depths:

$$k_{\mathrm{fl,depth}}^{\mathrm{exp}}(t_{\mathrm{g,w-eq}}) \approx \frac{1}{N}\sum_{j=1}^{N} \frac{M^{(1)}(z_{\mathrm{w}}^{(1)})}{M^{(3)}(d_j^{(3)},t_{\mathrm{g}})} \tag{3.9}$$

Here, this approach is referred to as the depth-averaging method and it was used to determine $k_{\text{fl}}^{\text{exp}}$ experimentally. Note that values near the Bragg peak were not considered since the effect of positioning errors is critical in that region due to high dose gradients. By testing graphite slabs of variable thicknesses t_{g}, the variation of the fluence correction factor with depth was studied. The depth-averaging approach was also applied to the results of Monte Carlo simulations of setups 1 and 3:

$$k_{\text{fl,depth}}^{\text{MC}}(t_{\text{g,w-eq}}) \approx \frac{1}{N}\sum_{j=1}^{N}\frac{D_{\text{w}}^{(1)}(z_{\text{w}}^{(1)})}{D_{\text{w}}^{(3)}(d_j^{(3)}, t_{\text{g}})} \tag{3.10}$$

In chapter 2, the ratio of ionization chamber readings between setups 1 and 3 was used to obtain fluence corrections experimentally in clinical proton beams. The results showed that fluence corrections obtained experimentally, accounted for the primary and part of the secondary particle spectra and, therefore, represented partial fluence corrections. Indeed, in proton beams, the energy of alpha particles, emitted by target fragmentation, is not sufficient to penetrate the wall of the ionization chamber and these particles are not accounted for in the experimental fluence correction factor. A correction factor F was established to relate fluence corrections defined theoretically to partial fluence corrections measured experimentally. However, in the case of a high-energy carbon-ion beam, the energies of secondary projectile fragments are large enough to cross the chamber wall [46] and fluence corrections obtained from experiments will thus include all charged particles, i.e. $F = 1$ and $\Phi_{\text{w}}^{(3)}(0, t_{pl}) \approx \Phi_{pl}^{(2)}(t_{pl})$, with the exception of heavy particles from target fragmentation which are less abundant in these beams.

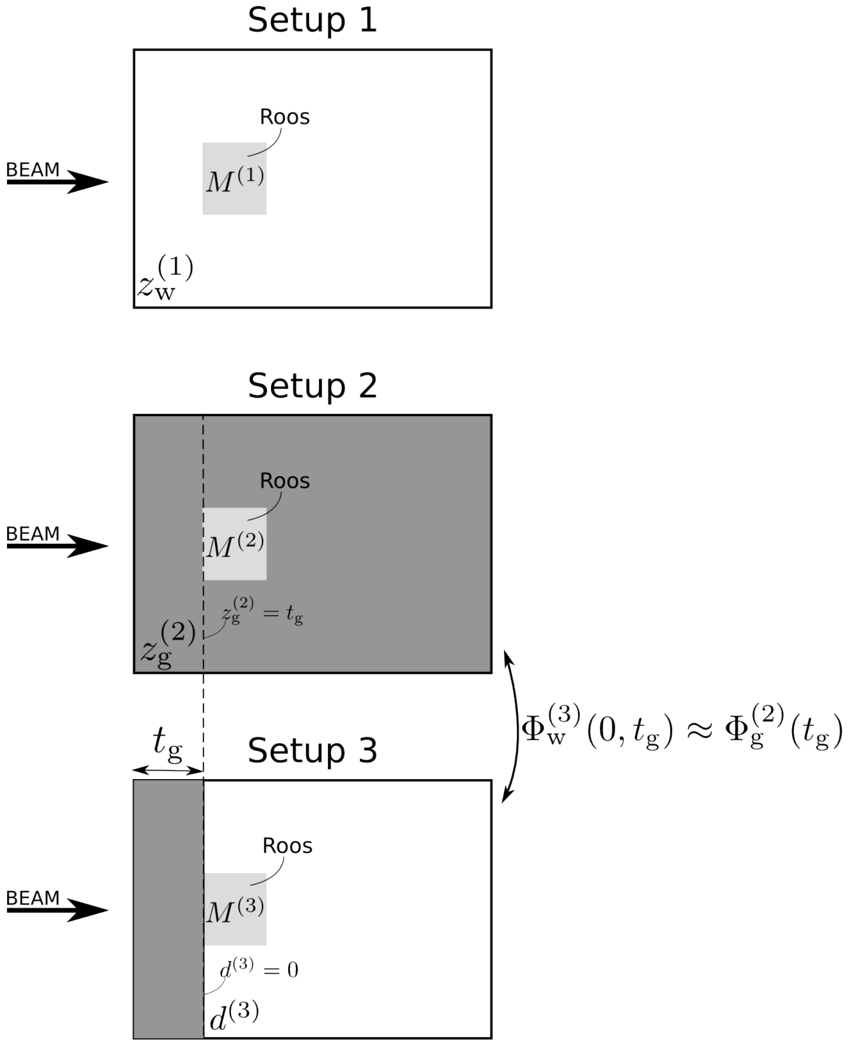

Figure 3.1: Schematic representation of setups 1, 2 and 3 and respective relation between setups 2 and 3.

3.4 Methods

3.4.1 Experimental fluence correction factor, $k^{\mathrm{exp}}_{\mathrm{fl,depth}}$

Measurements were performed at the Gunma University Heavy Ion Medical Center (GHMC), Japan [47–49], using a carbon-ion beam with mean energy of 290 MeV/n at the source. Measurements were performed with a field size of 11 x 11 cm^2, without modulation. A plane-parallel Roos ionization chamber (PTW type 34001, radius of the collecting volume = 0.75 cm) was used due to its small collecting volume in comparison with the field size (central axis measurements). For monitoring purposes a cylindrical Farmer ionization chamber (PTW type 30011) was placed in the corner of the collimator exit. Measurements were performed with a constant source-to-detector distance (SDD), so no correction was required for the inverse square law. Experimental information on fluence correction factors was obtained from ionization chamber measurements in water. This procedure was repeated for graphite plates (t_{g}) with 0.09, 1.9, 5.5, 7.4 and 9.2 g.cm^{-2} thicknesses placed in front of the water phantom (figure 3.1).

The standard uncertainty on each value of $k^{\mathrm{exp}}_{\mathrm{fl,depth}}$ was estimated to be 0.24% and the sources of uncertainties are listed in table 1, where $s_{\overline{k^{\mathrm{exp}}_{\mathrm{fl,depth}}}}$ represents the standard deviation of the mean value $k^{\mathrm{exp}}_{\mathrm{fl,depth}}$ calculated using equation 3.9.

Table 3.1: Experimental uncertainties.

Standard uncertainties (%)	Type A (%)	Type B (%)
Repeatability: Roos/Monitor	0.17	-
Temperature	-	0.05
Pressure	-	0.05
$s_{\overline{k^{\mathrm{exp}}_{\mathrm{fl,depthl}}}}$	-	0.15
Overall	**0.17**	**0.17**
Combined	**0.24**	

3.4.2 Numerical fluence correction factor, $k^{\mathrm{MC}}_{\mathrm{fl,fluence}}$, $k^{\mathrm{MC}}_{\mathrm{fl,dose}}$ and $k^{\mathrm{MC}}_{\mathrm{fl,depth}}$

Fluence corrections were also obtained with Monte Carlo simulations through the implementation of three methods based on (i) the fluence distributions differential in energy, thus defining $k^{\mathrm{MC}}_{\mathrm{fl,fluence}}$ (refer to equation 3.1), (ii) a ratio of calculated doses in water and graphite at equivalent depths, thus defining $k_{\text{fl,dose}}^{\text{MC}}$ (refer to equation 3.2), and (iii) simulations of the experimental setup, thus defining $k_{\text{fl,depth}}^{\text{MC}}$ (refer to equation 3.10).

Simulations were performed with FLUKA version 2011.2c.3 [16, 17], using the default card HADRONTHErapy and delta-ray production set to infinite threshold. For the calculation of $k_{\text{fl,dose}}^{\text{MC}}$ and $k_{\text{fl,fluence}}^{\text{MC}}$, depth-dose distributions and fluence spectra differential in energy were scored in homogenous phantoms of water (setup 1) and graphite (setup 2). For the calculation of $k_{\text{fl,depth}}^{\text{MC}}$, setup 3 was also simulated in FLUKA. Dose and fluence were scored in bins of 0.007 cm and 0.1 cm, respectively, throughout the phantoms. The beam energy and spread were tuned against experimental data for 265 MeV/n and σ=0.75 MeV, respectively, at the phantom surface. A broad carbon-ion beam of 11 x 11 cm^2 without modulation was simulated, with the radius of the scoring region equal to the radius of the Roos chamber used in the experiments. In addition, a beam without divergence was considered since the measurements were performed at constant SDD. A total number of 25x10^6 carbon-ion histories was required for each setup to obtain a standard uncertainty (type A) below 0.3%. Type B Monte Carlo uncertainties include stopping powers and interaction cross-sections uncertainties [44] and were note considered. The ICRU Report 73 [50] compared stopping powers from different models with experimental data and values agreed within 10%. In the calculation of the fluence correction factor using Monte Carlo methods (equations 3.1 and 3.2), the stopping powers are used in a ratio and thus uncertainties related with stopping powers will be strongly correlated. With regards to interaction cross-sections uncertainty, Böhlen *et al.* [32] compared nuclear models from FLUKA with experimental data for carbon-ion therapy and the results showed reasonable agreement between FLUKA and experimental data.

3.5 Results and discussion

3.5.1 Monte Carlo simulations: $k_{\text{fl,fluence}}^{\text{MC}}$ and $k_{\text{fl,dose}}^{\text{MC}}$

In figure 3.2, the contributions of primary and secondary particles to the absorbed dose calculated with FLUKA are shown for a 265 MeV/n carbon-ion beam in water (straight lines) and graphite (solid lines). Primary carbon ions that undergo an elastic nuclear interaction are considered as primaries and all products from a non-elastic nuclear interaction are considered secondary, including charge-changing products. Primary carbon ions do not contribute to the dose tail behind the Bragg peak, to which mostly lighter fragments ($1 \leq Z \leq 2$) contribute. In carbon-ion beams, the secondary particle spectrum is dominated by projectile fragments emerging with similar velocity to the projectile but with larger ranges. Experimental data from Haettner *et al.* [46] showed that fragments with Z=1 (hydrogen nuclei) and Z=2 (helium nuclei) have a larger contribution to the dose than fragments with Z=3 (lithium nuclei), Z=4 (beryllium nuclei), and Z=5 (boron nuclei). However, larger uncertainties were reported for fragments with Z=5. Our results are in agreement with their findings, with the exception of fragments with Z=5, where a contribution of the same order of magnitude as for Z=1 and Z=2 was found. Previous Monte Carlo studies from Kempe *et al.* [51] and Rossomme *et al.* [12] show similar results to ours. The latter reported a discontinuity in the depth dose curve for Z=2 fragments using Geant4 and concluded it could be the result of artefacts due to the implementation of interaction cross sections. In our case, using FLUKA, depth-dose distributions from all fragments follow a smooth curve.

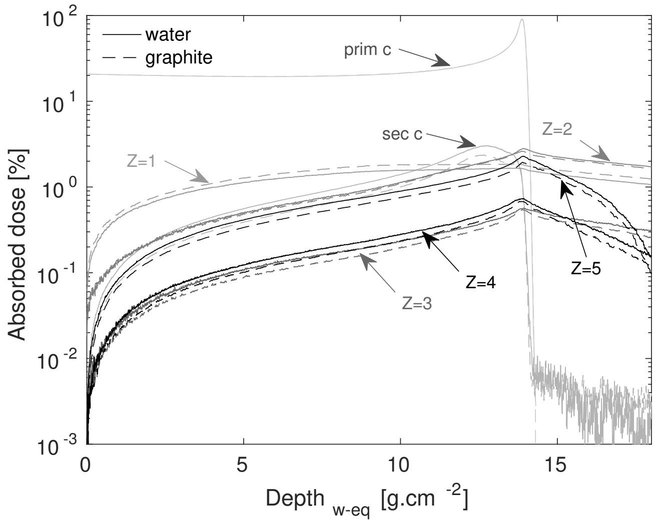

Figure 3.2: Depth-dose distributions for a 265 MeV/n carbon-ion beam in a water (solid lines) and graphite (dashed lines) phantoms for different particles (prim c = primary carbon ions, sec c = secondary carbon ions, and particles with atomic numbers Z=1, Z=2, Z=3, Z=4 and Z=5). Curves were normalised to the maximum of the total dose and are presented on a logarithmic scale.

Figure 3.3 shows the calculated fluence correction factor between water and graphite as a function of depth for different sets of particles. A good agreement was found between the fluence, $k^{\mathrm{MC}}_{\mathrm{fl,fluence}}$, and dose, $k^{\mathrm{MC}}_{\mathrm{fl,dose}}$, methods (0.05% difference). At the surface, the primary carbon-ion fluence is the same in both phantoms. When all particles are considered, there is a slight reduction of the k_{fl} term (0.998) due to the very short range of secondary particles from target fragmentation. Compared to proton beams [24], the reduction of the k_{fl} term at the surface is less pronounced for carbon-ion beams because the secondary particle spectrum is much more dominated by projectile fragmentation and thus secondary particles emerge with larger ranges.

When considering only primary carbon ions, k_{fl} decreases slightly in depth (toward 0.99) because more primary particles are removed from the beam in water than in graphite. When also secondary carbon ions are included, k_{fl} increases towards 1.02 at a depth near the Bragg peak since the total charge-changing cross-sections are higher in water than in graphite [52]. Therefore, the dose contribution of secondary carbon ions is also higher in water than in graphite as shown in figure 3.2. The same applies when a different set of charged particles are included, with exception of fragments with Z=1 of which the dose contribution is higher in graphite than in water (figure 3.2), thus there is a reduction in the k_{fl} factor when these particles are included.

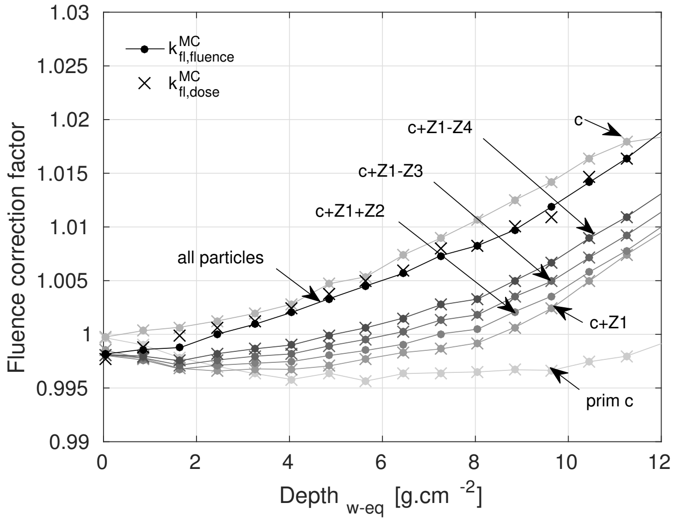

Figure 3.3: Fluence correction factor between water and graphite derived for different set of particles (prim c = primary carbon ions, c = primary and secondary carbon ions, and particles with atomic numbers Z=1 (Z1), Z=2 (Z2), Z=3 (Z3), Z=4 (Z4) and Z=5 (Z5)). Circles represent the fluence-based method and crosses represent the dose-based method.

3.5.2 Comparison between Monte Carlo simulations and experimental data

A comparison between experimental data and numerical simulations of the fluence correction factor is presented in figure 3.4. The results from different calculation methods are presented in this figure: the fluence- and depth-averaging approaches derived from Monte Carlo simulations and the depth-averaging approach derived from experimental data. For all methods, the fluence correction factor increased with depth from 1.00 to 1.02. The average difference between experimental and numerical simulations was of the order of 0.11% for the depth-averaging method and 0.16% for the fluence method. These results suggest that k_{fl} obtained experimentally includes all charged particles contrary to the case of protons (chapter 2). Similar results were found by Rossomme *et al.* [12] for a clinical 80 MeV/n carbon-ion beam using Geant4 and experimental data. In their work, fluence corrections were obtained using setups 1 and 2, assuming that the ratio of perturbations factors between water and graphite was negligible. However, small inconsistencies between numerical and experimental data were reported, which suggested that perturbation factors should be included in the analysis. In this work, by always measuring ionization chamber readings in water, using setups 1 and 3, it can be assumed that perturbation factors are the same for both setups.

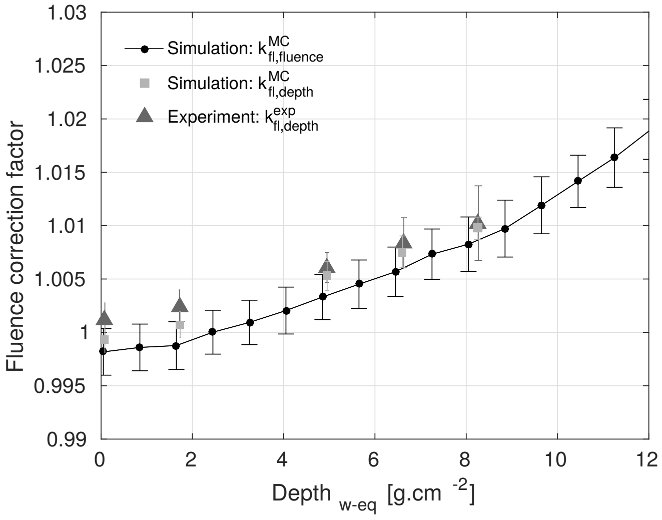

Figure 3.4: Fluence correction factor between water and graphite derived using different methods. Circles represent the fluence-based method (all particles), $k^{\text{MC}}_{\text{fl,fluence}}$, squares and triangles represent the depth-averaging method obtained from simulations, $k^{\text{MC}}_{\text{fl,depth}}$, and experiments, $k^{\text{exp}}_{\text{fl,depth}}$, respectively.

3.6 Conclusions

In this work, a formalism was developed and adapted to derive absorbed dose to water, using a graphite calorimeter in carbon-ion beams. This procedure has the advantage of involving measurements being done independently from ionization chamber perturbation factors caused by the use of different phantom materials. Fluence corrections, needed for the conversion of dose to graphite from a graphite calorimeter to dose to water, were measured experimentally in a high-energy carbon-ion beam and compared with numerical simulations.

The results showed that k_{fl} obtained from experiments includes all charged particles contrary to the case of protons (see chapter 2). For graphite, the fluence correction factor increased in depth from 1.00 towards 1.02 and the average difference between experimental and numerical simulations was of the order of 0.13%. The magnitude of differences between methods supports the use of FLUKA to compute fluence correction factors for carbon-ion beams between water and graphite.

NPL is currently working on the establishment of a graphite calorimeter as a primary standard instrument for light-ion beams. The calibration of user ionization chambers will be performed directly against the graphite calorimetry in the user beam. The work presented here will feed into the establishment of graphite calorimetry in carbon-ion beams by using a more practical experimental setup for the conversion of dose to graphite to dose to water.

Chapter 4

Water-equivalence of plastic materials in proton beams

The work presented in this chapter is currently under review in the Physics in Medicine and Biology journal:

- **A. Lourenço**, D. Shipley, N. Wellock, R. Thomas, H. Bouchard, A. Kacperek, F. Fracchiolla, S. Lorentini, M. Schwarz, N. MacDougall, G. Royle, and H. Palmans, "Evaluation of the water-equivalence of plastic materials in low- and high-energy clinical proton beams (currently under review in Physics in Medicine and Biology)

My contributions to this publication were as follows; novel water-equivalent plastics were designed by me and produced in collaboration with St Bartholomew's Hospital (UK); experiments at the Clatterbridge Cancer Centre (UK) and the Trento Proton Therapy Center (Italy) were performed by me with the assistance of NPL staff and local contacts; Geant4 simulations were conducted by David Shipley (NPL, UK) based on my simulation plans; analysis and interpretation of the results and FLUKA Monte Carlo simulations were performed by me under guidance of my supervisors and NPL staff; the paper was written by me and proof-read by the co-authors.

4.1 Summary

Water-equivalent plastics designed for high-energy photon and electron beam dosimetry are currently also used in proton beams. The aim of this work was to

evaluate the water-equivalence of new trial plastics designed specifically for light-ion beam dosimetry as well as commercially available plastics in clinical proton beams. The water-equivalence of materials was tested by computing a plastic-to-water conversion factor, $H_{pl,\mathrm{w}}$. Trial materials were characterized experimentally in 60 MeV and 226 MeV un-modulated proton beams and the results were compared with Monte Carlo simulations using the FLUKA code. For the high-energy beam, a comparison between the trial plastics and various commercial plastics was also performed using FLUKA and Geant4 Monte Carlo codes. Experimental information was obtained from laterally integrated depth-dose ionization chamber measurements in water, with and without plastic slabs with variable thicknesses in front of the water phantom. Fluence correction factors, k_{fl}, between water and various materials were also derived using the Monte Carlo method. For the 60 MeV proton beam, $H_{pl,\mathrm{w}}$ and k_{fl} factors were within 1% from unity for all trial plastics. For the 226 MeV proton beam, experimental $H_{pl,\mathrm{w}}$ values deviated from unity by a maximum of about 1% for the three trial plastics and experimental results showed no advantage regarding which of the plastics was the most equivalent to water. Different magnitudes of corrections were found between Geant4 and FLUKA for the various materials in consideration due mainly to the use of different non-elastic nuclear data. Nevertheless, for the 226 MeV proton beam, $H_{pl,\mathrm{w}}$ correction factors were within 2% from unity for all the materials. Considering the results from the two Monte Carlo codes, PMMA and trial plastic #3 had the smallest $H_{pl,\mathrm{w}}$ values, where maximum deviations from unity were 1%, however, PMMA range differed by 16% from that of water. Overall, k_{fl} factors were deviating more from unity than $H_{pl,\mathrm{w}}$ factors and could amount to a few percent for some materials depending on the code used.

4.2 Rationale

Water-equivalent plastics offer advantages for dosimetry over the reference material, water, such as the convenience of realizing the experimental setup and better positioning accuracy. As stated in the IAEA TRS-398 Code of Practice [4] two steps are involved in the conversion of ionization chamber readings in a plastic phantom to dose to water in a water phantom:

(i) the determination of the range scaling factor, c_{pl}, to convert depth in a plastic phantom to the corresponding depth in a water phantom, and

(ii) the application of a fluence scaling factor, h_{pl}, to convert ionization chamber readings in a plastic phantom to the equivalent reading in a water phantom.

While the c_{pl} factor is calculated by the ratio of continuous-slowing-down approximation (CSDA) ranges in water and in plastic, the h_{pl} factor is derived from the ratio of ionization chamber readings in water and in plastic at equivalent depths [4].

At present, only a limited amount of c_{pl} and h_{pl} values are available in the literature because their experimental determination is a time consuming process requiring the acquisition of Bragg peak curves in both the plastic and water, the former involving the insertion of numerous plates one by one to establish the distal edge with sufficient spatial resolution. Therefore, in proton beams, the water-equivalence thickness (WET) is often measured experimentally as an approximation of c_{pl}, where WET values are calculated by the difference of ranges in water, and in water with the material of interest in front. This methodology allows more efficient measuring since ionization chamber readings need to be measured only in water [53, 54]. Zhang *et al.* [55] compared measured WET values with those derived analytically in heavy-ion beams. The results obtained showed that analytical methods could well predict experimental values. Palmans *et al.* [10] conducted a study to measure h_{pl} factors for PMMA with reference to water in 75 and 191 MeV proton beams. For the low-energy beam, measured corrections were smaller than 1% and for the high-energy beam maximum corrections were of the order of 3%. Similar results were obtained by Al-Sulaiti *et al.* [14] for the water-equivalent plastic PWDT.

Differences in non-elastic nuclear interactions between different elements lead to differences in the fluence in water and low-Z materials such as plastics. Thus, the water equivalence of plastics can also be expressed in terms of the fluence correction factor, k_{fl}, which corrects for the differences in fluence. It can also be interpreted as a conversion factor between dose to plastic in a plastic phantom to dose to water in a water phantom [10, 24]. Fluence correction factors with reference to water were investigated using Monte Carlo simulations by Palmans *et al.* [10] for PMMA and polystyrene, by Al-Sulaiti *et al.* [13, 14] for A-150, PMMA, PW, PWDT and WT1 and by Lühr *et al.* [15] for bone and PMMA. Summarizing these findings, fluence corrections were of the order of 1% for low-energy proton beams, while for high-energy proton beams corrections from 2% to 5% were found.

As became evident from these studies, correction factors need to be considered to accurately determine dose to water from measurements performed in a plastic. For high-energy photon and electron beams, White *et al.* [56–58] and Constantinou *et al.* [59] have developed numerous water- and tissue-equivalent plastics such that similar corrections were negligible. The plastics consisted of epoxy resins mixed with low-Z compounds to form a mixture with radiation interaction properties similar to those of water or tissue. Based on this work, WT1 and WTe were designed and commercialised as water-equivalent plastics for high-energy photon and electron beams, respectively. A number of other plastics are currently used in the clinic as water substitutes – Gammex 457-CTG (CTG Solid Water®: GAMMEX, Middleton, WI, USA), Virtual Water™ (Med-Cal, Middleton, WI, USA), Plastic Water® (CIRS, Norfolk, VA, USA), PMMA and polyethylene, and as tissue substitutes – RANDO® phantom (The Phantom Laboratory, Salem, NY, USA) and A-150 tissue-equivalent plastic.

In this work, new water-equivalent plastics were developed specifically for light-ion beams. In the design phase, the propagation of proton beams through phantom materials was simulated using an analytical model. Three epoxy-resin based mixtures were then produced and experimentally characterized in low- and high-energy clinical proton beams. A plastic-to-water conversion factor $H_{pl,\mathrm{w}}$ was established and measured as an approximation of h_{pl}, using a more practical experimental setup from which WET values could also be derived. Experimental results were compared with Monte Carlo simulations using FLUKA and Geant4. Material physical properties of the trial compositions were calculated and compared to those of water and other commercially available plastics.

4.3 Analytical model

4.3.1 Formalism

To find plastic compositions equivalent to water, an analytical model was implemented in MATLAB to compute an approximation of the fluence correction factor between water and any other material for proton beams. The analytical model was used as a tool to quickly test a wide range of compositions and with any promising composition then fully simulated in Monte Carlo for more detailed evaluation. A value of unity for the fluence correction factor between water and plastic material indicates that no correction needs to be applied between media.

The model estimates the energy deposited by primary protons and secondary particles from non-elastic nuclear interactions. Primary particles are considered to travel along a straight line, with no scattering or energy straggling and energy losses are assumed to take place through the continuous slowing down approximation. Also, secondary particles are not transported and their energy is deposited at the point of interaction. Moreover, the energy transferred to neutrons and gamma rays does not contribute to dose.

The analytical model used was based on the work of Al-Sulaiti *et al.* [13] and Palmans *et al.* [24], and it was extended to calculate the fluence correction factor between water (w) and any plastic (*pl*), using elemental composition in fraction by weight. It is applicable to any proton energy but since at higher energies the dose contribution and range of secondary particles becomes larger, the approximations will be further from reality than for a low-energy beam. The analytical model implemented is described as follows.

- Mass collision stopping-power was computed using the definition from ICRU Report 37 [60] and ICRU Report 49 [27]:

  $$(1/\rho)S_{\mathrm{col}} = \frac{4\pi \mathrm{r_e}^2\mathrm{mc}^2}{\mathrm{u}}\frac{1}{\beta^2}\frac{Z}{A}z^2 \times \left[\ln\left(\frac{2\mathrm{mc}^2\beta^2}{(1-\beta^2)I}\right) - \beta^2\right] \tag{4.1}$$

  where $\mathrm{r_e}$ is the classical electron radius, mc^2 the electron rest energy, u the atomic mass unit, z the proton charge in units of electron charge, Z/A the ratio of number of electrons per molecular weight of the medium, I the mean excitation energy of the medium and β the velocity of the proton by the velocity of light which is calculated using the relation [61]:

  $$\beta = \left[1 - \left(\frac{1}{(T/\mathrm{Mc}^2)+1}\right)^2\right]^{(1/2)} \tag{4.2}$$

  where T is the proton kinetic energy and Mc^2 its rest energy.

- Bragg's additivity rule was used for the stopping power of compounds:

  $$(1/\rho)S_{\mathrm{col}} = \sum_k w_k(S_{\mathrm{col}}/\rho)_k \tag{4.3}$$

  where w_k is the fraction by weight and $(S_{\mathrm{col}}/\rho)_k$ is the mass collision stopping power of the k'th atomic constituent. Similarly, the mean excitation energy and the quantity Z/A was computed as follows:

  $$\ln I = \left[\sum_k w_k(Z_k/A_k)\ln I_k\right]\Big/\left\langle Z/A\right\rangle \tag{4.4}$$

  $$\left\langle Z/A\right\rangle = \sum_k w_k(Z_k/A_k) \tag{4.5}$$

  where Z_k and A_k are the atomic number and atomic mass of the k'th atomic constituent, respectively. Mean excitation energies were used according to ICRU Report 37 [60] for the constituting elements of compounds in the condensed phase.

- Equivalent depths were calculated by transposing data onto a common scale from zero to one (representing the discrete step length), where one represents the range of protons at a certain energy in the respective material (r_{w} or r_{pl}). Thus, equivalent depths can be thought as a percentage of the total range in mass thickness units (g.cm^{-2}). The range of a proton was computed from the mass collision stopping power (S_{col}/ρ) as a function of energy E using the CSDA:

  $$R(E_{\mathrm{initial}}) \approx \int_{E_{\mathrm{initial}}}^{E_{\mathrm{final}}} \left(-\frac{1}{\rho} S_{\mathrm{col}}(E) \right)^{-1} \mathrm{d}E \tag{4.6}$$

  in units of g.cm^{-2}. In the CSDA the rate of energy loss at every point along the proton track is assumed to be equal to the mass stopping power and, therefore, energy-loss fluctuations are neglected.

- Along a grid of predefined step lengths, the average energy loss of primary protons, ΔE, per unit length, was calculated from the stopping powers derived in order to obtain the primary proton energy E_{Pprim} at each slab n.

  $$E_{\mathrm{Pprim}} = E_n = E_{n-1} - \Delta E_n \tag{4.7}$$

  $$\Delta E_n = (S_{\mathrm{col}}/\rho)_{m,n-1} . \rho \Delta d_n \tag{4.8}$$

  where $(S_{\mathrm{col}}/\rho)_{m,n-1}$ is the mass collision stopping power of the respective material m (water or plastic) and $\rho \Delta d_n$ is the mass thickness of slab n.

- The attenuation of primary particles over each step was calculated using the total non-elastic nuclear reaction cross sections from ICRU Report 63 [37], providing estimates of the fraction of primary proton fluence in water and plastic phantom material as a function of depth, $\Phi_{\mathrm{w}}^{\mathrm{Pprim}}(z_{\mathrm{w-eq}})$ and $\Phi_{pl}^{\mathrm{Pprim}}(z_{pl})$:

  $$\Phi^{\mathrm{Pprim}} = N_n = N_{n-1} \cdot \mathrm{e}^{-(\mu_n/\rho).\rho \Delta d_n} \tag{4.9}$$

  where Φ^{Pprim} is in cm^{-2} and μ is the macroscopic cross section (also known as attenuation coefficient) in units of cm^{-1}. The latter represents the probability of interaction of a particle per unit of linear path length in the medium. The macroscopic cross section μ is defined as:

  $$\mu = \rho \frac{\mathrm{N_A}}{A} \sigma_{\mathrm{n}} \quad \text{for nuclear interactions} \tag{4.10}$$

where $\mathrm{N_A}$ is the Avogadro's number and σ_n refers to nuclear cross sections. Thus,

$$\mu_n/\rho = \frac{\sigma_{\mathrm{react},n-1}}{A} \cdot \mathrm{N_A} \tag{4.11}$$

$$\sigma_\mathrm{react}/A = \sum_k w_k(\sigma_{k,\mathrm{react}}/A_k) \tag{4.12}$$

where σ_react is the nuclear reaction cross section in a compound and is calculated from the elemental cross sections. It represents the probability that for a given primary proton fluence a proton is removed from the beam by a nuclear interaction.

- The production cross section for a given charged particle type represents the probability that for a given primary proton fluence a charged particle of that type is emitted. The production cross section of a particular particle type i is related to the reaction cross section by $\sigma_{\mathrm{prod},i} = \sigma_\mathrm{react} \cdot \mathrm{mutiplicity}_i$, with $\mathrm{multiplicity}_i$ equal to the number of particles of type i that are on average emitted per nuclear interaction. Thus, the energy per unit mass of charged particles emitted was computed as:

$$D^\mathrm{nuc}_\mathrm{dep} = \Phi^{\mathrm{p_{prim}}} \cdot \mathrm{N_A} \cdot \sum_i \sum_k w_k(\sigma_{\mathrm{prod},i,k}/A_k) \cdot \left\langle W_{\mathrm{rec},i,k} \right\rangle \tag{4.13}$$

where $D^\mathrm{nuc}_\mathrm{dep}$ is in units of $\mathrm{MeV.g^{-1}}$, $\sigma_{\mathrm{prod},i,k}$ is the production cross section of secondary charged particles for the element k and $\left\langle W_{\mathrm{rec},i,k} \right\rangle$ is the average emission energy of the recoil spectrum. In this model the energy of secondary particles is assumed to be deposited locally and secondary particles considered included protons, alphas, deuterons, tritons, ^{3}He and recoils.

- Finally, dose-to-medium was calculated as:

$$D_m(z_m) = \Phi^{\mathrm{p_{prim}}}_m(z_m) \cdot \left(\frac{S_\mathrm{col,p}(E_{\mathrm{p_{prim}}})}{\rho} \right)_m + \Phi^{\mathrm{p_{prim}}}_m(z_m) \cdot N_A \cdot \sum_i \sum_k w_k(\sigma_{\mathrm{prod},i,k}/A_k) \cdot \left\langle W_{\mathrm{rec},i,k} \right\rangle \tag{4.14}$$

where the first term represents the contribution of energy depositions due to the energy loss of primary protons and the second term represents the contribution of energy depositions due to nuclear interactions.

- The fluence correction factor was then computed as:

$$k^\mathrm{AM}_\mathrm{fl} = \frac{D_\mathrm{w}(z_\mathrm{w-eq})}{D_{pl}(z_{pl}) \cdot \left(\frac{S_\mathrm{col,p}(E_{\mathrm{p_{prim}}})}{\rho} \right)_\mathrm{w} \Big/ \left(\frac{S_\mathrm{col,p}(E_{\mathrm{p_{prim}}})}{\rho} \right)_{pl}} \tag{4.15}$$

Stopping powers from ICRU Report 37 [60] and nuclear data from ICRU Report 63 [37] were used.

4.3.2 Validation

The analytical model implemented in MATLAB was compared against Monte Carlo simulations using FLUKA. As described in section 4.3.1, in the analytical model energy losses were assumed to take place through the continuous slowing down approximation. In order to have a pure CSDA calculation in Monte Carlo, multiple Coulomb scattering (MCS), nuclear reactions (NUC) and energy loss fluctuations (FLUC) need to be switched off. The following physics settings were used in FLUKA:

- The DEFAULTS card was set to HADROTHErapy;
- The MCSTHRES card was used to switch off MCS of primary and secondary charged hadrons by setting the energy threshold for these interactions very high;
- The IONFLUCT card was used to switch off FLUC;
- The DELTARAY card was used to switch off the production of delta-rays by setting the production threshold to infinity;
- The THRESHOL card was used to switch off elastic nuclear interactions by setting the energy threshold for these interactions very high;
- The DISCARD card was used to discard neutrons and gammas rays.

Note that non-elastic nuclear interactions were included in the simulations, and secondary charged particles were transported (with the exception of delta-rays).

Figure 4.1 shows a comparison of the fluence correction factor derived using Monte Carlo simulations (solid circles) and the analytical model (straight lines). The fluence correction factor was derived for graphite (left graphs) and PMMA (right graphs) with reference to water for a 60 MeV proton beam (top graphs) and a 200 MeV proton beam (bottom graphs).

Overall, the analytical model gave acceptable predictions. A better agreement between the models was found for the low-energy beam. The analytical model considers that secondary particles deposit their energy at the point of interaction. However, in reality and in the Monte Carlo simulations, these particles travel a certain distance and deposit their energy further way from the point where produced.

At higher energies the dose contribution and range of secondary particles becomes larger, thus, the approximations are further from reality than for a low-energy beam. Furthermore, different nuclear models are used in the analytical model and in the Monte Carlo simulations. The need for k_{fl} factors originates from the differences in the non-elastic nuclear interaction cross sections between water and the different materials. These interactions are described by the PEANUT (Pre-Equilibrium Approach to Nuclear Thermalization) model in FLUKA [62, 63], while the analytical model uses data from the ICRU Report 63 [37]. Palmans *et al.* [24] also reported differences between fluence correction factors calculated using nuclear data from ICRU Report 63 [37] and five different Monte Carlo codes (Geant4, FLUKA, MCNPX, SHIELD-HIT and McPTRAN.MEDIA). Moreover, the dose contribution due to nuclear interactions is larger for higher-energy beams. For example, in a 250 MeV proton beam about 30% of the primary protons are lost in nuclear interactions and about 60% of their kinetic energy emerges as secondary charged particles. Nevertheless, differences between models were below 1%.

The analytical model was used as a tool to quickly test a wide range of compositions since the CPU time required to compute the fluence correction factor was about 2 seconds, while for FLUKA it was 15 hours.

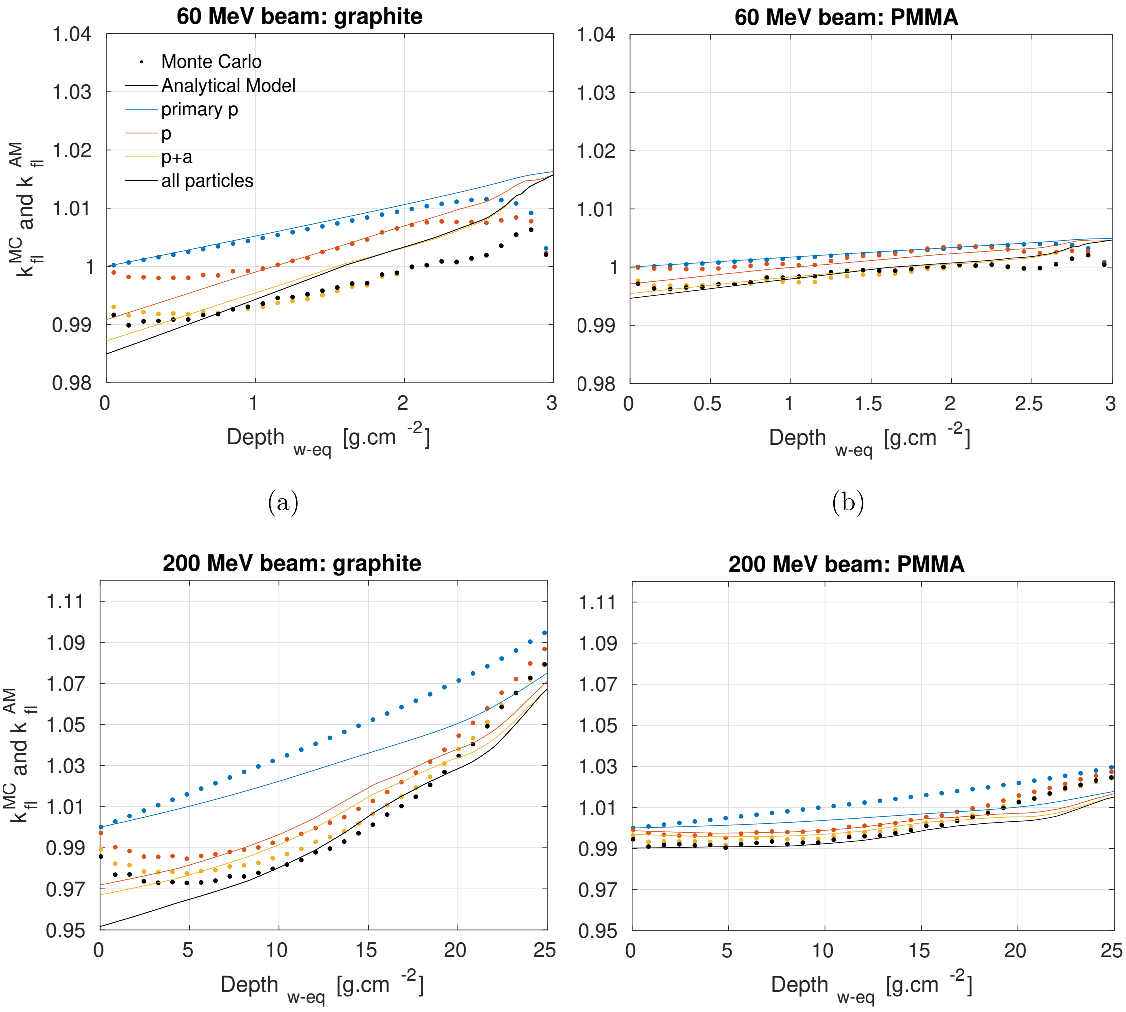

(a) (b)

(c) (d)

Figure 4.1: Comparison of the fluence correction factor derived using Monte Carlo simulations (solid circles) and the analytical model (solid lines) between water and graphite for (a) a 60 MeV proton beam and (c) a 200 MeV proton beam, and between water and PMMA for (b) a 60 MeV proton beam and (d) a 200 MeV proton beam. The models consider the contribution of different secondary particles (primary p = primary protons, p = primary and secondary protons, a = alphas) and all charged particles.

4.3.3 Epoxy resins

In this work new compositions of plastic materials based on epoxy resins were studied for proton beams. Epoxy resins consist of low-molecular-weight compounds containing epoxide groups. Compounds containing a reactive group to the epoxide (a.k.a. hardeners), when mixed together with the epoxy resin, produce a linked polymer that can be mixed with powders of different compositions. The resulting plastic is a rigid material and insoluble in water.

There are various resins and hardeners avaiable with different compositions and the production of plastic materials based on epoxy resins is relatively simple [56–59]. It is also possible to adjust their density by adding gas-filled spheres called phenolic microspheres (PMS). In previous work by White *et al.* [56], different epoxy resin systems designated by CB1, CB2, CB3 and CB4, were evaluated for photon beams. Here, the same epoxy resin systems were evaluated for proton beams.

New plastic materials were formulated by adding powders with varying atomic low-Z numbers to the epoxy resin mixtures in order to change the atomic number of the final compound. The new formulations were then tested using the analytical model. The elements considered were H, C, N, O, Al, Si, P and Ca, since the nuclear cross sections of these elements are present in ICRU Report 63 [37]. PMS of 50 μm diameter were also added to the composition of the resins in a percentage of roughly 4%. Many compositions were tested and four compositions were proposed for more detailed evaluation. Due to intellectual property constraints, more information regarding the criteria of acceptance cannot be provided. Figure 4.2 shows the fluence correction factor derived using the analytical model between water and the four different types of epoxy resins and the four proposed materials, referred to as plastics #1, #2, #3 and #4, for a 200 MeV proton beam. For plastics #3 and #4, the fluence correction factor fluctuated between +/-1% with depth, while for plastics #1 and #2, the fluence correction factor increased from 0.99 towards 1.02 with a total variation of 2.0%-2.5%.

The four proposed plastics were then produced in collaboration with St Bartholomew's Hospital (UK). Three of the plastics were characterized experimentally and using Monte Carlo simulations in order to determine the effect of adding powders to the resins (section 4.5). Plastic #4 did not result in an homogeneous mixture thus it was not considered for experimental evaluation.

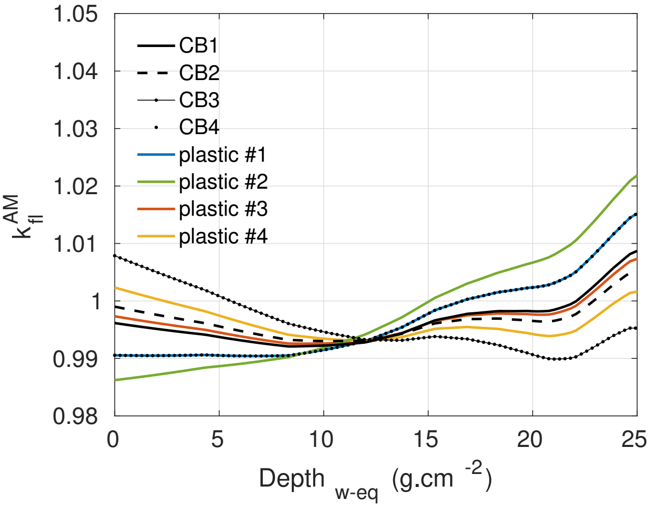

Figure 4.2: Fluence correction factor derived using the analytical model between water and various materials for a 200 MeV proton beam.

4.4 Material physical properties

To have a completely water equivalent material one must understand which physical properties are important. Thus, it is relevant to understand what are the interactions involved when proton beams pass through matter.

Protons lose energy by proton-atomic electron collisions. This type of interaction is very well known and can be described by the Bethe-Bloch theory (equation 4.1) which calculates the mean energy loss of a proton per unit path length in a material (stopping power). In reality, the number of proton-atomic electron collisions per unit path length can fluctuate and the amount of energy loss in each collision will not be the same (energy straggling). For example, secondary electrons ejected with a larger energy compared with the ionization potential (delta-rays) travel further away from the point where generated before their energy is deposited. Spencer-Attix stopping power theory considers the production of these electrons that have enough energy to leave the medium of interest. Nevertheless, proton beams are near mono-energetic along their path and thus well described by Bethe-Bloch theory. The mass stopping power of a proton is medium dependent, and equation 4.1 can be re-written as a function of the medium independent terms to separate them from the medium dependent terms:

$$(1/\rho)S_{\text{col}} = f\left(\frac{k}{\beta^2}\right)\frac{Z}{A} \times [f(\beta) - \ln(I)] \tag{4.16}$$

where k is a constant. Therefore, the mass stopping power of a specific compound is dependent on Z/A and $\ln I$ and by computing these quantities for different plastic materials and by comparing with those for water, it is possible to quantify the water-equivalence of such materials for a given interaction type. The stopping power for compounds can be calculated by averaging the stopping power over each atomic element weighted by the fraction of that element in the compound (Bragg's additivity rule) and effective values of Z/A and $\ln I$ were calculated using equations 4.5 and 4.4, respectively.

Protons are deflected when they pass in the neighbourhood of a nucleus due to the Coulomb and hadronic field of the nucleus. The probability of Coulomb interactions $\mathrm{d}\sigma(\theta)/(\sin\theta\,\mathrm{d}\theta)$ was first represented by the Rutherford scattering formula. Considering a small projectile with mass M_1 in comparison with the mass of the nucleus M_2 with charge z and Z, respectively, the differential atomic cross section is [64]:

$$\frac{\mathrm{d}\sigma(\theta)}{\sin\theta\,\mathrm{d}\theta} = \frac{2\pi \mathrm{e}^4 z^2 Z^2}{16T^2\sin^4(\theta/2)} = f(T^2,\theta)Z^2 \tag{4.17}$$

where T is the kinetic energy of the incident projectile, θ the scattering angles and e the electron charge. The cross section decreases rapidly with increasing angle and energy therefore protons have predominantly very small deflection angles (single scattering). When considering macroscopic cross sections (equation 4.10):

$$\mu_{\sigma_\mathrm{R}} = \rho\frac{\mathrm{N_A}}{A}\cdot f(T^2,\theta)Z^2 \tag{4.18}$$

and for mixtures,

$$\begin{aligned} \mu_{\sigma_\mathrm{R}} &= \rho\mathrm{N_A}\sum_i w_i\frac{\sigma_{\mathrm{R},i}}{A_i} \\ &= \rho\mathrm{N_A}\left(\sum_i w_i\frac{Z_i^2}{A_i}\right)\cdot f(T^2,\theta) \\ &= \rho\left\langle\frac{Z^2}{A}\right\rangle_m \mathrm{N_A}\cdot f(T^2,\theta) \end{aligned} \tag{4.19}$$

Therefore, the Rutherford atomic cross section is proportional to $\rho\left\langle Z^2/A\right\rangle_m$.

Deflections caused by electrons are small since the proton mass is roughly 1800 times larger than the one of electrons. The main angular deflection is due to multiple small deflections and as a result multiple Coulomb scattering theories were derived. Analogous to stopping power, scattering power is defined as the rate of increase of the variance of the multiple Coulomb scattering angle per unit path length [1]:

$$T(x) \equiv \mathrm{d}\left\langle\theta_y^2\right\rangle/\,\mathrm{d}x \tag{4.20}$$

There are different parametrizations for $T(x)$ derived from the differential of Molière formula (most acceptable theory for proton multiple Coulomb scattering). The one from Gottschalk is [1, 65]:

$$T_{\mathrm{dM}}(x) = f_{\mathrm{dM}}(pv, p_1v_1) \times \left(\frac{15.0\mathrm{MeV}}{pv}\right)^2 \frac{1}{X_S} \tag{4.21}$$

where the scattering length X_S is a material property defined as:

$$\frac{1}{\rho X_S} \equiv \alpha \mathrm{N_A} r_\mathrm{e}^2 \frac{\rho Z^2}{A} \left\{2\log(33219(AZ)^{-1/3}) - 1\right\} \tag{4.22}$$

which obeys to the Bragg's additivity rule for compounds.

The clinical energy range in proton therapy is much higher than the Coulomb-barrier therefore protons have a probability to interact with the nucleus other than by elastic and inelastic scattering. Nucleus-nucleus collisions (non-elastic nuclear interactions) can take place and change the nature of the projectile, decreasing the primary proton fluence and producing secondary particles. This can be modelled by equation 4.11:

$$\mu_{\sigma_{\mathrm{react}}} = \rho \frac{N_A}{A} \cdot \sigma_{\mathrm{react}} \tag{4.23}$$

Nuclear reactions are harder to model than stopping power and scattering, however, their relative importance can be estimated from the fluence correction factor calculation for a particular material in comparison to water. Furthermore, for mixtures such interactions will be dependent of $\rho/\bar{A}$, where $\bar{A}$ is the average atomic mass of the medium:

$$\begin{aligned} \mu_{\sigma_{\mathrm{react}}} &= \rho N_A \left(\sum_i w_i \frac{\sigma_{\mathrm{react},i}}{A_i}\right) \\ &= \frac{\rho}{\bar{A}} \mathrm{N_A} \cdot \sigma_{\mathrm{react}} \end{aligned} \tag{4.24}$$

Material physical properties of the trial compositions were calculated and compared to those of water and other commercially available plastics in section 4.5.1.4.

4.5 Experimental and Monte Carlo studies

The three trial plastics produced were characterized experimentally and using Monte Carlo simulations; details of these calculations will be described in this section.

4.5.1 Methods

4.5.1.1 Plastic-to-water conversion factor and fluence correction factor

For absolute dosimetry using a graphite calorimeter, Palmans *et al.* [24] derived a dose conversion formula to obtain dose to water in a water phantom from the measured dose to graphite in a graphite phantom. This formalism was further developed in chapter 2 where it was expanded to a more practical experimental set-up involving measurements in a water phantom, with and without the presence of a graphite absorber in front of the phantom. Here, the formal framework is expanded to derive absorbed dose to water in a water phantom from ionization chamber charge readings performed in a plastic phantom.

The determination of absorbed dose to water for a proton beam, using an ionization chamber, is expressed by [4]:

$$D_{\mathrm{w}}^{(1)}(z_{\mathrm{w}}^{(1)}) = M^{(1)}(z_{\mathrm{w}}^{(1)}) \cdot N_{D_{\mathrm{w},Q}} \tag{4.25}$$

where $D_{\mathrm{w}}^{(1)}$ is the dose to water in a water phantom, $M^{(1)}$ is the ionization chamber reading in a water phantom and $N_{D_{\mathrm{w},Q}}$ is the calibration coefficient in terms of absorbed dose to water for the beam quality Q.

Three different setups are considered in which ionization chamber readings can be defined: a water phantom (setup 1), a plastic phantom (setup 2) and a water phantom with slabs of plastic in front (setup 3), respectively (figure 4.3).

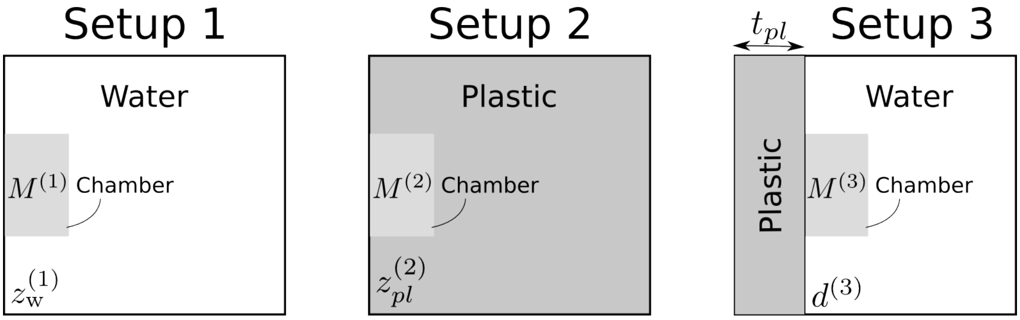

Figure 4.3: Three setups considered in the experiments and simulations. The beam is incident from the left.

As defined in the IAEA TRS-398 Code of Practice [4], the fluence scaling factor, h_{pl}, is calculated by:

$$h_{pl} = \frac{M^{(1)}(z_{\mathrm{w-eq}})}{M^{(2)}(z_{pl}^{(2)})} \tag{4.26}$$

where $M^{(1)}$ is the ionization chamber reading in the water phantom in setup 1 and $M^{(2)}$ is the ionization chamber reading in the plastic phantom in setup 2. The depth in setup 1, $z_{\mathrm{w}}^{(1)}$, is related with depth in setup 2, $z_{pl}^{(2)}$, by the range scaling factor, c_{pl}, in units of g.cm^{-2}. The experimental determination of the range in setup 2, $r^{(2)}$, is very time consuming because for each depth plastic plates need to be added manually in front of the chamber; also its accurate determination is hampered by the resolution of available plates. Thus, a more practical experimental setup was proposed (chapter 2), where measurements are performed in a water phantom with plastic slabs of variable thickness in front of it - setup 3. Ionization chamber readings in setup 3, $M^{(3)}(d^{(3)}, t_{pl})$, are thus a function of the depth in water $d^{(3)}$, and the thickness of the plastic slab t_{pl}. The assumption is made that at the interface between the plastic and the water phantom when $d^{(3)} = 0$ and when $z_{pl}^{(2)} = t_{pl}$, $M^{(2)}(t_{pl}) \approx M^{(3)}(0, t_{pl})$. Note that for practical reasons it is not possible to perform measurements at a depth $d^{(3)} = 0$ (due to the water phantom's entrance wall and the ionization chamber's front wall), therefore, the most proximal depth is considered. Considering the assumption described, equation 4.26 can be rewritten as:

$$h_{pl} = \frac{M^{(1)}(z_{\mathrm{w-eq}})}{M^{(2)}(z_{pl}^{(2)})} \approx \frac{M^{(1)}(z_{\mathrm{w}}^{(1)})}{M^{(3)}(0, t_{pl})} \tag{4.27}$$

By solving equation 4.27 for $M^{(1)}$ and inserting the resulting $M^{(1)}$ expression into equation 4.25, the determination of absorbed dose to water in a plastic can be expressed as:

$$D_{\mathrm{w}}^{(1)}(z_{\mathrm{w}}^{(1)}) \approx M^{(2)}(t_{pl}) \cdot \frac{M^{(1)}(z_{\mathrm{w}}^{(1)})}{M^{(3)}(0, t_{pl})} \cdot N_{D_{\mathrm{w},Q}} \approx M^{(2)}(t_{pl}) \cdot H_{pl,\mathrm{w}}^{\mathrm{exp}} \cdot N_{D_{\mathrm{w},Q}} \tag{4.28}$$

where the ratio $M^{(1)}(z_{\mathrm{w}}^{(1)})/M^{(3)}(0, t_{pl})$ is the plastic-to-water conversion factor and $H_{pl,\mathrm{w}} \approx h_{pl}$.

The $H_{pl,\mathrm{w}}$ term is not an overall conversion factor from dose to plastic in a plastic phantom (setup 2) to dose to water in a water phantom (setup 1) [24]. Instead, $H_{pl,\mathrm{w}}$ relates ionization chamber readings in a plastic phantom (setup 2) with dose to water in a water phantom (setup 1). It can also be interpreted theoretically as relating dose to water in the plastic phantom to dose to water in the water phantom. If $H_{pl,\mathrm{w}} = 1$, no conversion needs to be applied to equation 4.28 and the plastic material is water-equivalent.

The experimental plastic-to-water conversion factor, $H_{pl,\mathrm{w}}^{\mathrm{exp}}$, is thus determined by the ratio of ionization chamber readings in setup 1 and setup 3:

$$H_{pl,\mathrm{w}}^{\mathrm{exp}} = \frac{M^{(1)}(z_{\mathrm{w}}^{(1)})}{M^{(3)}(d^{(3)}, t_{pl})} \tag{4.29}$$

Depth in setup 1 is related with depth in setup 3 by the range difference, i.e., the water-equivalent thickness, WET, of the plastic slab t_{pl}: $z_{\mathrm{w}}^{(1)} = d^{(3)} + t_{pl,\mathrm{w-eq}}$. Furthermore, for one particular slab thickness t_{pl}, an $H_{pl,\mathrm{w}}$ factor is calculated at N depths $d^{(3)}$ and a mean value can be derived:

$$H_{pl,\mathrm{w}}^{\mathrm{exp}} \approx \frac{1}{N} \sum_{j=1}^{N} \frac{M^{(1)}(z_{\mathrm{w},j}^{(1)})}{M^{(3)}(d_j^{(3)}, t_{pl})} \tag{4.30}$$

Points near the Bragg peak are not considered since positioning uncertainties become critical in this region. If equations 4.29 and 4.30 give the same result then there is no depth dependence on the calculation of $H_{pl,\mathrm{w}}$ for a particular slab with thickness t_{pl}. By testing different slab thicknesses for a given material, a variation of $H_{pl,\mathrm{w}}$ values with depth is determined. Assuming that ionization in the chamber is proportional to dose, $H_{pl,\mathrm{w}}$ can also be calculated using Monte Carlo methods by (see section 2.3.1):

$$H_{pl,\mathrm{w}}^{\mathrm{MC}} = \frac{D_{\mathrm{w}}^{(1)}(z_{\mathrm{w}}^{(1)})}{D_{\mathrm{w}}^{(3)}(d^{(3)}, t_{pl})} \tag{4.31}$$

And using similar arguments to those related to equation 4.30:

$$H_{pl,\mathrm{w}}^{\mathrm{MC}} \approx \frac{1}{N} \sum_{j=1}^{N} \frac{D_{\mathrm{w}}^{(1)}(z_{\mathrm{w},j}^{(1)})}{D_{\mathrm{w}}^{(3)}(d_j^{(3)}, t_{pl})} \tag{4.32}$$

The water-equivalence of plastic materials can also be quantified by calculating the fluence correction factor, k_{fl}. While $H_{pl,\mathrm{w}}$ values need to be calculated to convert ionization chamber readings in a plastic phantom to dose to water in a water phantom, k_{fl} factors are necessary for the conversion of dose to plastic in a plastic phantom to dose to water in a water phantom. Therefore, the water-equivalence of the plastics was also studied by computing k_{fl} factors between water and plastic using equation 2.4.

4.5.1.2 Experimental determination of $H_{pl,\mathrm{w}}^{\mathrm{exp}}$

Three plastic materials, referred as plastics #1, #2 and #3, were specifically formulated for light-ion beam dosimetry and characterized experimentally with reference to water in proton beams. The plastics tested were based on the same epoxy resin mixed with different low-Z compounds and were produced in collaboration with St Bartholomew's Hospital, UK [56–59]. Experimental information of $H_{pl,\mathrm{w}}^{\mathrm{exp}}$ was obtained from laterally integrated depth-dose ionization chamber measurements in a water phantom using setups 1 and 3. Measurements were carried out at the 60 MeV proton cyclotron at the Clatterbridge Cancer Centre (CCC), UK, and at the 226 MeV proton cyclotron at the Trento Proton Therapy Center (TPTC), Italy (figure 4.4).

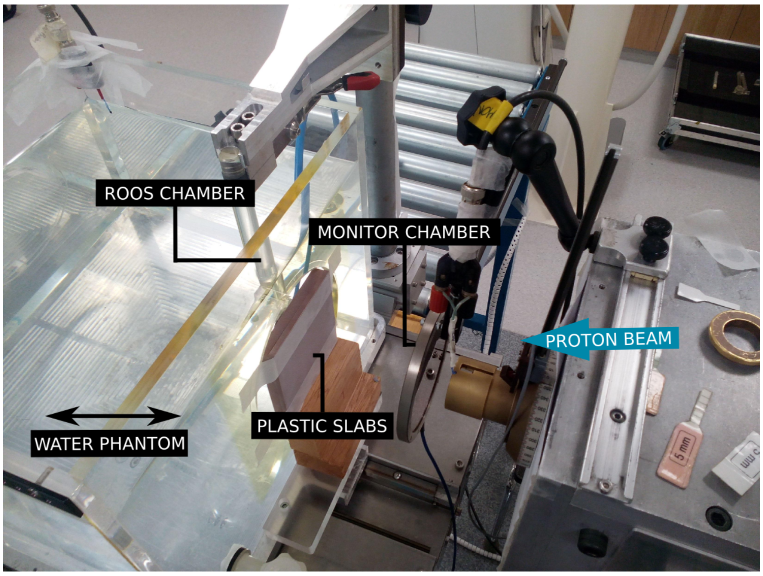

(a)

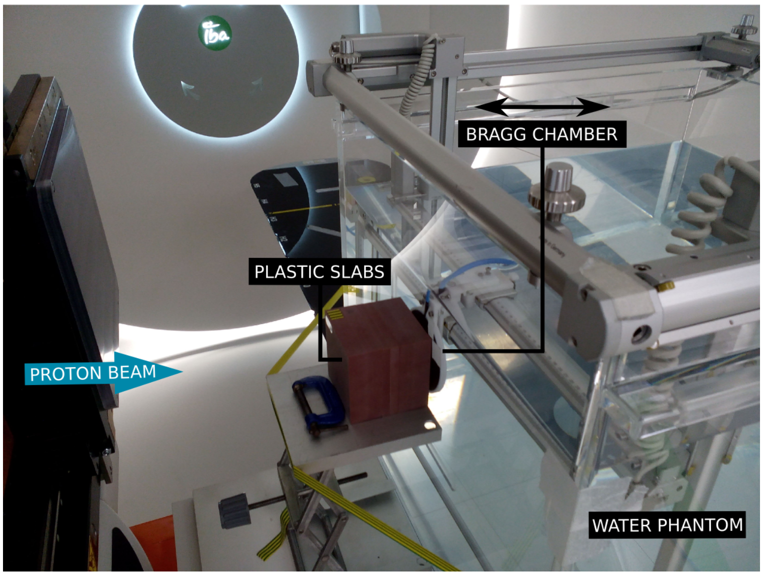

(b)

Figure 4.4: Experimental setups: (a) at CCC with SDD constant and (b) at TPTC with SSD constant.

The CCC beam line consisted of a double scattering system and collimators [35] providing an un-modulated 60 MeV beam with a diameter of 4 mm at collimator exit. Monitoring of the beam was performed with a PTW type 7862 transmission chamber placed in front of the collimator. Measurements were performed in a water phantom with a WET front wall of 3.7 mm, using a Roos plane-parallel ionization chamber (PTW type 34001), placed about 15 cm away from the collimator. The water phantom was moved towards the beam to vary the amount of water upstream of the chamber. This was repeated with different thicknesses of plastic slabs in front of the water phantom.

At TPTC, the beam line consisted of a scanning system and measurements were performed using a single spot. Similarly as at CCC, an un-modulated beam was used with a nominal energy of 226 MeV. Measurements were carried out in a water phantom with a front wall of 17.4 mm WET, using a large-area plane-parallel ionization chamber (PTW type 34070 “Bragg Peak”), and the beam monitor signal for normalization. The water phantom was at a fixed position with its front face aligned with the isocentre and the chamber depth was varied. Measurements were repeated with plastic slabs in front of the water phantom.

Note that measurements at TPTC were carried out using a constant source-to-phantom surface distance (SSD), while at CCC measurements were performed using a constant source-to-detector distance (SDD). The SDD setup avoids corrections for particles scattered by the collimator edges; such corrections are not negligible for the CCC beam when a collimator of 4 mm is used [35]. For the TPTC beam the scattering of particles at the nozzle exit is assumed to be negligible since it consists of a scanning system.

4.5.1.3 Numerical simulations of $H_{pl,\mathrm{w}}^{\mathrm{MC}}$ and $k_{\mathrm{fl}}^{\mathrm{MC}}$

The $H_{pl,\mathrm{w}}^{\mathrm{MC}}$ factor was calculated by Monte Carlo simulations using equations 4.29 and 4.30 and the fluence correction factor, $k_{\mathrm{fl}}^{\mathrm{MC}}$, was also calculated using equation 2.4. Commonly used water-equivalent plastics were also simulated by Monte Carlo. Materials were defined according to IAEA TRS-398 Code of Practice [4] and ICRU Reports 37 [60] and 49 [27] and included A-150 tissue equivalent plastic, PMMA, polyethylene, polystyrene, Rando® soft tissue (The Phantom Laboratory, Salem, NY, USA), Gammex 457-CTG (CTG Solid Water®: GAMMEX, Middleton, WI, USA) and WT1 (St Bartholomew’s Hospital, London, UK). The density of the trial plastics was determined through weight and volume measurements of each slab.

For the CCC beam, simulations were performed with the FLUKA-2011.2c.4 code [16, 17]. The geometry of the CCC beam line was implemented as described in Bonnett *et al.* [33], Baker *et al.* [34], and Kacperek [35]. The default HADROTHErapy card was used with a delta-ray production threshold set to infinity. Secondary electrons have short ranges so it was assumed their energy was absorbed locally. Inelastic hadron-nucleus interactions were described by the PEANUT (Pre-Equilibrium Approach to Nuclear Thermalization) model [62, 63]. The incident particles in the first scattering foil were 62.5 MeV protons assuming a Gaussian spread of $\sigma = 0.28\,\text{MeV}$ (section 2.5.2). Dose and charged particle fluence differential in energy were scored in bins of 0.01 cm and 0.1 cm, respectively, throughout cylindrical phantoms of a given material. A total number of $5\text{x}10^8$ primary protons were simulated for each material. Scoring was performed within the radius of the Roos ionization chamber (7.5 mm) and in a larger radius of 10 cm to study the contribution of particles that scatter outside the sensitive area of the chamber. Particles scored included primary and secondary protons, alpha particles, deuterons, tritons and ^{3}He ions. In order to implement a constant SDD setup in Monte Carlo, a simulation would be required for each position of the phantom. Therefore, a constant SSD setup was implemented and a correction was applied to obtain SDD calculations (section 2.4.2).

Simulations for the TPTC beam were performed using two Monte Carlo codes, FLUKA-2011.2c.4 [16, 17] and Geant4-9.6.p01 [66], because corrections are expected to be higher in high-energy beams. A beam of 226.14 MeV was simulated with a Gaussian energy spread of $\sigma = 0.67\,\text{MeV}$ and divergence of 1.3 mrad [67]. Dose and fluence were scored within the radius of the Bragg peak ionization chamber (40.8 mm) used in the experiments, as well as, within a radius of 10 cm. FLUKA simulations were implemented with similar parameters as those used for the CCC beam. For the Geant4 simulations, the reference physics list QGSP_BIC_EMY was used [68]. Electromagnetic interactions were described by the electromagnetic standard package option 3 (emstandard_opt3), and hadronic nucleon-nucleus interactions were described by the BIC (Binary cascade) model [69]. Production thresholds for photons, electrons and positrons were set to 10 km (i.e. secondary production of these particles were not considered in the simulations). Dose and charged particle fluence differential in energy were scored in 0.07 cm slabs in water and scaled slab thicknesses in each plastic material in cylindrical phantoms. For each setup about $4.4\text{x}10^6$ primary protons were simulated.

4.5.1.4 Material physical properties

As described in section 4.4, the mass stopping power of a specific compound depends on the number of electrons per molecular weight of medium, Z/A. Thus, by computing this quantity for different plastic materials and by comparing with those for water, it is possible to quantify the water-equivalence of such materials for a given interaction type. Therefore, Z/A was calculated for all the materials using the Bragg additivity rule for compounds [60], as well as, the scattering length, X_S, which is related to the mass scattering power [65]. The scattering length scales the scattering power for different materials and can be interpreted as the distance a 15 MeV proton would have to travel in the medium for the scattering angle to increase by 1 rad [65]. In addition, the relative water-equivalent thickness (rWET) was calculated experimentally and using Monte Carlo methods for the novel plastics using the following relation:

$$\mathrm{rWET} = \frac{t_{pl,\mathrm{w-eq}}}{t_{pl}} \tag{4.33}$$

where $t_{pl,\mathrm{w-eq}}$ and t_{pl} are expressed in cm. rWET values were also derived from Monte Carlo simulations for seven commercially available plastics. Note that C_{pl} factors with uppercase are expressed in cm according to IAEA TRS-381 Code of Practice [70], while c_{pl} factors with lowercase are expressed in g.cm^{-2} according to IAEA TRS-398 Code of Practice [4]. For a material to be water-equivalent in terms of range, the linear stopping power plays an important role thus rWET and C_{pl} values are relevant. On the other hand, for applications where the materials can be scaled by the density, the mass stopping power is important and c_{pl} is the quantity of interest.

Table 4.1 lists different material properties computed for various plastics. In comparison to water, Z/A differs 1%-2% for A-150, plastic #3 and Rando soft tissue, whereas for plastic #2 differences were of the order of 4%. In terms of ρX_S values, plastic #2 was the most water-equivalent material. rWET values were calculated using Monte Carlo methods for ten different thicknesses of each material tested in the TPTC beam and a mean value was derived. FLUKA and Geant4 rWET values agreed within 0.1%, while for the trial plastics characterized experimentally average differences between experimental and Monte Carlo data were about 2%. This discrepancy may be due to uncertainties in the weight and volume measurements of the plastics that influence directly the density and therefore the range. Range scaling factors were also computed for comparison. Note that rWET values relate depths between setups 1 and 3, while C_{pl} and c_{pl} factors relate depths between setups 1 and 2. A good agreement between rWET and C_{pl} factors was found for all the materials. In comparison with water, C_{pl} factors were different by less than 0.5% for WT1 and polyethylene, whereas for A-150 and PMMA differences exceeded 13%-16%. These values suggest that A-150 and PMMA materials would not be suitable for an anthropomorphic phantom. C_{pl} factors listed in table 1 are in good agreement with those from ICRU Report 49 [27], where for a proton beam of 225 MeV, C_{pl} factors amounted to 1.1345, 1.1583, 0.9982 and 1.0382 for A-150, PMMA, polyethylene and polystyrene, respectively.

Other properties, such as $\ln I$, $\rho(Z^2/A)$ and $\rho(1/\bar{A})$, related to stopping power, scattering and nuclear interactions (section 4.4), were computed as a ratio to water properties in table 4.2. In terms of $\ln I$, phantom materials differ to water in 1.0% for plastics #2 and PMMA and 6.0% for polyethylene. For $\rho(Z^2/A)$ and $\rho(1/\bar{A})$ properties, the differences between water and the plastic materials values are in the range of 1%-30%. These properties are density dependent and the density of the trial plastics can be adjusted by adding gas-filled microspheres thus such values could be water-matched if relevant.

Table 4.1: Material physical properties.

	Z/A (mol.g^{-1})	ρX_s (g.cm^{-2})	rWET^a	C_{pl} ^{a}	c_{pl} ^{a}	Density (g.cm^{-3})
Liquid water	0.5551	46.9	1.0000	1.0000	1.0000	1.00
Plastic #1	0.5385	55.2	0.9352	0.9355	0.9402	0.94
Plastic #2	0.5307	46.7	1.0554	1.0531	0.9534	1.05
Plastic #3	0.5449	56.4	1.0259	1.0278	0.9964	1.03
A-150	0.5490	56.2	1.1332	1.1348	1.0069	1.13
PMMA	0.5393	53.8	1.1635	1.1645	0.9786	1.19
Polyethylene	0.5703	61.8	0.9958	0.9975	1.0612	0.94
Polystyrene	0.5377	59.1	1.0368	1.0376	0.9789	1.06
Rando	0.5446	55.2	0.9907	0.9915	0.9945	1.00
Gammex	0.5395	53.0	1.0217	1.0227	0.9806	1.04
WT1	0.5395	53.0	0.9992	1.0002	0.9806	1.02

[a] Values derived from FLUKA Monte Carlo code.

Table 4.2: Material physical properties as a ratio to water properties.

	$\ln I$ (eV)	$\rho\frac{Z^2}{A}$ (mol.cm^{-3})	$\rho\frac{1}{\bar{A}}$ (mol.cm^{-3})
Liquid water	1.00	1.00	1.00
Plastic #1	0.98	0.80	0.86
Plastic #2	1.01	1.12	0.86
Plastic #3	0.97	0.84	1.01
A-150	0.97	0.93	1.17
PMMA	0.99	1.03	1.07
Polyethylene	0.94	0.70	1.21
Polystyrene	0.98	0.82	0.98
Rando	0.97	0.84	0.97
Gammex	0.98	0.91	0.95
WT1	0.98	0.89	0.93

4.5.2 Results and discussion

4.5.2.1 Low-energy beam

Results from $H_{pl,\mathrm{w}}$ and k_{fl} factors are presented as corrections in percentage away from unity i.e. $H_{pl,\mathrm{w}} - 1$ and $k_{\mathrm{fl}} - 1$.

In figure 4.5, a comparison between experimental data and Monte Carlo simulations of $H_{pl,\mathrm{w}}$ factors are presented for the three novel plastics. Experimental relative standard uncertainties were obtained by combining type A and type B uncertainties in quadrature and are summarized in table 4.3. Type A uncertainties included repeatability of the chamber/monitor ratio and type B included uncertainties in temperature, pressure and standard deviation of the mean of $H^{\mathrm{exp}}_{pl,\mathrm{w}}$ obtained from equation 4.30. At CCC the plastics were tested in the following chronological order, plastic #3, plastic #1 and plastic #2. As can be seen from table 4.3, uncertainties decreased significantly with time (from 1.03% to 0.46%) because the beam alignment became more stable. Monte Carlo type-A uncertainties were of the order of 0.2%. Type B Monte Carlo uncertainties are discussed in section 4.5.2.2. For a particular slab thickness t_{pl}, a mean value was used to represent the $H_{pl,\mathrm{w}}$ factor by application of equations 4.30 and 4.32 since there was no obvious trend of variation of $H_{pl,\mathrm{w}}$ with depth $d^{(3)}$ (refer to figure 4.3).

Overall, corrections were smaller than 0.5% and experimental and Monte Carlo results agreed within uncertainties. These results are in agreement with previous work performed by Palmans *et al.* [10], where h_{pl} values were measured for PMMA with reference to water in an un-modulated and modulated 75 MeV proton beam. Al-Sulaiti *et al.* [14] also measured h_{pl} values for the water-equivalent plastic PWDT in a 60 MeV proton beam. Maximum corrections were smaller than 1% at a depth near the Bragg peak. In general, the results from $H_{pl,\mathrm{w}}$ and h_{pl} factors indicate no preference regarding the plastic to be used since corrections are small for low-energy beams. These results also confirm the recommendation in IAEA TRS-398 Code of Practice [4] for low-energy proton beams where the use of plastic phantoms is permitted for the measurement of dose.

Fluence correction factors between water and the trial plastics were calculated using Monte Carlo methods and the results are shown in figure 4.6, when the fluence of all charged particles is considered. At the surface, fluence corrections are higher in the plastics than in water since $k^{\mathrm{MC}}_{\mathrm{fl}}$ are about 0.5% less than unity. Palmans *et al.* [24] reported a similar effect when computing fluence corrections between

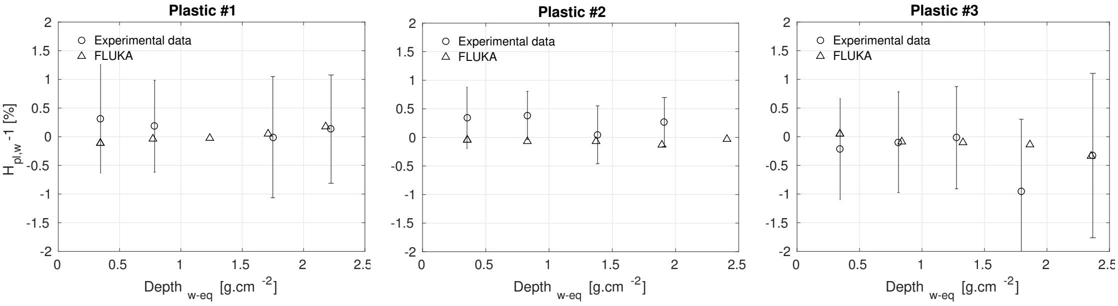

(a) (b) (c)

Figure 4.5: Plastic-to-water conversion factor measured experimentally (refer to equation 4.30) and derived from Monte Carlo simulations (refer to equation 4.32) for (a) plastic #1, (b) plastic #2 and (c) plastic #3 in the CCC beam, inside the area of the Roos chamber used in the experiments. Open circles represent $H^{\mathrm{exp}}_{pl,\mathrm{w}}$ measured experimentally and open triangles represent $H^{\mathrm{MC}}_{pl,\mathrm{w}}$ calculated using FLUKA. Similar results were found for $H_{pl,\mathrm{w}}$ factors calculated in a larger area. Numerical error bars are smaller than the marker points.

water and graphite (see also chapter 2). This effect was mainly attributed to the contribution of alpha particles due to their very short range. The production cross sections of these particles per unit of atomic mass are larger for graphite than for water [37], consequently, the fluence of these particles is larger in compounds with carbon content, such as plastic materials. Fluence corrections did not exceed 1% in absolute magnitude for the three plastics. Monte Carlo calculations of fluence corrections for various plastics were also performed by Palmans *et al.* [10] using an adapted version of the PTRAN code, by Al-Sulaiti *et al.* [13, 14] using MCNPX and FLUKA and by Lühr *et al.* [15] using SHIELD-HIT10A. All these studies reported corrections below 1% between water and plastic materials in low-energy proton beams.

Table 4.3: Experimental relative standard uncertainties of the $H_{pl,\mathrm{w}}^{\mathrm{exp}}$ factor for the measurements performed at CCC.

	Plastic #1		**Plastic #2**		**Plastic #3**	
Component of uncertainty	Type A	Type B	Type A	Type B	Type A	Type B
Chamber/Monitor ratio	0.765	-	0.361	-	0.820	-
Temperature	-	0.050	-	0.050	-	0.050
Pressure	-	0.050	-	0.050	-	0.050
$s_{\overline{H_{pl,\mathrm{w}}^{\mathrm{exp}}}}$	-	0.514	-	0.290	-	0.616
Total	**0.77**	**0.52**	**0.36**	**0.30**	**0.82**	**0.62**
Combined (%)	**0.92**		**0.46**		**1.03**	

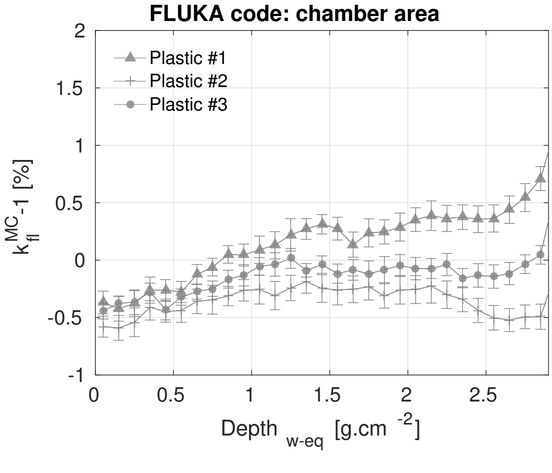

Figure 4.6: Variation with depth of the fluence correction factor for the three novel plastics with reference to water. Fluence corrections were calculated using Monte Carlo simulations (refer to equation 2.4), considering the spectra of all charged particles, inside the area of the Roos chamber used in the experiments.

4.5.2.2 High-energy beam

Figure 4.7 shows $H_{pl,\mathrm{w}}$ factors derived experimentally and calculated using the FLUKA and Geant4 codes for the three novel plastics in the TPTC beam. Open markers represent mean values of $H_{pl,\mathrm{w}}$ factors (calculated from equations 4.30 and 4.32) and solid markers represent $H_{pl,\mathrm{w}}$ factors calculated at a specific depth, proximal to $d^{(3)} = 0$ (equations 4.29 and 4.31). For the thinner plastic slabs t_{pl}, the data showed no depth dependence on the calculation of $H_{pl,\mathrm{w}}$ with $d^{(3)}$, while for thicker slabs the spread of values was slightly larger. In the following graphs only mean values of $H_{pl,\mathrm{w}}$ will be presented and discussed, since its calculation avoids systematic errors. Similar as in CCC, experimental uncertainties included repeatability of the chamber/monitor ratio, uncertainties in temperature, pressure and standard deviation of the mean of the $H_{pl,\mathrm{w}}^{\mathrm{exp}}$ factor (table 4.4). Repeatability was derived from depth-dose measurements only in water that were carried out during the experiments. Uncertainties of 0.5% were found for all the materials.

As can be seen from figure 4.7, experimental data showed no preference regarding the most water-equivalent plastic, with $H_{pl,\mathrm{w}}^{\mathrm{exp}}$ factors up to 1% from unity. For thicker slabs, FLUKA predicts $H_{pl,\mathrm{w}}$ factors of about 1% higher than the ones predicted by Geant4. The need for $H_{pl,\mathrm{w}}$ and k_{fl} factors originates from the differences in the non-elastic nuclear interaction cross sections between water and the different plastic materials. These interactions are described by the PEANUT model in FLUKA [62, 63], and by the BIC model [69] in Geant4. Böhlen *et al.* [32] and Robert *et al.* [71] compared FLUKA and Geant4 nuclear models for carbon-ion beams and for proton and carbon-ion beams, respectively, and both studies reported substantial deviations between codes. Moreover, ICRU Report 63 [37] estimated uncertainties of the order of 5%-10% on the total non-elastic cross sections and 20%-30% on the angle-integrated production cross sections for secondary particles. Type-B Monte Carlo uncertainties include uncertainties in nuclear cross sections, material data and stopping powers. It was assumed that type-B Monte Carlo uncertainties on the calculation of $H_{pl,\mathrm{w}}^{\mathrm{MC}}$ factors were unlikely to be the double that of the average differences between the codes, leading to an estimate of error of 0.54%. Thus, given these uncertainties, Monte Carlo codes do not allow a further discrimination to be made between the three plastics. Nevertheless, as can been seen from figure 4.7, maximum plastic-to-water corrections are about 1%.

In figure 4.8, the water-equivalence of the three plastics tested experimentally is compared with commercially available materials using Monte Carlo simulations. $H_{pl,\mathrm{w}}^{\mathrm{MC}}$ factors were derived inside the area of the Bragg peak chamber using the

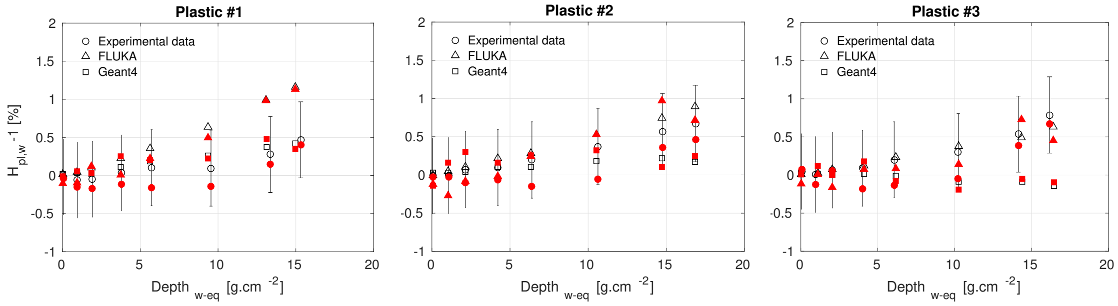

(a) (b) (c)

Figure 4.7: Plastic-to-water conversion factor measured experimentally and derived from Monte Carlo simulations for (a) plastic #1, (b) plastic #2 and (c) plastic #3 in the TPTC beam. Open markers represent mean values of $H_{pl,\mathrm{w}}$ (refer to equations 4.30 and 4.32), and solid markers represent $H_{pl,\mathrm{w}}$ factors calculated at a proximal depth of $d^{(3)} = 0$ (refer to equations 4.29 and 4.31). Circles represent $H^{\mathrm{exp}}_{pl,\mathrm{w}}$ measured experimentally, triangles and squares represent $H^{\mathrm{MC}}_{pl,\mathrm{w}}$ calculated using the FLUKA and Geant4 codes, respectively. Numerical error bars are smaller than the marker points.

FLUKA and Geant4 codes.

For the FLUKA results in figure 4.8(a), plastic #1 gave the largest correction with reference to water, with an $H^{\mathrm{MC}}_{pl,\mathrm{w}} - 1$ correction increasing from 0% to 2% at a depth near the Bragg peak. For polystyrene, the $H^{\mathrm{MC}}_{pl,\mathrm{w}} - 1$ correction increased towards 1.7%, while for polyethylene and PMMA maximum corrections did not exceed 0.5%. The material compositions are C_8H_8 for polystyrene, C_2H_4 for polyethylene and $C_5H_8O_2$ for PMMA. Thus, carbon, oxygen and hydrogen content influence the rate of variation of the $H^{\mathrm{MC}}_{pl,\mathrm{w}}$ factor. This is also applied to the other plastics since these elements make up the majority of their compositions. Table 4.5 summarizes the hydrogen, oxygen and carbon content of the different materials. Polyethylene is the material with highest hydrogen density, followed by A-150 and PMMA, and smaller corrections were found for these materials. For materials with approximately the same hydrogen and oxygen densities, such as, WT1, Gammex 457-CTG, plastic #2 and Rando soft tissue, $H^{\mathrm{MC}}_{pl,\mathrm{w}} - 1$ corrections increased from 0% toward 1.3%-1.5%. Plastic #3, which has similar hydrogen content to PMMA, was the most water-equivalent material of the three trial materials tested experimentally. Although on average the plastics in evaluation are composed of 9% hydrogen and 72% carbon (calculated based on the elemental composition by fraction by weight), hydrogen appears to have a larger influence in the calculation of $H^{\mathrm{MC}}_{pl,\mathrm{w}}$ factors. Previous work from Rasouli *et al.* [72] reported the issue of quantifying the probability of non-elastic nuclear interactions in compounds with hydrogen content. According to

Table 4.4: Experimental relative standard uncertainties for the $H^{\mathrm{exp}}_{pl,\mathrm{w}}$ factor for the measurements performed at TPTC.

	Plastic #1		**Plastic #2**		**Plastic #3**	
Component of uncertainty	Type A	Type B	Type A	Type B	Type A	Type B
Chamber/Monitor ratio	0.493	-	0.493	-	0.493	-
Temperature	-	0.050	-	0.050	-	0.050
Pressure	-	0.050	-	0.050	-	0.050
$s_{\overline{H^{\mathrm{exp}}_{pl,\mathrm{w}}}}$	-	0.020	-	0.030	-	0.026
Total	**0.49**	**0.07**	**0.49**	**0.08**	**0.49**	**0.08**
Combined (%)	**0.50**		**0.50**		**0.50**	

Janni [73], the probability of a proton undergoing a non-elastic nuclear interaction with hydrogen is zero for the clinical energy range. However, natural hydrogen has a large contribution to the stopping power due to its high Z/A ratio, thus, the total non-elastic nuclear interaction cross section per unit of range is reduced for a compound containing hydrogen.

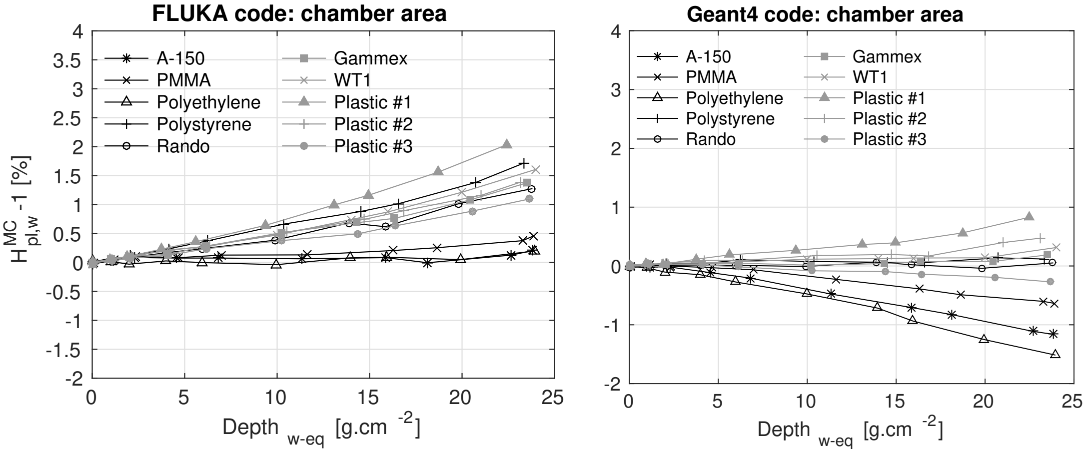

(a)

(b)

Figure 4.8: Plastic-to-water conversion factor for various plastics in the TPTC beam, derived from Monte Carlo simulations (refer to equation 4.32) using (a) FLUKA and (b) Geant4 simulations, inside the area of the Bragg peak chamber.

As with the results presented in figure 4.7 for the three trial plastics, different corrections were found between Geant4 and FLUKA for the materials commercially available. As shown in figure 4.8(b), the largest correction was found for A-150 and polyethylene, where corrections increased from 0% toward 1%-1.5% in absolute magnitude. All other materials gave corrections within +/-1% in magnitude. Although there are differences in the magnitude of $H^{\mathrm{MC}}_{pl,\mathrm{w}}$ factors between the two codes, correc-

Table 4.5: Hydrogen, oxygen and carbon densities for different materials.

	H density ($10^{22}\,\mathrm{cm}^{-3}$)	O density ($10^{22}\,\mathrm{cm}^{-3}$)	C density ($10^{22}\,\mathrm{cm}^{-3}$)
Liquid water	6.7	3.3	0.0
Plastic #1	4.5	0.7	3.3
Plastic #2	4.2	1.1	3.2
Plastic #3	5.7	0.6	3.7
A-150	6.8	0.2	4.4
PMMA	5.7	1.4	3.6
Polyethylene	8.1	0.0	4.0
Polystyrene	4.9	0.0	4.9
Rando	5.5	0.8	3.4
Gammex	5.0	0.8	0.4
WT1	4.9	0.8	3.4

tions were within 2% from unity for all the materials in this study. Considering the results from the two codes, PMMA and plastic #3 were the materials with smallest corrections, where maximum values were about 1%.

Moyers *et al.* [74] measured the ratio of ionization chamber readings in water and polystyrene in un-modulated proton beams. For a beam of 200 MeV, corrections were about 0.2% in the plateau region, whereas at the peak, corrections of the order of 2.3% were found. This is a better agreement with the results from FLUKA than in Geant4, where maximum corrections at a depth near the Bragg peak were about 1.7% and 0.1%, respectively.

By using the least-squares method, $H^{\mathrm{MC}}_{pl,\mathrm{w}}$ factors can be approximated by a linear fit as a function of the H, C, O, N, Ca and F content (fraction by weight), considering FLUKA and Geant4 data:

$$H^{\mathrm{MC}}_{pl,\mathrm{w}} \approx \sum_k a_k \cdot w_k + (b_k \cdot w_k) \cdot z_{\mathrm{w-eq}} \tag{4.34}$$

where k is the element, w_k is the elemental fraction by weight and a_k and b_k are coefficients as listed in table 4.6:

As shown in figure 4.9, the $H^{\mathrm{MC}}_{pl,\mathrm{w}}$ factors derived using equation 4.34 and the coefficients listed in table 4.6 are a good approximation of the data of figure 4.8. Although there are differences in the magnitude of $H^{\mathrm{MC}}_{pl,\mathrm{w}}$ factors between the two codes, the relative behaviour of most plastics is similar. However, the parameterisation of $H^{\mathrm{MC}}_{pl,\mathrm{w}}$ factors as a function of the elemental content did not clarify the source of differences between the codes.

Table 4.6: Fit coefficients for equation 4.34 using FLUKA and Geant4 data.

	FLUKA		**Geant4**	
k	a_k	b_k	a_k	b_k
H	1.00695	-0.00866	1.00907	0.00980
C	0.99873	0.00149	0.99938	0.00087
O	1.00145	-0.00010	1.00145	-0.00004
N	1.03908	0.01412	1.03917	0.01321
Ca	0.99625	-0.00042	0.99412	-0.00006
F	0.95212	-0.04135	0.99412	-0.03719

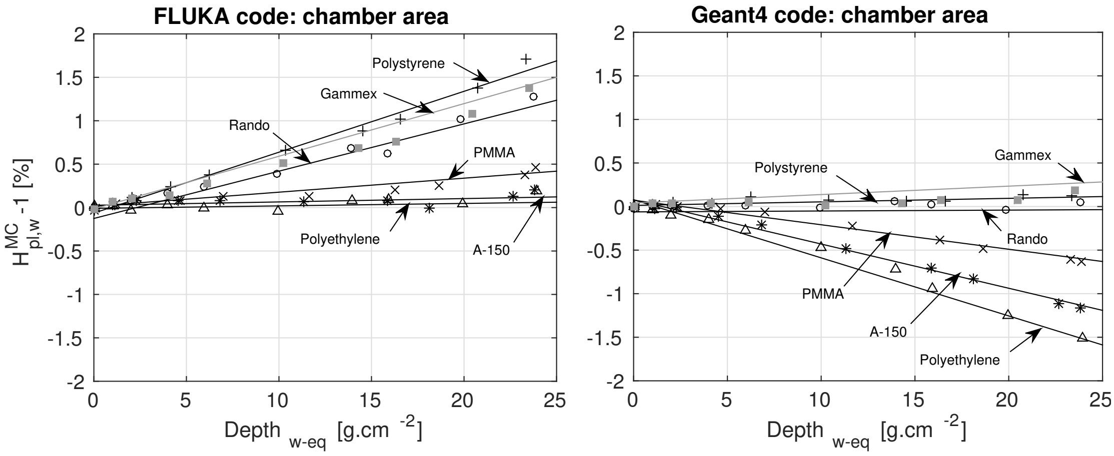

(a)

(b)

Figure 4.9: Linear fits of the plastic-to-water conversion factor derived (a) from equation 4.34 for FLUKA and (b) for Geant4 for polystyrene (pluses), Gammex 457-CTG (solid squares), Rando soft tissue (open circles), PMMA (crosses), A-150 (asterisks) and polyethylene (open triangles).

Figure 4.10 shows the ratio between the energy deposited due to secondary protons inside the radius of the chamber and in a larger radius for water and various materials using FLUKA. Secondary particles originating from non-elastic nuclear interactions emerge with larger angles; therefore a fraction of the energy deposited by these particles is not accounted for within the collecting area of the chamber. Results from figure 4.10 also illustrate the relative differences in scattering between water and the various plastics. Most plastics in this study showed similar scattering properties to those of water, with the exception of PMMA, A-150 and plastic #1. Consequently, for these materials a discrepancy in $H^{\mathrm{MC}}_{pl,\mathrm{w}}$ factors calculated inside the chamber area and in a larger area was observed.

$H^{\mathrm{MC}}_{pl,\mathrm{w}}$ factors derived within a larger area for A-150, PMMA, and the three trial

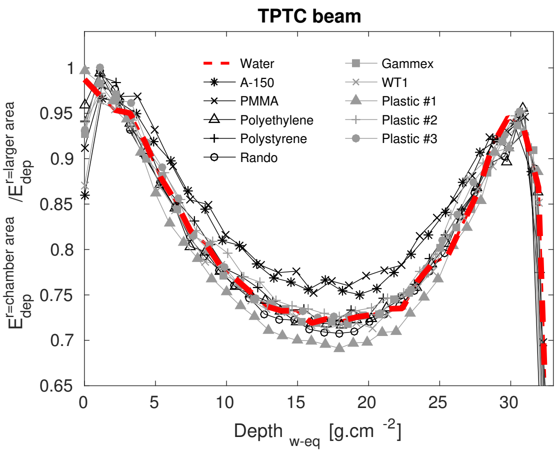

Figure 4.10: Ratio between the energy deposited due to secondary protons inside the radius of the Bragg peak chamber and in a larger radius for water and various plastic materials.

plastics are shown in figure 4.11. In comparison with the results from figure 4.8(a) for FLUKA, maximum $H_{pl,\mathrm{w}}^{\mathrm{MC}}$ values from figure 4.11(a) were about 0.5% higher for A-150 and PMMA and 0.5% smaller for plastic #1. For Geant4 results in figure 4.11(b), maximum $H_{pl,\mathrm{w}}^{\mathrm{MC}}$ values were approximately 0.5% smaller in absolute magnitude for A-150 and plastic #2 in comparison with results from figure 4.8(b). There were no significant differences between $H_{pl,\mathrm{w}}^{\mathrm{MC}}$ values calculated within different radii for plastic #3. These results can be compared with experimental h_{pl} values measured by Palmans *et al.* [10] for PMMA in an un-modulated 191 MeV proton beam. At a depth near the Bragg peak corrections of about 2% were reported. The magnitude of this correction is in better agreement with results from FLUKA, where maximum corrections were of the order of 1.5% than with results from Geant4 data, where maximum corrections were of the order of 0.5%.

Fluence correction factors were also calculated between water and plastic materials using FLUKA and Geant4, inside the area of the Bragg peak chamber (figure 4.12). As with the results for the CCC beam (figure 4.6), at the surface, $k_{\mathrm{fl}}^{\mathrm{MC}}$ values are about 0.5% lower than unity. This effect is less pronounced for Geant4 results, as previously reported by Palmans *et al.* [24], where fluence corrections were computed between water and graphite using five different Monte Carlo codes. Plastic #1 showed the largest variation of $k_{\mathrm{fl}}^{\mathrm{MC}}$ factors with depth, with deviations from unity ranging from -0.8% to 3% in FLUKA and from -0.1% to 2% in Geant4. For A-150 and PMMA, values varied from -1.5% to 1% in FLUKA and from -0.2% to -1.5% in Geant4. When using FLUKA, polyethylene was the plastic with the smallest variation (-0.5%-0.5%), whilst for Geant4 plastic #3 gave the smallest range

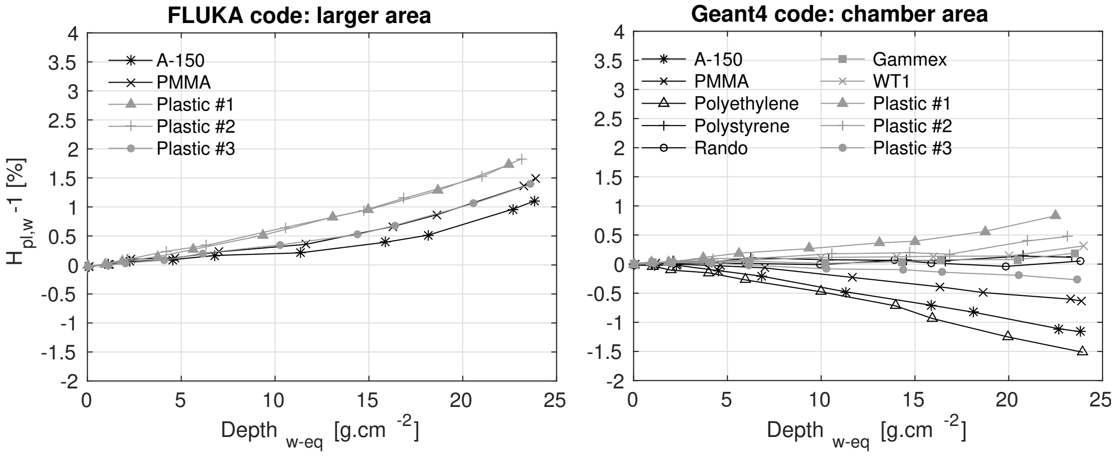

(a) (b)

Figure 4.11: Plastic-to-water conversion factor for various plastics in the TPTC beam, derived from Monte Carlo simulations (refer to equation 4.32) using (a) FLUKA and (b) Geant4 simulations, within an area larger than the Bragg peak chamber used in the experiments.

of values (-0.1%-0.5%). An interesting observation between figures 4.8 and 4.12 is that there is a high degree of correlation between $H_{pl,\mathrm{w}}^{\mathrm{MC}}$ and $k_{\mathrm{fl}}^{\mathrm{MC}}$, however, there are also distinct differences in their variations with depth. In chapter 2, fluence corrections were derived between water and graphite by experiments using setups 1 and 3 in a similar way as $H_{pl,\mathrm{w}}^{\mathrm{exp}}$ factors were measured in this chapter. The results suggested that secondary particles produced in the slab of material t_{pl} in setup 3 do not have enough energy to cross the chamber wall; therefore, these particles are not accounted for in the measured value. Fluence corrections measured experimentally were thus partial. Note that $k_{\mathrm{fl}}^{\mathrm{MC}}$, values are generally higher than $H_{pl,\mathrm{w}}^{\mathrm{MC}}$. In carbon-ion beams [44, 46], secondary particles spectra are mainly from projectile fragmentation and are emitted with sufficient energy to cross the chamber wall and, consequently, $H_{pl,\mathrm{w}} \approx k_{\mathrm{fl}}$ (see chapter 5).

Lühr *et al.* [15] performed a Monte Carlo study using the SHIELD-HIT10A code to determine fluence corrections for PMMA in comparison to water in light-ion beams. For high-energy beams, PMMA was shown to be water-equivalent with an uncertainty of 1%. Al-Sulaiti *et al.* [13] calculated fluence corrections for A-150 and PMMA in a 60 MeV and 200 MeV proton beams using the MCNPX Monte Carlo code and analytical model calculations. Corrections were found to be smaller than 1%. Another study from Al-Sulaiti *et al.* [14] aimed to study the water equivalence of the following plastic materials: PW, PWDT and WT1. Measurements were performed in a 60 MeV proton beam and compared with Monte Carlo simulations using the

FLUKA code for 60 and 200 MeV proton beams. Fluence corrections were less than 1% for the 60 MeV beam and roughly 3% for the 200 MeV. As evident from these studies and from the results presented here, fluence corrections are energy, material and code dependent. Palmans *et al.* [10] estimated fluence corrections for PMMA and polystyrene with reference to water in low- and high- energy clinical proton beams using an adapted version of the PTRAN Monte Carlo code using non-elastic nuclear interaction data from ICRU Report 63 and Janni [73] tables. They concluded that corrections were dependent on the nuclear data used and that results were inconclusive with regards to the most accurate dataset. Similarly, the work presented here does not allow us to conclude which Monte Carlo method gives a more accurate representation of the experimental data in figure 4.7.

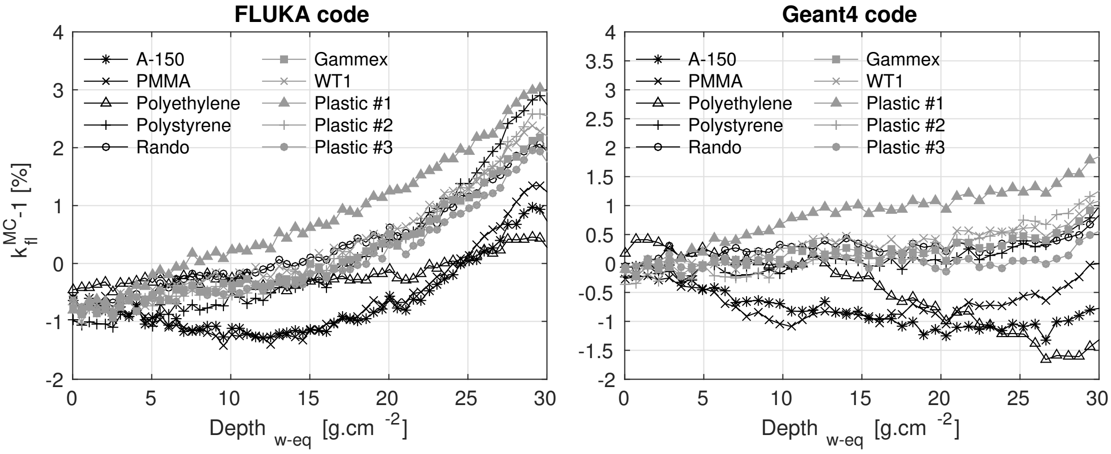

(a) (b)

Figure 4.12: Fluence correction factor for various plastics in the TPTC beam, derived from Monte Carlo simulations using (a) FLUKA and (b) Geant4 codes, inside the area of the Bragg peak chamber.

4.6 Conclusions

In this study, the dosimetric water-equivalence of three trial plastics, designed for light-ion beams, as well as, some commercially available plastics was evaluated for proton beams. The water-equivalence was evaluated by computing a plastic-to-water conversion factor, $H_{pl,\mathrm{w}}$. The trial materials were characterized experimentally in 60 MeV and 226 MeV un-modulated proton beams and the results were compared with Monte Carlo simulations. Fluence correction factors, k_{fl}, were also derived using the Monte Carlo method.

For the 60 MeV proton beam, maximum deviations of $H_{pl,\mathrm{w}}$ and k_{fl} factors from unity were of the order of 1% for all trial plastics. For the 226 MeV proton beam, experimental $H_{pl,\mathrm{w}}$ values were about 1% higher than unity for the three trial plastics and experimental results showed no preference regarding the most water-equivalent plastic. The main reason that low-Z materials - such as phantom materials – are not water-equivalent in proton beams is the difference in the nuclear interaction cross sections between different elements. Different magnitudes of corrections were found between Geant4 and FLUKA for the various materials in consideration because the nuclear data are different depending on the code. These differences are nevertheless consistent with the large uncertainties on nuclear interaction cross sections. Experimental $H_{pl,\mathrm{w}}$ values measured in this work showed no preference with regards to the most accurate dataset, while experimental data from Palmans *et al.* [10] and from Moyers *et al.* [74] was in better agreement with FLUKA results. Nevertheless, maximum $H_{pl,\mathrm{w}}$ corrections were within 2% for all the materials. Considering the results from the two codes, PMMA and plastic #3 were the materials with smallest $H_{pl,\mathrm{w}}$ corrections, where maximum values were about 1%.

Overall, k_{fl} factors were higher in magnitude than $H_{pl,\mathrm{w}}$ factors and could amount to a few percent for some materials dependent on the code used. This can have important consequences when comparing dose to water calculated from treatment planning systems to dose to tissue from Monte Carlo simulations.

In summary, the results indicated that plastic #3 and PMMA are the most suitable water-substitutes for the measurement of dose to water using ionization chambers in clinical proton beams, however, PMMA is not water-equivalent when range and scattering are concerned.

Chapter 5

Water-equivalence of plastic materials in a clinical high-energy carbon-ion beam

The work presented in this chapter has been accepted for publication in the Physics in Medicine and Biology journal:

- **A. Lourenço**, N. Wellock, R. Thomas, M. Homer, H. Bouchard, T. Kanai, N. MacDougall, G. Royle, H. Palmans, "Theoretical and experimental characterisation of novel water-equivalent plastics in clinical high-energy carbon-ion beams", Physics in Medicine and Biology **61**, 7623-38 (2016)

My contributions to this publication were as follows; novel water-equivalent plastics were designed by me and produced in collaboration with St Bartholomew's Hospital (UK); experiments at the Gunma University Heavy Ion Medical Center (Japan) were performed by me with the assistance of NPL staff and local contacts; analysis and interpretation of the results and Monte Carlo simulations were performed by me under guidance of my supervisors and NPL staff; the paper was written by me and proof-read by the co-authors.

5.1 Summary

Water-equivalent plastics are frequently used in dosimetry for experimental simplicity. This work evaluates the water-equivalence of novel water-equivalent plastics specifically designed for light-ion beams, as well as commercially available plas-

tics in a clinical high-energy carbon-ion beam. The water-equivalence of materials was tested by computing the plastic-to-water conversion factor, $H_{pl,\mathrm{w}}$. The three trial plastic materials with varying atomic compositions were experimentally characterised in a high-energy carbon-ion beam. Measurements were performed with a Roos ionization chamber, using a broad un-modulated beam of $11 \times 11\,\mathrm{cm}^2$, to measure the plastic-to-water conversion factor for the novel materials. The experimental results were compared with Monte Carlo simulations, using the FLUKA code. Commercially available plastics were also simulated for comparison with the plastics tested experimentally, with particular attention to the influence of nuclear interaction cross sections. The measured $H_{pl,\mathrm{w}}^{\mathrm{exp}}$ correction increased gradually from 0% at the surface to 0.7% at a depth near the Bragg peak for one of the plastics prepared in this work, while for the other two plastics a maximum correction of 0.8%-1.3% was found. Average differences between experimental and numerical simulations were 0.2%. Monte Carlo results showed that for polyethylene, polystyrene, Rando phantom soft tissue and A-150, the correction increased from 0% to 2.5-4.0% with depth, while for PMMA it increased to 2%. Water-equivalent plastics such as, Plastic Water, RMI-457, Gammex 457-CTG, WT1 and Virtual Water, gave similar results, where maximum corrections were of the order of 2%. Considering the results from Monte Carlo simulations, one of the novel plastics was found to be superior in comparison with the plastic materials currently used in dosimetry, demonstrating that it is feasible to tailor plastic materials to be water-equivalent for carbon ions specifically.

5.2 Rationale

In the most recent international codes of practice for the dosimetry of radiotherapeutic carbon-ion beams [4, 21], water is the recommended medium for the determination of absorbed dose. However, for relative dosimetry, for quality assurance (QA) of reference and relative dosimetry and for treatment planning verification, water- or tissue-equivalent plastic materials are often used in the measurements for convenience of realizing the setup.

The water-equivalence and tissue-equivalence of phantom materials in light-ion beams is widely considered to be related to stopping powers and ranges [55, 75]. It is, however, also substantially influenced by the nuclear interaction cross sections, though this mechanism is less well quantified and understood. Nuclear interactions have important consequences on primary dosimetry using non-water calorimeters

[12, 24], reference and relative dosimetry in plastic water-substitute phantoms and dose verification in complex, anatomic and anthropomorphic phantoms [10]. Their importance has also been demonstrated for the comparison of dose calculations in tissue and in water [45, 76]. For carbon-ion beams, Inaniwa *et al.* [77, 78] investigated the influence of nuclear interactions on dose calculations in treatment planning. The effects were tumour site, fraction size and patient dependent and could be substantial in particular cases. Kanematsu *et al.* [79] calculated and experimentally verified the impact of using polyethylene range compensators on the spread-out Bragg peak (SOBP) dose in carbon-ion beams, with particular attention to the influence of nuclear interactions. They reported corrections of 3% in extreme cases when a range compensator of 20 cm needs to be used and a correction of the order of 1% in most clinical cases.

Palmans and Verhaegen [80] indicated that the main source of differences in the shape of the Bragg peak between low-Z materials is due to differences in the non-elastic nuclear interaction cross sections. Palmans *et al.* [10] established a fluence correction factor, k_{fl}, to account for the difference in the particle fluences between water and plastic materials in proton beams. With regards to the fluence correction factor for carbon-ion beams, fewer studies have been carried out compared to electron and proton beams [10, 13, 14, 24, 81]. Lühr *et al.* [15] performed a Monte Carlo study, using SHIELD-HIT10A, to determine fluence corrections for PMMA, bone and graphite in comparison to water in carbon-ion and proton beams.

As mentioned in chapter 4, to convert ionization chamber readings in a plastic phantom to the equivalent reading in a water phantom, the IAEA TRS-398 Code of Practice [4] established a fluence scaling factor, h_{pl}. Thwaites *et al.* [26] calculated fluence scaling factors between water and plastic phantoms for electron beams. The results showed that measured values of h_{pl} were dependent on the ionization chamber and beam energy. This has been further investigated by Ding *et al.* [9] for clear polystyrene, white polystyrene and PMMA phantom materials and by McEwen and DuSautoy [82] for the water-equivalent material WTe. For photon beams, Seuntjens *et al.* [83] conducted a study to measure the h_{pl} factor in six water-equivalent plastics.

In this work, the novel plastic materials described in chapter 4 were experimentally characterised at the Gunma University Heavy Ion Medical Center, using a carbon-ion beam of 290 MeV/n, and compared with various commercially available plastics using Monte Carlo simulations. The water-equivalence of the materials was tested by calculating a plastic-to-water conversion factor, $H_{pl,\text{w}}$, in a similar way as was previously proposed for proton beams (chapter 4).

5.3 Theory

5.3.1 Measurement of absorbed dose to water in a plastic using an ionization chamber

In chapter 4, three epoxy-resin based mixtures of water-equivalent plastics, specifically formulated for light-ion beams, were experimentally characterized in proton beams. A plastic-to-water conversion factor $H_{pl,\mathrm{w}}$ was established and measured as an approximation of h_{pl}, using a more practical experimental setup from which WET values could also be derived. In this study, the trial compositions were characterized experimentally in a high-energy carbon-ion beam, using the previously developed formal framework by application of this methodology to carbon-ion beams.

In this work, ionization chamber readings were performed in setups 1 and 3 similarly as in chapter 4 (figure 5.1). The $H_{pl,\mathrm{w}}$ factor was determined experimentally using equation 4.30 and numerically using equation 4.32.

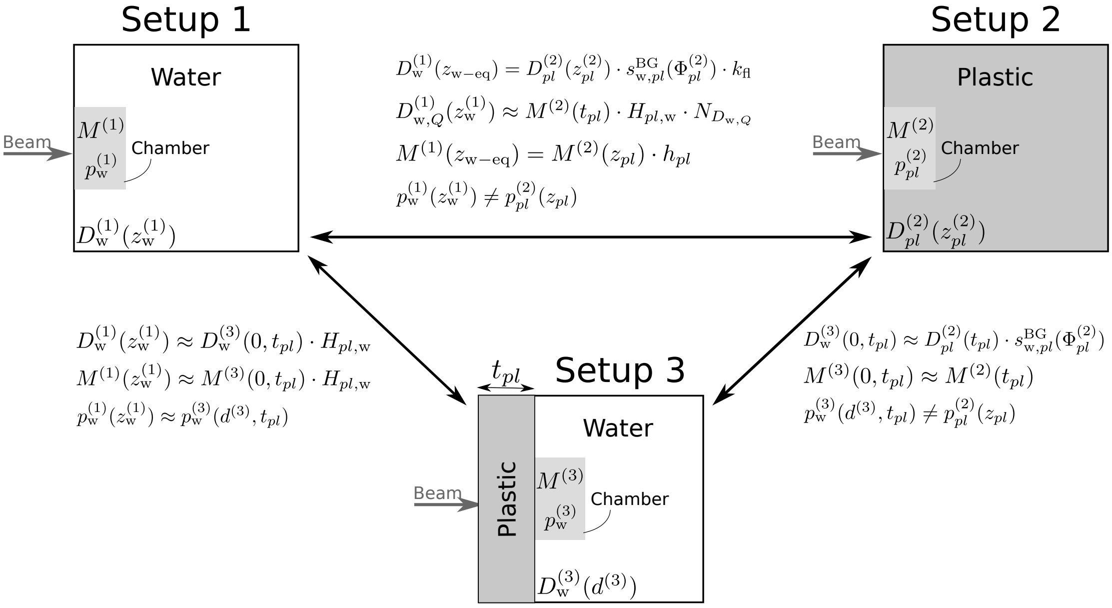

Figure 5.1: Schematic representation of the experimental setups under consideration and their respective relations.

5.3.2 Relation between $H_{pl,\mathrm{w}}$ and k_{fl}

The fluence correction factor, k_{fl}, can be calculated from a ratio of doses between two materials from equation 3.1 and by a ratio of fluences from equation 3.2 using setups 1 and 2.

In setup 3, at the interface between a slab of thickness t_{pl} and the water phantom, when $d^{(3)} = 0$, it can also be considered that the fluence will be the same as in setup 2 at $z_{pl}^{(2)} = t_{pl}$, i.e. $\Phi_{\mathrm{w}}^{(3)}(0, t_{pl}) \approx \Phi_{pl}^{(2)}(t_{pl})$. This assumption can be applied for carbon-ion beams because secondary particle spectra are mainly from projectile fragmentation. Therefore, they are emitted with similar velocity to the projectile and will have larger ranges, contrary to proton beams where, e.g., alpha particles emitted by target fragmentation with very short ranges have substantial influence (see section 2.3.1). Thus, dose in setup 3 for $d^{(3)} = 0$ can be written as:

$$D_{\mathrm{w}}^{(3)}(0, t_{pl}) \approx \sum_i \left[\int_{E_{\min,i}}^{E_{\max,i}} \Phi_{E,pl,i}^{(2)}(E) \cdot \left(\frac{S_i(E)}{\rho} \right)_{\mathrm{w}} \cdot dE \right] \tag{5.1}$$

Furthermore, dose in setup 2 is defined as $D_{\mathrm{w}}^{(2)}(t_{pl}) = \sum_i \left[\int_{E_{\min,i}}^{E_{\max,i}} \Phi_{E,pl,i}^{(2)}(E) \cdot \left(\frac{S_i(E)}{\rho} \right)_{pl} \cdot dE \right]$ for $z_{pl}^{(2)} = t_{pl}$. The ratio between dose to water in setup 3 given by equation 5.1 and dose to plastic in setup 2, gives,

$$\frac{D_{\mathrm{w}}^{(3)}(0, t_{pl})}{D_{pl}^{(2)}(t_{pl})} \approx \frac{\sum_i \left[\int_{E_{\min,i}}^{E_{\max,i}} \Phi_{E,pl,i}^{(2)}(E) \cdot \left(\frac{S_i(E)}{\rho} \right)_{\mathrm{w}} \cdot dE \right]}{\sum_i \left[\int_{E_{\min,i}}^{E_{\max,i}} \Phi_{E,pl,i}^{(2)}(E) \cdot \left(\frac{S_i(E)}{\rho} \right)_{pl} \cdot dE \right]} \approx s_{\mathrm{w},pl}^{\mathrm{BG}}(\Phi_{pl}^{(2)}) \tag{5.2}$$

Thus,

$$D_{\mathrm{w}}^{(3)}(0, t_{pl}) \approx D_{pl}^{(2)}(t_{pl}) \cdot s_{\mathrm{w},pl}^{\mathrm{BG}}(\Phi_{pl}^{(2)}) \tag{5.3}$$

Combining equations 4.29 and 4.31 with equation 5.3:

$$\frac{M^{(1)}(z_{\mathrm{w}}^{(1)})}{M^{(3)}(0, t_{pl})} \approx \frac{D_{\mathrm{w}}^{(1)}(z_{\mathrm{w}}^{(1)})}{D_{\mathrm{w}}^{(3)}(0, t_{pl})} \approx \frac{D_{\mathrm{w}}^{(1)}(z_{\mathrm{w-eq}})}{D_{\mathrm{g}}^{(2)}(z_{\mathrm{g}}^{(2)}) \cdot s_{\mathrm{w,g},i}^{\mathrm{BG}}(\Phi_{\mathrm{g}}^{(2)})} = k_{\mathrm{fl}}(z_{\mathrm{w-eq}}) \tag{5.4}$$

Consequently, $k_{\mathrm{fl}} \approx H_{pl,\mathrm{w}}$. In chapter 2 [84], fluence correction factors between water and graphite were calculated in proton beams using similar methods. However, for proton beams, fluence corrections derived from setups 1 and 3 were found to be partial fluence corrections since they account only for primary and part of the secondary particles spectra. In these beams, secondary particles, such as alpha particles, which originated from target fragmentation with very short ranges, do not have sufficient energy to cross the chamber's wall.

In summary, $H_{\mathrm{pl,w}}^{\mathrm{exp}}$ factors were measured experimentally from equation 4.30 and $H_{pl,\mathrm{w}}^{\mathrm{MC}}$ and $k_{\mathrm{fl}}^{\mathrm{MC}}$ factors were calculated using Monte Carlo simulations from equations 4.32, 3.1 and 3.2, respectively.

5.4 Methods

5.4.1 Water-equivalent plastics

The plastic materials prepared in this work consist of epoxy resins and were produced in collaboration with the St Bartholomew's Hospital, UK, based on earlier experience from White *et al.* [56–58] and Constantinou *et al.* [59].

Three plastic materials were produced based on the same epoxy resin system (epoxy resin + hardener), referred as plastics #1, #2 and #3, respectively (section 4.3.3). Powders with varying atomic low-Z numbers were added to the resin in order to change the atomic number of the final. Gas-filled spheres called phenolic microspheres (PMS) were added in the composition of the resin in order to adjust the density of the final compound to approximately $1\,\mathrm{g.cm^{-3}}$. For each plastic formulation, three slabs of 4 cm, 5 cm and 8 cm thickness were machined from the same batch.

5.4.2 Measurements

The plastic-to-water conversion factor $H_{pl,\mathrm{w}}^{\mathrm{exp}}$ was measured for the three novel plastics. Measurements were performed in the clinical carbon synchrotron at the Gunma University Heavy Ion Medical Center (GHMC), Japan [49]. A 290 MeV/n carbon-ion beam was provided by a wobbling delivery system [47, 48] which magnetically scanned the scattered beam.

Measurements were performed in a broad collimated field of $11 \times 11\,\mathrm{cm}^2$ without beam modulation. As shown in figure 5.2, a cylindrical Farmer ionization chamber (PTW type 30011) was placed in the corner of the beam exit in order to monitor the beam. Central axis measurements were performed using a plane-parallel Roos ionization chamber (PTW type 34001) with a sensitive diameter of 1.5 cm. The Roos chamber was kept at a constant source-to-detector distance (SDD), in order to avoid corrections for the divergence of the beam. A water phantom was placed in front of the beam, with the phantom surface aligned with the isocenter. The water phantom was moved towards the beam in order to change the amount of water in front of the static Roos chamber. This was repeated with slabs of water-equivalent plastics of variable thicknesses attached to the front window of the water phantom. Finally, for each slab of plastic tested with thickness t_{pl}, $H_{pl,\mathrm{w}}^{\mathrm{exp}}$ was determined by application of equation 4.30.

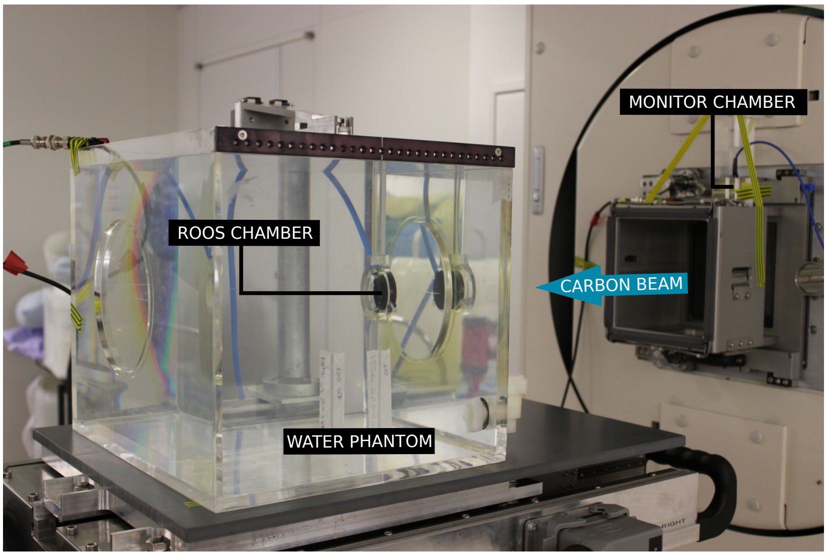

Figure 5.2: Experimental setup.

5.4.3 Monte Carlo simulations

Monte Carlo simulations were performed with the FLUKA code version 2011.2c.3 [16, 17]. To calculate $H_{pl,\mathrm{w}}^{\mathrm{MC}}$ using equation 4.32, depth-dose distributions were calculated in water (setup 1) and in water after passing through slabs of plastic with variable thickness (setup 3). The simulated slabs had the same thickness and density of those tested experimentally. For comparison with $H_{pl,\mathrm{w}}^{\mathrm{MC}}$, $k_{\mathrm{fl}}^{\mathrm{MC}}$ was also calculated using the dose and the fluence approaches, from equations 3.2 and 3.1, respectively. Fluence differentials in energy and dose were scored in bins of 0.1 cm and 0.007 cm thick, respectively, within cylindrical volumes of 1.5 cm diameter (equal to the sensitive diameter of the Roos chamber used in the experiments). For each simulation, 25×10^6 particles were simulated for a broad carbon-ion beam of $11 \times 11\,\mathrm{cm}^2$. A beam with no divergence was considered in the simulations because it corresponded to a better approximation of the experiments performed with constant SDD.

Commercially available plastics were also simulated by Monte Carlo for comparison with the three trial compositions of water-equivalent plastics characterised in this work. The following plastics were included: A-150, PMMA, polyethylene, polystyrene, RANDO® phantom (The Phantom Laboratory, Salem, NY, USA), Plastic Water® (CIRS, Norfolk, VA, USA), RMI-457 (GAMMEX, Middleton, WI, USA), Virtual Water™ (Med-Cal, Middleton, WI, USA), Gammex 457-CTG (CTG Solid Water®: GAMMEX, Middleton, WI, USA) and WT1 (St Bartholomew's Hospital, London, UK). Existing plastics were defined in terms of elemental mass fractions, density and mean excitation energy (a.k.a. I-value) as stated in ICRU Reports

37 [60] and 49 [27] and IAEA TRS-398 Code of Practice [4]. When experimentally determined I-values were not available, I-values were obtained by the application of the Bragg additivity rule for compounds [60].

5.4.4 Experimental and Monte Carlo uncertainties

The sources of experimental uncertainties to determine $H^{\mathrm{exp}}_{pl,\mathrm{w}}$ are presented in table 5.1 [36]. Type A uncertainties were calculated as one standard deviation of the mean of repeated observations. Type B uncertainties included temperature and pressure and standard deviation of the mean values $H^{\mathrm{exp}}_{pl,\mathrm{w}}$ at all calculated depths. Ratios of ionizations were measured (standard chamber/monitor chamber) with the same type of electrometer, therefore, type B uncertainties related to electrometer calibrations were correlated and cancelled out. Uncorrelated uncertainties, such as fluctuations and drifts, were considered negligible for the electrometer used. Uncertainties related to the determination of equivalent depths between setups 1 and 3 were also considered negligible. This becomes mainly a large uncertainty close to the Bragg peak because of the high sensitivity to positioning errors in depth. Therefore, those points were not considered in equations 4.30 and 4.32 to calculate $H_{pl,\mathrm{w}}$.

Table 5.1: Experimental relative standard uncertainties.

Sources of uncertainty (%)	Type A	Type B
Standard/Monitor ratio	0.32	-
Temperature	-	0.05
Pressure	-	0.05
$s_{\overline{H^{\mathrm{exp}}_{pl,\mathrm{pl}}}}$	-	0.16
Overall	**0.32**	**0.18**
Combined (%)	**0.37**	

Type A uncertainties from Monte Carlo simulations were below 0.3% and type B uncertainties were not considered. Type B Monte Carlo uncertainties are more challenging to estimate than type A. Type B Monte Carlo uncertainties include uncertainties from stopping-power data and interaction cross sections. Böhlen *et al.* [32] conducted a study to benchmark nuclear models implemented in FLUKA for carbon-ion beams. The authors concluded that FLUKA code predicted experimental data with reasonable accuracy, although further improvements were needed since the existing experimental data was limited and had large uncertainties. Stopping powers from different models were compared with experimental data in ICRU Report 73

[50]. Overall, data agreed to within 10% with higher accuracy for energies above 10 MeV/n, however, for energies below 0.1 MeV/n, uncertainties were larger due to considerable disagreement between experimental data and models [50]. Note that in equation 3.1 the same stopping power data are used in the numerator and denominator, therefore, the correlation in these uncertainties is large and cancel out. Although in equation 3.2 the uncertainty contribution from the stopping-power ratio has a large influence, it will be strongly correlated with the ratio of calculated doses [24].

5.5 Results and discussion

5.5.1 Tuning of the beam model and benchmarking of the simulations

Monte Carlo simulations were first validated against experimental data and results in the literature. In Monte Carlo, both the beam energy and the Gaussian energy spread were tuned to achieve good agreement between the experimental and simulated curves. This correction resulted in a mean beam energy of 265 MeV/n with a standard deviation of $\sigma = 0.75\,\text{MeV}$ incident at the phantom surface. In figure 5.3, a relative dose curve as a function of measurement depth acquired during the experiments is compared with a depth-dose distribution from Monte Carlo simulations. The assumption is made that ionization in the chamber is proportional to dose (equation 3.8). Both distributions were normalized to the integral of the curves. The tail beyond the Bragg peak is due to the fragmentation of primary carbon ions which produces secondary particles with a smaller mass and similar velocity to the projectile. Consequently, these lighter fragments will deposit their energy at a depth beyond the Bragg peak, to which mostly lighter fragments ($1 \leq Z \leq 2$) contribute.

Figure 5.4 shows the contribution of primary and secondary particles in water. The following particles were scored: primary carbon ions, secondary particles with Z=1 (protons, deuterons, tritons), Z=2 (isotopes of helium ^{3}He,^{4}He), Z=3 (isotopes of lithium ^{6}Li, ^{7}Li), Z=4 (isotopes of beryllium ^{7}Be, ^{9}Be, ^{10}Be), Z=5 (isotopes of boron ^{12}B, ^{1}3B) and Z=6 (isotopes of carbon ^{10}C, ^{11}C, ^{12}C). Other isotopes and neutrons with a contribution to the dose of the order of 0.001% were not scored. Unlike fragments, primary particles do not contribute to the tail dose shown in figure 5.4(a). The contribution of fragments increases in depth and a maximum is reached in the Bragg peak. Beyond the Bragg peak their contribution decreases gradually

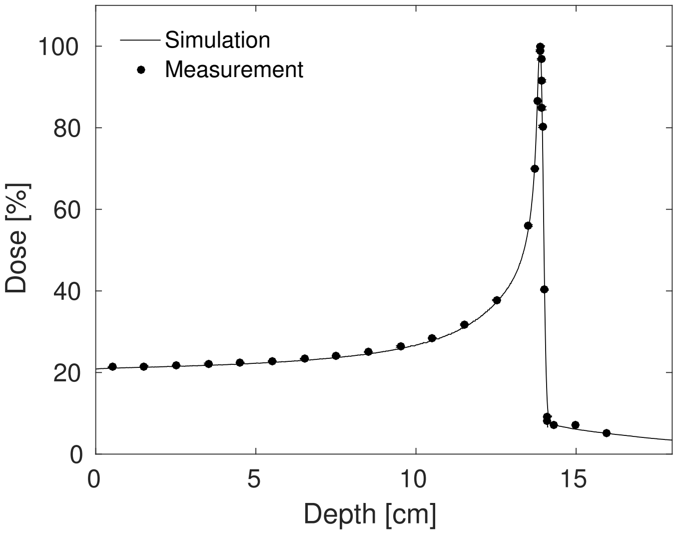

Figure 5.3: Measured and simulated depth-dose curves in water. Experimental error bars are smaller than the marker points. Maximum differences between experimental points and Monte Carlo were of the order of 2%.

because there are no primary particles producing secondary particles. Results are in agreement with experimental data from Haettner *et al.* [46] and with previous Monte Carlo studies from Kempe *et al.* [51] and Rossomme *et al.* [12], using SHIELD-HIT and Geant4/GATE codes, respectively.

5.5.2 Plastic-to-water conversion factor

Figure 5.5 shows the plastic-to-water conversion factor for the three novel plastics characterised experimentally. In the graphs, data are included that were obtained from experiments, $H_{pl,\mathrm{w}}^{\mathrm{exp}}$, and from Monte Carlo simulations, $H_{pl,\mathrm{w}}^{\mathrm{MC}}$. For comparison, the results from $k_{\mathrm{fl}}^{\mathrm{MC}}$ are also shown. Results from $H_{pl,\mathrm{w}}$ and k_{fl} factors for the different plastics are shown as percent corrections in comparison to water. The approaches $k_{\mathrm{fl,fluence}}^{\mathrm{MC}}$ and $k_{\mathrm{fl,dose}}^{\mathrm{MC}}$ are strongly linked (0.05% difference) [24] and the results between methods were consistent. For simplification, the results from the latter have not been included in the graphs.

For plastic #1, average differences between experimental data and numerical simulations were of the order of 0.20% for $k_{\mathrm{fl,fluence}}^{\mathrm{MC}}$ and 0.10% for $H_{pl,\mathrm{w}}^{\mathrm{MC}}$. Differences were larger for plastic #2, where mean values were 0.24% and 0.38% for $k_{\mathrm{fl,fluence}}^{\mathrm{MC}}$ and $H_{pl,\mathrm{w}}^{\mathrm{MC}}$, respectively. For plastic #3, average differences between experimental data and numerical simulations were of the order of 0.15% for $k_{\mathrm{fl,fluence}}^{\mathrm{MC}}$ and 0.10% for $H_{pl,\mathrm{w}}^{\mathrm{MC}}$. The production process of plastics has uncertainties and the assumed compositions

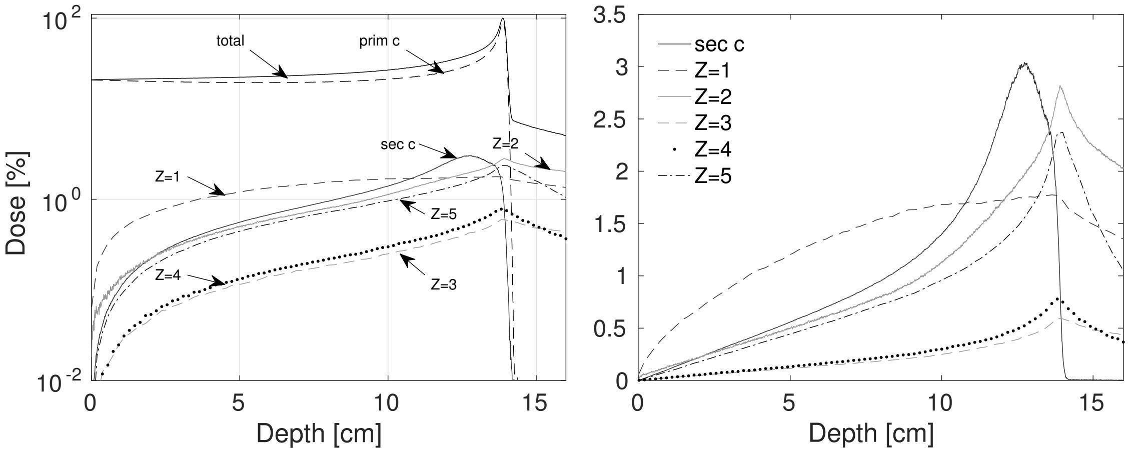

(a) (b)

Figure 5.4: Monte Carlo simulations of absorbed dose curves as a function of depth in water, for different set of particles (prim c = primary particles, sec c = secondary carbon ions, and particles with atomic numbers Z=1, Z=2, Z=3, Z=4 and Z=5).

may not always be consistent with the ones produced. The latter may explain small discrepancies between experimental and numerical methods. Nevertheless, these results suggest that $H_{pl,\mathrm{w}}^{\mathrm{exp}}$, obtained experimentally from setups 1 and 3, account for all charged particles and ensure the validity of the assumptions considered. The good agreement between $H_{pl,\mathrm{w}}^{\mathrm{MC}}$ and $k_{\mathrm{fl}}^{\mathrm{MC}}$ implies that they are comparable. The latter is easier to implement in Monte Carlo since a single simulation is enough to calculate $k_{\mathrm{fl}}^{\mathrm{MC}}$ with depth, whereas $H_{pl,\mathrm{w}}^{\mathrm{MC}}$ requires a simulation for each thickness of material in order to obtain its variation with depth.

Experimental data showed no preference regarding the most water-equivalent plastic with measured $H_{pl,\mathrm{w}}^{\mathrm{exp}}$ values amounting to a maximum of 0.8% for plastic #1, while for plastic #2 and plastic #3 a maximum correction of 0.7% and 1.3% was found, respectively. Considering the results from Monte Carlo simulations, for plastics #1 and #3, $H_{pl,\mathrm{w}}^{\mathrm{MC}}$ increased towards 2% with depth, while for plastic #2 it increased gradually towards 0.5%. The different rate of variation of $H_{pl,\mathrm{w}}^{\mathrm{MC}}$ with depth between the different plastics suggest that varying the concentration of an additive to the epoxy resin system enables the properties of the materials to be altered towards water-equivalence.

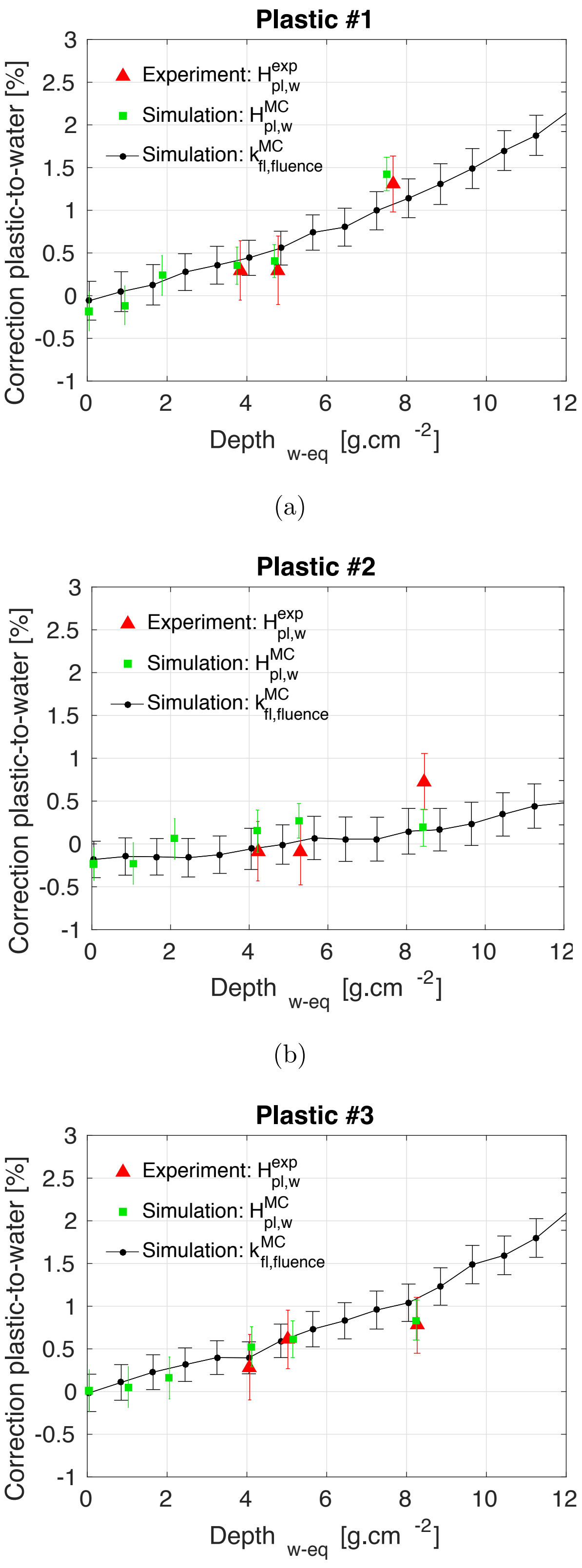

(a)

(b)

(c)

Figure 5.5: Plastic-to-water corrections for three trial compositions of water-equivalent plastics: (a) plastic #1, (b) plastic #2 and (c) plastic #3. Triangles represent the values of $H^{\mathrm{exp}}_{pl,\mathrm{w}}$ calculated experimentally (refer to equation 4.30), squares represent the values of $H^{\mathrm{MC}}_{pl,\mathrm{w}}$ calculated using Monte Carlo methods (equation 4.32) and circles represent the values of $k^{\mathrm{MC}}_{\mathrm{fl,fluence}}$ (refer to equation 3.1).

In figure 5.6, plastic #2 is compared with various commercially available plastic materials, using Monte Carlo simulations since only a limited amount of experimental data is available in the literature. Moreover, the maximum difference between Monte Carlo and experimental data for the three in-house plastics in figure 5.5 was 0.57%. For this purpose, $k^{\mathrm{MC}}_{\mathrm{fl,fluence}}$ was calculated due to its easy implementation in Monte Carlo. For polyethylene, polystyrene, A-150 and Rando phantom soft tissue the correction increased from 0% to 2.5-4.0% at a depth near the Bragg peak, while for PMMA it increased towards 2%. Water-equivalent plastics such as, Plastic Water, RMI-457, Gammex 457-CTG, WT1 and Virtual Water, gave similar results, where maximum corrections were of the order of 1.5%-2.5%. Plastic #2 gave the most promising results with $k^{\mathrm{MC}}_{\mathrm{fl,fluence}}$ varying between 0.0%-0.5% with depth. Similar results were found by Lühr *et al.* [15] for PMMA. The latter performed a Monte Carlo study, using SHIELD-HIT10A code, to determine fluence corrections for PMMA in comparison to water in 107 MeV/n, 270 MeV/n and 400 MeV/n carbon-ion beams. For high-energy beams PMMA was shown to be water equivalent with an uncertainty of 1%. For the 107 MeV/n carbon-ion beam, corrections were close to unity, while for the higher-energy beams corrections deviated from unity by 0% at the surface to 1%-2% at a depth near the Bragg peak.

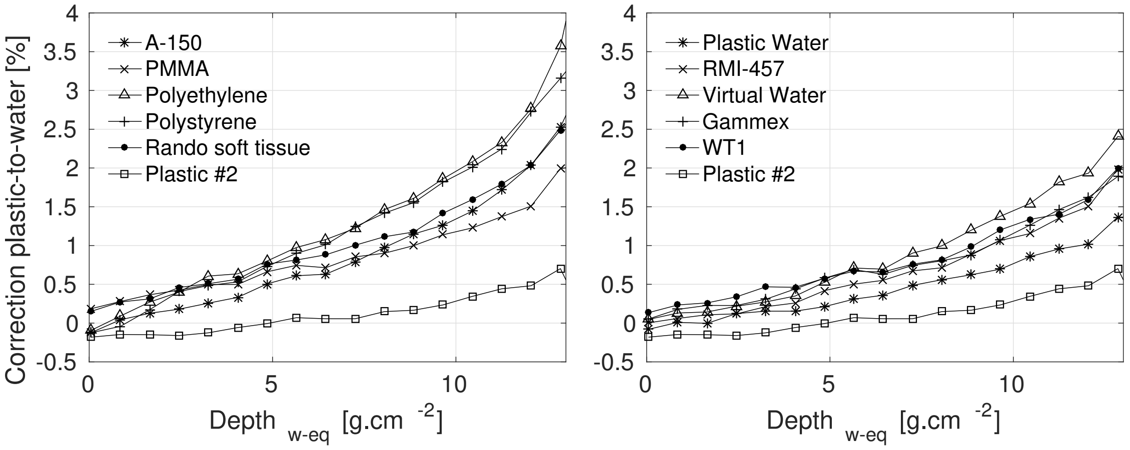

(a) (b)

Figure 5.6: Dose conversion corrections from plastic-to-water for various plastic materials commercially available and for plastic #2.

5.6 Conclusions

In this work, a plastic-to-water conversion factor, $H_{pl,\mathrm{w}}^{\mathrm{exp}}$, was established to derive absorbed dose to water in a water phantom from ionization chamber readings performed in a plastic phantom for carbon ion-beams. Three trial plastic materials with varying atomic compositions, produced based on epoxy resins, were characterised experimentally in a high-energy carbon-ion beam. Experimental data showed no preference regarding the most water-equivalent plastic with measured $H_{pl,\mathrm{w}}^{\mathrm{exp}}$ values amounting to a maximum of 0.7%-1.3%. Considering the results from Monte Carlo simulations, the good agreement between $H_{pl,\mathrm{w}}^{\mathrm{MC}}$ and $k_{\mathrm{fl}}^{\mathrm{MC}}$ suggested that they are comparable. For plastics #1 and #3 it was found that the simulated plastic-to-water correction increased towards 2% at a depth near the Bragg peak, while for plastic #2 the correction increased gradually towards 0.5%. Plastic #2 was found to be superior to plastics commercially available with a $k_{\mathrm{fl}}^{\mathrm{MC}}$ correction 1.0%-3.5% smaller at larger depths.

This work presents a proof-of-principle that varying the concentration of an additive to the epoxy resin system alters the properties of the plastics towards water-equivalence. This work will feed into the development of water- and tissue-equivalent materials for light-ion beams.

Chapter 6

Fano cavity test and ionization chamber perturbation factors

6.1 Summary

The aim of this chapter was to study the influence of ionization chamber perturbation factors since in the previous chapters it was assumed that the ratio of ionization chamber perturbation factors between setups 1 and 3 differed from unity by a negligible amount. These correction factors are very sensitive to boundary crossing artifacts, therefore, a self-consistency test called the Fano cavity test, was performed to evaluate the accuracy of particle transport in the FLUKA Monte Carlo code for proton beams. A routine was written in FLUKA to generate a uniform proton source per unit of mass. Simulations were performed for mono-energetic protons with initial energies of 60 MeV, 150 MeV and 250 MeV. To study the influence of different subsets of secondary charged particle types, three simulations with different charged particle transport were performed for each proton energy considered; (i) all charged particles transported, (ii) alpha particles discarded and (iii) nuclear interactions discarded. FLUKA was found to pass the Fano test to within 0.1%. Ionization chamber perturbation factors were also computed for the PTW 34070 Bragg peak chamber for proton beams of 60 MeV, 100 MeV, 150 MeV, 200 MeV and 250 MeV. The results showed that the presence of the air cavity introduces a perturbation in the medium of the order of 0.2% away from unity, while the chamber's wall introduces a perturbation that could amount to 0.8%. The results also showed that nuclear interactions must be taken into account for calculation of ionization chamber response and that perturbation factors are dependent on the proton energy.

6.2 Rationale

Monte Carlo (MC) codes are used to calculate the depth-dose response of ionization chambers accurately. Although a high level of statistical accuracy can be achieved with Monte Carlo simulations (type-A uncertainties), there are other uncertainties associated with these codes (type-B uncertainties). The latter include uncertainties related to the physical models implemented in the codes, the physical data used and the transport algorithms [85]. While physical models and data uncertainties can be evaluated by benchmarking results against experimental data, transport algorithm uncertainties can be evaluated by performing a self-consistency test called the Fano cavity test [86]. This test is based on Fano's theorem [87] and it states that under conditions of charged particle equilibrium (CPE), the charged particle fluence will not be altered by mass density variations whilist the cross-sections are uniform. Monte Carlo calculations of ionization chamber response are very sensitive to transport algorithm parameters, such as step size and boundary crossing artefacts [88, 89]. Thus, the Fano cavity test is an important step to understand which combinations of parameters lead to accurate particle transport to compute ionization chamber perturbation factors using Monte Carlo.

The accuracy of electron transport algorithms has been validated in several Monte Carlo codes, such as EGSnrc [90], PENELOPE [91, 92] and Geant4 [93]. More recently Sterpin *et al.* [85] have designed a Fano cavity test for proton transport using Geant4 and PENELOPE extended to protons (PENH). Both codes were found to pass the Fano cavity test to within 0.1% by using small step sizes. In their work, the transport of electrons was neglected as well as nuclear interactions. However, electrons and nuclear interactions must be taken into account for calculation of ionization chamber response.

In this work, the accuracy of particle transport in the FLUKA Monte Carlo code for proton beams was assessed by performing a Fano cavity test, with particular attention to the influence of nuclear interactions. Ionization chamber perturbation factors were also computed for the PTW 34070 Bragg peak chamber typically used in clinical proton beams.

6.3 Methods

6.3.1 Fano cavity test

The Fano cavity test can be implemented in Monte Carlo using two methods:

(i) One method is the regeneration technique where an external parallel beam is used and primary particles are regenerated at the site of primary interaction. For protons, this is not possible (due to continuous energy loss of the primary particles) and, therefore, Sterpin *et al.* [85] implemented this method by creating a virtual particle that triggers proton transport in the phantom [85].

(ii) The other method is to create an homogeneous particle source, similar to a radionuclide. In such a source, protons are randomly generated, giving a uniform particle distribution per unit mass in the simulated geometry. This method has the advantage of being independent of the cross sections of incident particles.

Here, the second method was used to perform the Fano cavity test.

6.3.1.1 Simulation model

To implement the method described above, the following is required:

(i) A phantom with homogeneous atomic properties (cross sections, I-value, density effect parameters, etc.) but varying mass densities.

(ii) An homogeneous source, such that the number of particles per unit mass generated in the geometry is uniform in space.

These two conditions allow applying Fano's theorem.

Monte Carlo simulations were performed with FLUKA version 2011.2c.4 [16, 17]. A routine was written in FLUKA to generate a uniform proton distribution by mass using a customized modification of the "source.f" user-routine, which was then linked to the code. Simulations were performed for mono-energetic protons with initial energies of 60 MeV, 150 MeV and 250 MeV. A plane-parallel beam was simulated instead of an isotropic point source because protons have a smaller scattering cross section than electrons due to their much heavier mass. The geometry (discussed in section 6.3.1.2) consisted of a phantom made of water, divided into different regions with different mass densities but with the same composition, Sternheimer density effect parameters and I-value which was set to 75 eV. The following physics settings were used in FLUKA:

- The DEFAULTS card was set to HADROTHErapy;
- The IONTRANS card was set to full transport of all ions;
- The DELTARAY card was used to switch off the production of delta-rays by setting the production threshold to infinity since it was not the aim of this work to study the accuracy of electron transport in FLUKA;
- The PART-THRes card was used to set the energy transport cutoff for protons to 10 keV. Other charged particles transport cutoffs were set to 100 keV by default.
- The MULSOPT card was used to activate single scattering at boundaries;
- The STEPSIZE card was used to set the maximum step size of all charged particles to 0.01 cm (discussed in section 6.4.1.1).

To study the influence of different subsets of secondary charged particle types, three simulations with different charged particle transport were computed for each proton energy considered:

(i) $\mathrm{T}_{\mathrm{all}}$ where all charged particles were transported;

(ii) $\mathrm{T}_{\mathrm{alpha}}$ where alpha particles were killed by zeroing its weight (particles are generated hence the proton loses energy but they are not transported) using a "usrmed.f" user-routine which was linked to the code and activated using MAT-PROP with SDUM = USERDIRE;

(iii) T_{ni} where elastic and non-elastic nuclear interactions were switched off by setting the energy threshold for these interactions very high using the THRESHOL card.

6.3.1.2 Geometry

Figure 6.1 illustrates the simulation geometry where plane-parallel protons are randomly generated uniformly by mass in the phantom made of water. The geometry is divided in two regions, the build-up and the CPE. Protons have a finite range determined by their initial energy, thus, the build-up region is made large enough to ensure that the CPE region is at a depth beyond the maximum range of the protons generated at $z = 0$. In this way, charged particle equilibrium is achieved in the CPE region. Protons have a smaller scattering cross section than electrons due to their much heavier mass, therefore, x and y dimensions do not need to be as large as the range of the protons generated along the central axis, z. The field size dimensions, $x \times y$, were $36 \times 36\,\mathrm{cm}^2$ to ensure CPE in the cavity. The ionization chamber has a wall thickness of 0.347 cm and 10.395 cm in diameter, while the low-density water cavity was 0.2 cm thick and 8.16 cm in diameter. The latter correspond to the dimensions of the PTW 34070 Bragg peak chamber. The ionization chamber setup was overridden to water-property materials but it was kept the original mass densities of the materials. The blue colour indicates a phantom with density equal to water, $\rho_\mathrm{w} = 1\,\mathrm{g.cm}^{-3}$, while the cavity (light blue) has a density equal to air, $\rho_\mathrm{air} = 0.00120484\,\mathrm{g.cm}^{-3}$ and the ring that surrounds the cavity (dark blue) has a density equal to the densest material in the chamber, graphite, $\rho_\mathrm{g} = 1.7\,\mathrm{g.cm}^{-3}$. The choice of the depths upstream and downstream of the chamber, z_u and z_d, respectively, will be discussed in section 6.4.1.1. The code accuracy was then tested by comparing the dose scored in the different mass density regions.

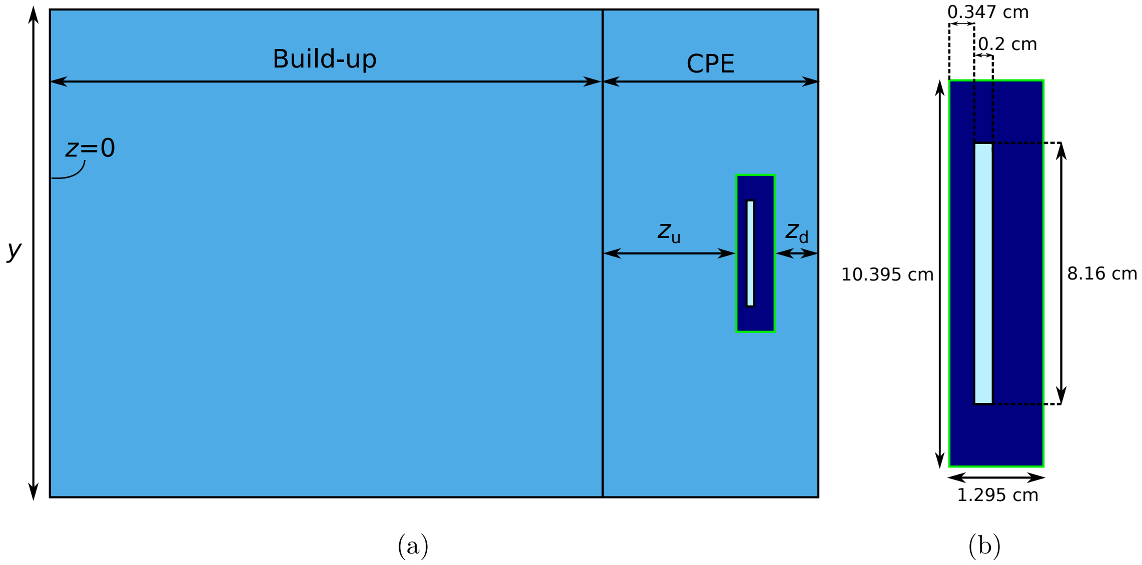

Figure 6.1: (a) Simulation geometry of the Fano cavity test. (b) Dimensions of the chamber considered in this study. Adapted from Poon *et al.* [93] and Sterpin *et al.* [85].

6.3.2 Perturbation correction factors

Dose to water, D_w, is related to dose to air, D_chamber, by the Spencer-Attix mass stopping power ratio between water and air, $s^\mathrm{SA}_\mathrm{w,air}$, and p_cav and p_wall which are perturbation correction factors that account for the non-water equivalence of the air

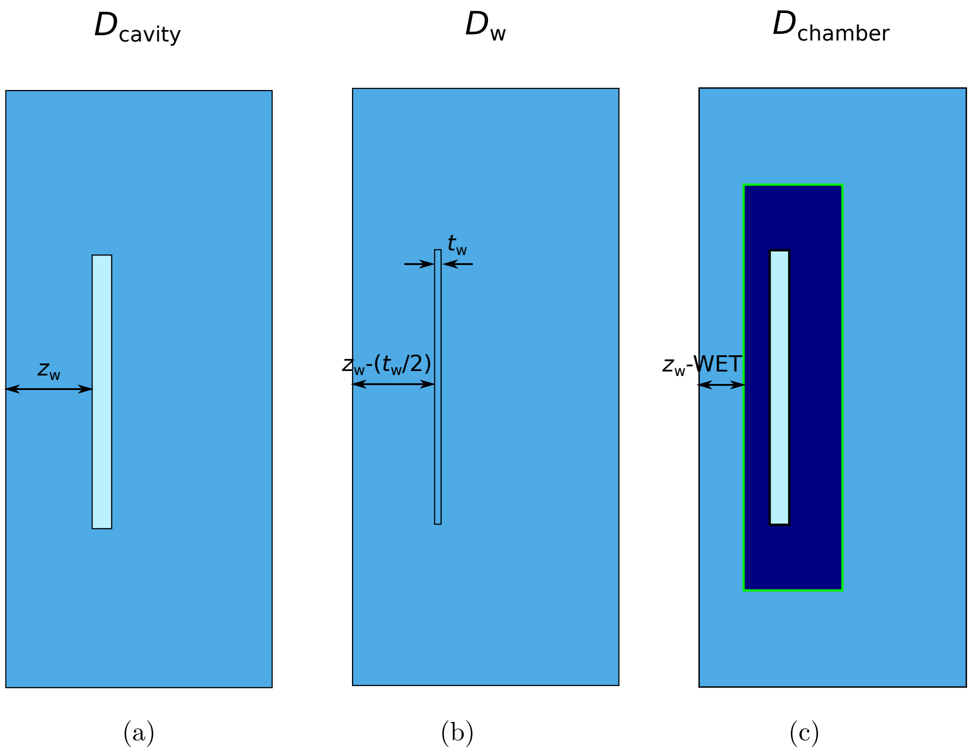

Figure 6.2: Simulations geometry for calculation of ionization chamber perturbation factors. (a) Dose in the air cavity, (b) dose to water and (c) dose in the air cavity when the full geometry of the ionization chamber is considered [95].

cavity and the chamber's wall, respectivelly [94]:

$$D_{\mathrm{w}} = D_{\mathrm{chamber}} \cdot s_{\mathrm{w,air}}^{\mathrm{SA}} \cdot p_{\mathrm{cav}} \cdot p_{\mathrm{wall}} \tag{6.1}$$

Note the analogy to equation 2.3 established in chapter 2. Thus, perturbation factors are fluence corrections that account for the perturbation of the charged particle fluence due to the presence of the air cavity and chamber's wall.

Ionization chamber perturbation factors can be determined by calculating the dose in different geometries as illustrated in figure 6.2 [95]. D_{cavity} is the dose in the air cavity at a depth of measurement z_{w}. D_{w} is the dose to water calculated in a thin layer ($t_{\mathrm{w}} = 0.01\,\mathrm{cm}$) at a depth of measurement $z_{\mathrm{w}} - (t_{\mathrm{w}}/2)$. D_{chamber} is the dose in the air cavity when the full geometry of the ionization chamber is considered at a depth of measurement $z_{\mathrm{w}} - \mathrm{WET}$, where WET is the water equivalent thickness of the chamber's wall [95]. Thus, ionization perturbation factors were calculated using:

$$p_{\mathrm{wall}} = \frac{D_{\mathrm{cavity}}}{D_{\mathrm{chamber}}} \tag{6.2}$$

and,

$$p_{\text{cav}} \cdot s_{\text{w,air}}^{\text{BG}} = \frac{D_{\text{w}}}{D_{\text{cavity}}} \tag{6.3}$$

In this work, the production of delta-rays was neglected thus Bragg-Gray mass stopping power ratios, $s_{\text{w,air}}^{\text{BG}}$, were calculated. The combined perturbation p_{Q} is then given by:

$$p_{\text{Q}} = p_{\text{wall}} \cdot p_{\text{cav}} = \frac{D_{\text{w}}}{D_{\text{chamber}} \cdot s_{\text{w,air}}^{\text{BG}}} \tag{6.4}$$

Perturbation factors calculations were performed with FLUKA version 2011.2c.4 [16, 17]. The physics settings were the same as those described in section 6.3.1.1 The full geometry of the PTW 34070 Bragg peak chamber was modelled. A mono-energetic proton beam of 60 MeV was simulated, where a depth of measurement of $z_{\text{w}} = 1\,\text{cm}$ was used, while for proton beams of 100 MeV, 150 MeV, 200 MeV and 250 MeV, $z_{\text{w}} = 2\,\text{cm}$ was used. Proton beams were incident on cylindrical phantoms of water ($\rho = 1.0\,\text{g.cm}^{-3}$ and I-value = 75 eV) with 10 cm radius. Moreover, to study the influence of different subsets of secondary charged particle types, three simulations with different charged particle transport, T_{all}, T_{alpha} and T_{ni}, were computed for each proton energy considered.

6.4 Results and discussion

6.4.1 Proton Fano test

6.4.1.1 Boundary crossing artefacts

Figure 6.3 shows the depth-dose distribution of an uniform-source mono-directional proton beam of 250 MeV. The data were obtained using a similar geometry to that shown in figure 6.1(a), but with a phantom made of water with a density of $1\,\text{g.cm}^{-3}$ throughout the phantom. After a build-up region of approximately 38 cm (the range of the beam in water), there is charged-particle equilibrium, thus, the CPE region starts at this depth, where the dose is uniform. When the phantom was divided into two regions of water (with equal material composition, I-value and density) by placing a boundary at a depth of 45 cm, the results showed an artefact at the boundary, as shown in figure 6.4(a).

In FLUKA, at the scoring level, the proton energy loss is distributed uniformly along the particle step, thus, the dose value scored at each depth bin is proportional

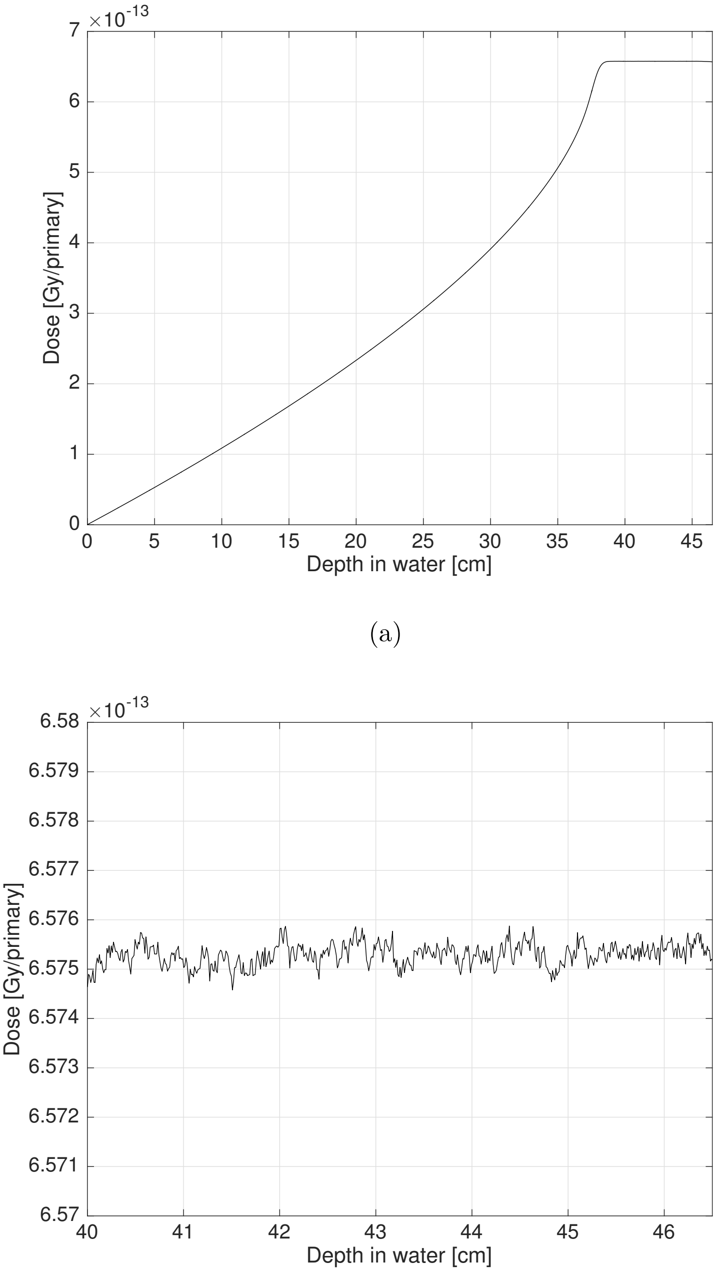

(a)

(b)

Figure 6.3: (a) Depth-dose distribution of an uniform-source mono-directional proton beam of 250 MeV in water, with density 1 g.cm^{-3} throughout the phantom. (b) Detail of CPE region.

to the respective step fraction. However, in reality, the stopping power increases non-linearly along the step, and is larger towards the step end. At boundaries, the particles steps are forced to end, which makes the respective scored dose lower than in the case of non-existence of the boundary, because the dose is not compensated by larger dose values from the final fraction of the particle step. Note that the non-

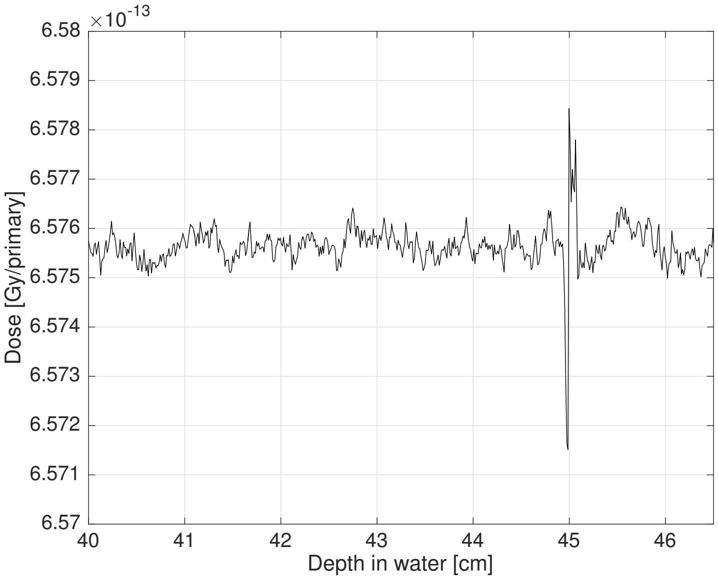

(a)

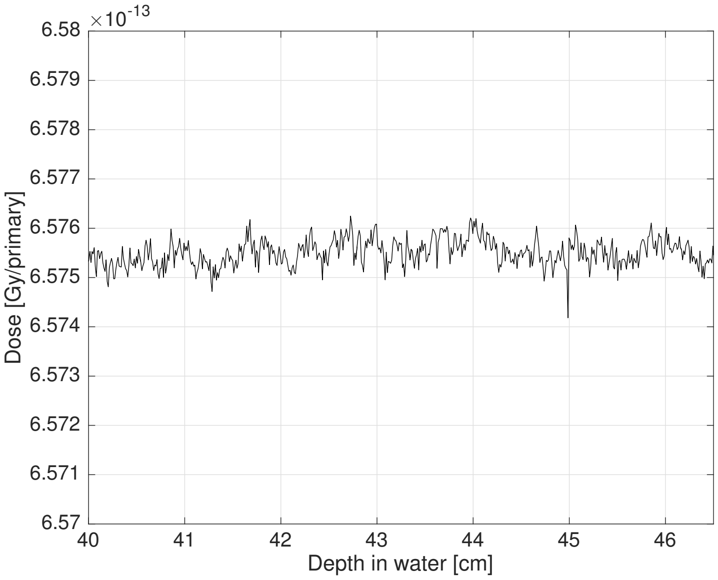

(b)

Figure 6.4: Detail of CPE regions using a (a) large and (b) small step sizes. The geometry consists of two identical regions of water at a depth of 45 cm.

linearity of the stopping power is fully taken into account in FLUKA, however, the scoring considers that the dose is uniformly distributed along the step and artefacts appear [16, 17].

Boundary crossing artefacts were removed by shortening all transport steps down to 0.01 cm using STEPSIZE card (figure 6.4(b)). This increased significantly the CPU time, thus, small step sizes were only applied to the CPE region. A boundary was created just after the start of the CPE region and the depth upstream of the chamber, z_{u}, was made 13 cm for higher-energy beams and 6 cm for lower-energy beams to correct for the scoring artefacts at the position of the latter [16, 17]. The depth downstream of the chamber, z_{u}, was 2 cm since backscattered protons have a minor effect.

6.4.1.2 Cavity response

Homogeneous plane-parallel proton beams of 60 MeV, 100 MeV and 250 MeV were simulated in the geometry shown in figure 6.1(a). Figure 6.5 shows the ratio between the dose scored in the water-property regions with different mass densities. Overall, FLUKA was found to pass the Fano test to within 0.1%. When all charged particles were considered maximum deviations from unity of about 0.15% were found. Type-A statistical uncertainties were below 0.05%.

6.4.2 Perturbation factors

Figure 6.6(a) shows the Bragg-Gray mass stopping power ratio between water and air calculated when considering the contribution of different set of particles. The results show that the stopping power ratio for the protons alone is close to the stopping power ratio for the entire charged particle spectrum, confirming earlier findings, e.g. by Medin and Andreo [96]. The Bragg-Gray mass stopping power ratio between water and air was also calculated when considering different charged particle transport in figure 6.6(a). The results were in agreement with those of figure 6.6(b). For example, when elastic and non-elastic nuclear interactions are discarded, T_{ni}, there is no production of secondary particles and the only particles that contribute to the ratio are primary protons thus the curve coincides with the primary proton curve of figure 6.6(a).

Figure 6.7 shows ionization chamber perturbation factors as a function of proton energy, when considering the transport of different charged particles. When nuclear interactions are discarded, T_{ni}, perturbation factors are close to unity for all the energies considered. For p_{cav} the largest deviations from unity were of 1.002 for T_{alpha} and 0.999 for T_{all}. These results demonstrate that the presence of the air cavity introduces a small perturbation in the medium. Deviations from unity were larger for p_{wall} which was found to be dependent on proton energy. For a 250 MeV beam and considering the transport of all charged particles, p_{wall} was significantly different from unity (p_{wall} = 0.992), while for a 60 MeV beam, it deviated less (p_{wall} = 0.996). It is also interesting to note that not only alpha particles contribute to p_{wall} but also other secondary particles (T_{all} versus T_{a}). Overall, p_{wall} factors were below unity. These results suggest that less particles are being stopped in the wall or less particles are being produced in water than in the chamber's wall. The latter is in agreement with the results presented in chapter 2 where fluence correction factors between water and graphite were below unity when alpha particles were considered, consequently, alpha particles fluence was larger in graphite than in water. Note that the chamber's wall is composed of PMMA which has in its composition carbon.

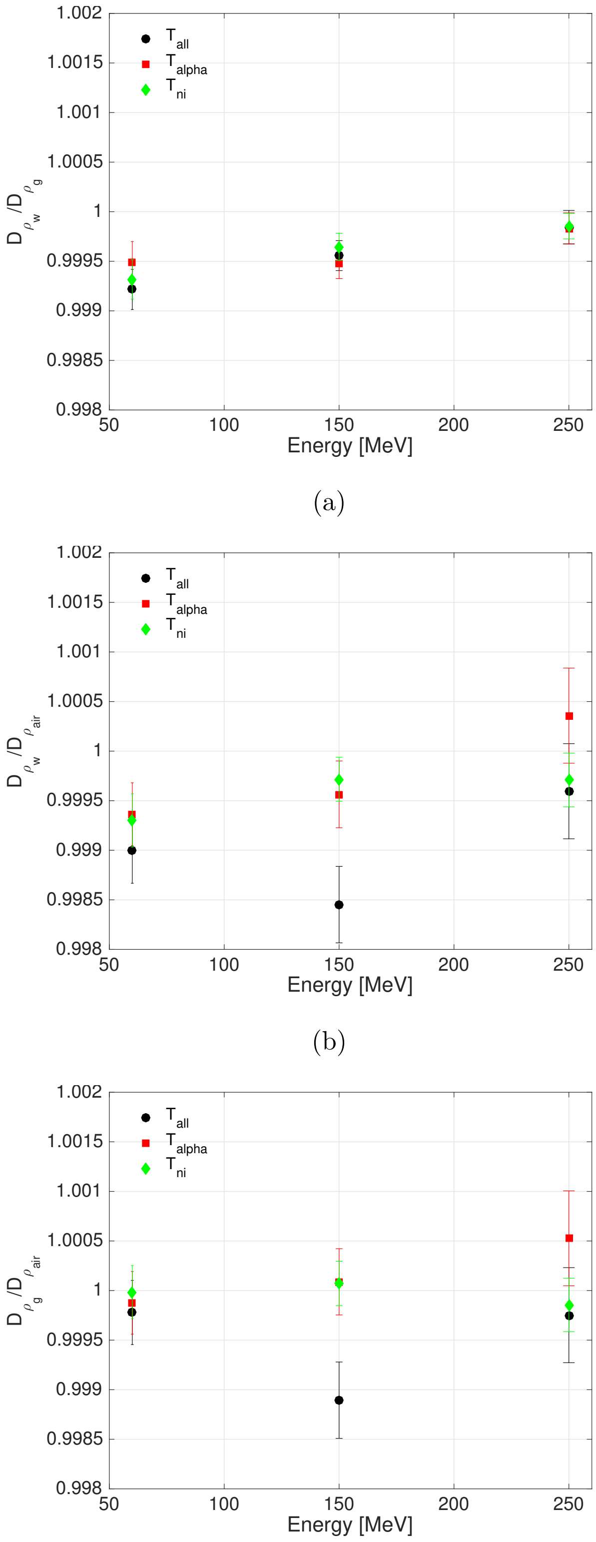

(a)

(b)

(c)

Figure 6.5: Ratio between the dose scored in water-property materials with different mass densities: (a) water with nominal density, $\rho_{\mathrm{w}} = 1\,\mathrm{g.cm^{-3}}$, and water with graphite density, $\rho_{\mathrm{g}} = 1.7\,\mathrm{g.cm^{-3}}$, (b) water with nominal density, $\rho_{\mathrm{w}} = 1\,\mathrm{g.cm^{-3}}$, and water with air density, $\rho_{\mathrm{air}} = 0.00120484\,\mathrm{g.cm^{-3}}$, and (c) water with graphite density, $\rho_{\mathrm{g}} = 1.7\,\mathrm{g.cm^{-3}}$, and water with air density $\rho_{\mathrm{air}} = 0.00120484\,\mathrm{g.cm^{-3}}$, when all charged particles were transported, T_{all}, alpha particles discarded, T_{alpha}, and elastic and non-elastic nuclear interactions discarded, T_{ni}.

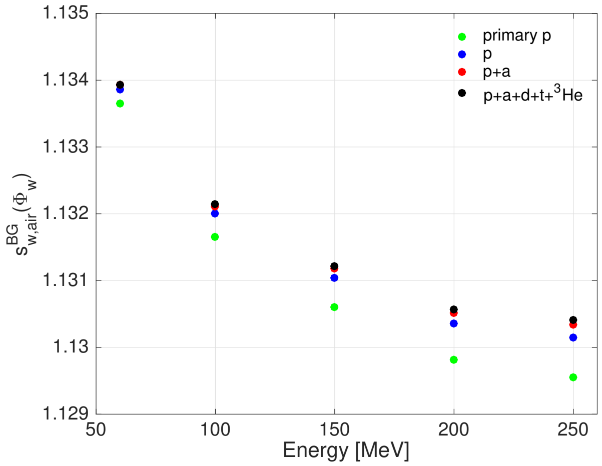

(a)

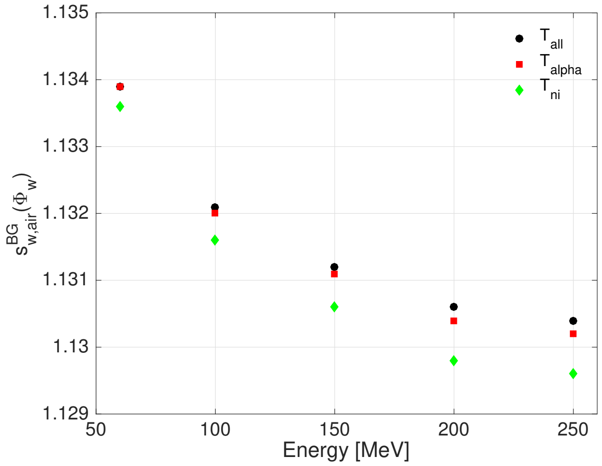

(b)

Figure 6.6: Bragg-Gray mass stopping power ratio between water and air calculated (a) for different set of particles and (b) for different charged particle transport (primary p = primary protons, p = primary and secondary protons, a = alphas, d = deuterons, t = tritons, ^{3}He ions, T_{all} = all charged particles transported, T_{alpha} = alpha particles discarded and T_{ni} = elastic and non-elastic nuclear interactions discarded).

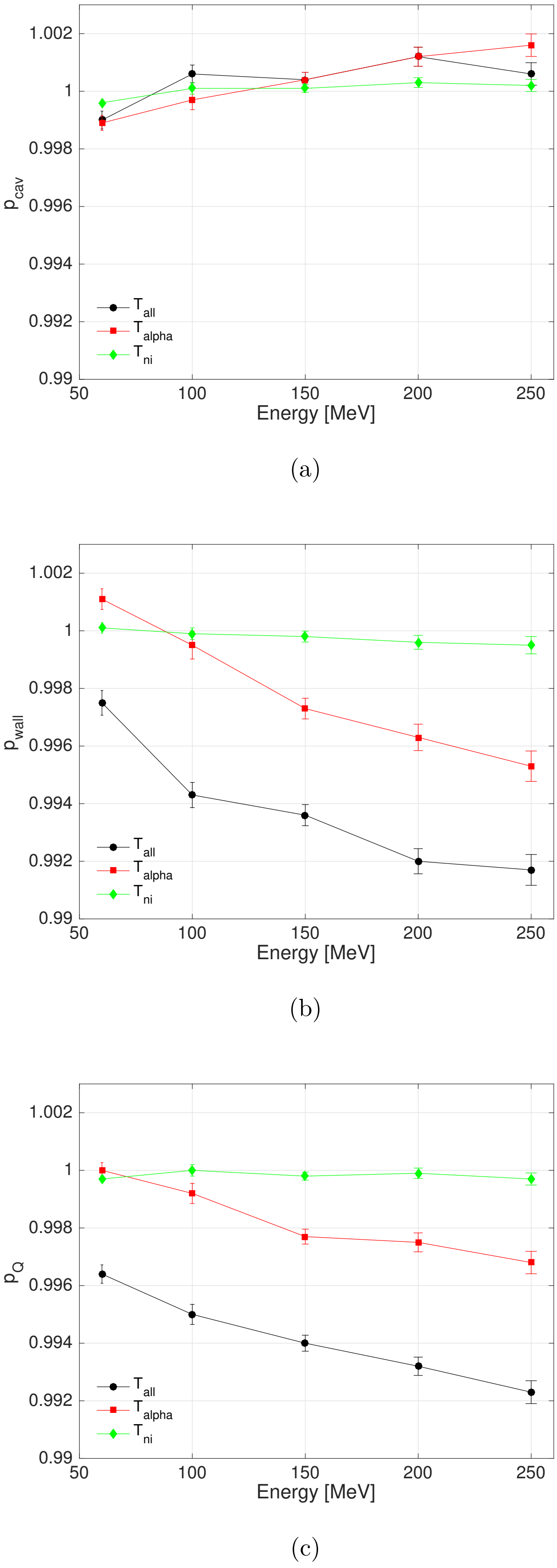

(a)

(b)

(c)

Figure 6.7: Ionization chamber perturbation factors versus proton energy: (a) p_{cav}, (b) p_{wall} and (c) p_{Q}.

6.5 Conclusions

The accuracy of particle transport in the FLUKA Monte Carlo code for proton beams was assessed by performing a Fano cavity test. FLUKA was found to pass this test to within 0.1%. Ion-chamber perturbation factors were also computed for the PTW 34070 Bragg peak chamber typically used in clinical proton beams. The results showed that nuclear interactions must be taken into account for calculation of ionization chamber response since perturbation corrections could amount to 0.8% when all charged particles were transported. Also, perturbation factors showed to be dependent on the proton energy.

In the previous chapters, the PTW 34070 Bragg peak chamber was used in the experiments and it was assumed that the ratio of ionization chamber perturbation factors between setups 1 and 3 differed from unity by a negligible amount. The results in this chapter support this assumption, since perturbation factors showed a weak dependence on energy, with a maximum variation of 0.6% for proton initial energies ranging from 60 MeV to 250 MeV. In addition, the setups are compared at equivalent depths, i.e., at equivalent proton mean energies, therefore, the small differences in spectra between setups 1 and 3 are likely to have a negligible influence on the ratio of ionization chamber perturbation factors.

Chapter 7

Final remarks

The growing interest in light-ion therapy in recent decades has led to a need for accurate dosimetry. The quantity of interest in radiation therapy dosimetry is absorbed dose to water, and the determination of this quantity must be accurate, reproducible and traceable in order to assure tumour control and mitigate normal tissue complications. Currently, no primary standards for the direct determination of absorbed dose to water in light-ion beams exist. Ionization chamber dosimetry under reference conditions is currently performed, although this leads to larger dose uncertainties for light-ions in comparison with photons. The increased uncertainty is due to lack of knowledge in the beam quality correction factor k_{Q}, which is originated by inaccuracies in the W_{air} value, in the water-to-air stopping power ratios and in the calculation of ionization chamber perturbation factors [5]. Moreover, for relative dosimetry, QA of reference and relative dosimetry, and treatment planning verification, water- or tissue-equivalent plastic materials are often used in the measurements for convenience of realizing the setup. Therefore, it is important to understand the water-equivalence of plastic materials which are currently being used in light-ion clinics, but were designed for photon and electron beams.

The work described in this thesis has made a contribution to the field by (i) improving absolute dosimetry using graphite calorimetry in light-ion beams, (ii) the development of water-equivalent plastics for light-ion beams and (iii) determination of ionization chamber perturbation factors with particular attention to the influence of nuclear interactions for proton beams.

Fluence correction factors important for the conversion of absorbed dose to graphite from a graphite calorimeter to absorbed dose to water were determined both experimentally and using Monte Carlo calculations in clinical proton and carbon-ion beams. An experimental setup involving measurements being done independently from ionization chamber perturbation factors caused by the use of different phantom materials was used to measure fluence corrections. Moreover, a mathematical formalism was established that relates fluence corrections derived from Monte Carlo simulations to fluence corrections measured experimentally. Fluence corrections in high-energy light-ion beams could amount to as much as 4% and therefore need to be considered. For proton beams, fluence corrections obtained experimentally were found to be partial because they only accounted for differences in the primary and part of the secondary particle fluence; the energy of alpha particles, emitted by target fragmentation, is not high enough to penetrate the wall of the ionization chamber used in the experiments, and these particles were not accounted for in the experimental fluence correction factor. For carbon-ion beams, the energies of secondary projectile fragments are large enough to cross the chamber wall and fluence corrections obtained from experiments were found to include all charged particles, with the exception of the less abundant heavy particles from target fragmentation.

Novel water-equivalent plastics were specifically designed for light-ion beams as part of this PhD project. In the design phase of the plastics, the propagation of proton beams through phantom materials was simulated using an analytical model. Three test compositions were then produced and experimentally characterised in proton and carbon-ion beams. Experimental results were compared with Monte Carlo simulations and material physical properties of the trial compositions were calculated and compared to those of water. Commercially available plastics were also simulated for comparison with the experimentally tested plastics. Experimental data showed that each of the novel water-equivalent plastics showed measurements of dose similar to water to within 1% across all depths of interest. Considering the results from Monte Carlo simulations, one of the novel plastics and PMMA were found to be the most suitable water-substitutes for the measurement of dose to water using ionization chambers in clinical proton beams - however, PMMA is not water-equivalent when range and scattering are concerned. For carbon-ion beams, Monte Carlo simulations showed that one of the novel plastics had superior water-equivalence to commercially available plastics, with a fluence correction 1.0%-3.5% smaller at larger depths.

Ionization chamber perturbation factors were also computed for the PTW 34070 Bragg peak chamber used in the experiments. In order to calculate this, the accuracy of particle transport in the FLUKA Monte Carlo code for proton beams was first assessed by performing a Fano cavity test, where transport in FLUKA showed an accuracy to within 0.1%. The results showed that nuclear interactions must be taken into account for the calculation of ionization chamber response since perturbation factors could amount to 0.8% when all charged particles were transported.

Although there were important results arising from this work, there is a great deal of future work still to be conducted. As mentioned above, for the conversion of dose to graphite to dose to water in proton beams, the results showed that the fluence corrections measured experimentally only accounted for part of the secondary particle spectra. Thus, the experiments could be repeated using an alternative detector, such as a thin-window ionization chamber, to sample the fraction of secondary particles with low-energy. Also, in this work water-equivalent plastics were developed, however, it would also be of interest to the field to develop tissue-equivalent materials for light-ion beams and investigate how to incorporate these materials into anthropomorphic phantoms used specifically for dosimetry in light-ion therapy. Additionally, the establishment of calorimeters as primary standards may significantly improve light-ion beam dosimetry. Calorimetric measurements would enable study of the energy and depth dependence of W_{air} values in these beams, to determine k_{Q} values experimentally and to establish a calibration service based on a primary standard. Moreover, the majority of the work conducted for this project was focused on understanding the influence of nuclear interactions in the dosimetry of light-ion beams. It should be emphasized that existing nuclear cross sections and Monte Carlo models are not completely accurate, thus, there is a demand to obtain more accurate nuclear cross sections based on experimental data. This could potentially be of importance for the improvement of dose calculations, such that the treatment planning system accounts for nuclear interactions. Also in proton imaging, by reconstructing the nuclear interactions cross sections and the production cross sections of the different secondary particles produced in the target and their respective energies.

In summary, the work presented here will enable the provision of a direct calibration service in terms of absorbed dose to water in the UK's forthcoming proton therapy centres. Also, this work will feed into the development of data for future codes of practice for the dosimetry of light-ion beams, as well as the development of new water or tissue equivalent materials.

Appendix A

Monte Carlo parameters

Monte Carlo simulations described in chapters 2, 3, 5 and 6 were performed using the FLUKA code. Simulations described in chapter 4 were performed using FLUKA and Geant4.

The simulation parameters used are listed in table A.1 for the different beam lines considered. The entire geometry of the CCC scattering beam line was simulated, therefore, the energy of the beam was defined at the source, while for the other beam lines, the beam line configuration was not considered in the numerical simulations and the beam energy was defined at the phantom surface. In Monte Carlo, both the beam energy and the Gaussian energy spread were tuned to achieve good agreement between the experimental and simulated Bragg peak curves.

A beam with no divergence was considered in the simulations for the CCC, PTC Czech and GHMC beam lines because it corresponded to a better approximation of the experiments performed with constant SDD.

For the experiments at CCC, PTC Czech and TPTC, laterally integrated measurements were performed in narrow beams. Thus, the scoring volumes were defined as stacks of a cylindrical geometry with a radius equal to the sensitive area as the chambers (r_{ch}) used in the experiments and also with a larger radius (r_{l}) to calculate the contribution of particles scattered outside the sensitive area of the chambers. For the experiments at GHMC, central axis measurements were performed using a broad beam and the scoring volume was defined with a radius equal to the sensitive area of the chamber used.

Delta-ray production was set to infinite threshold such that delta-ray production was not considered in the simulations. The most energetic secondary electrons have a short range of <1 mm and therefore all energy transferred to electrons can be regarded as absorbed locally. In chapter 6, to compute ionization chamber dose response accuratelly, secondary electrons must be taken into account. However, the influence of secondary electrons in proton beams was investigated previously [7, 8] and it was not the aim of this work to study the accuracy of electron transport in FLUKA and simulations were performed with particular attention to the influence of nuclear interactions.

For the CCC beam simulations, transport of neutrons was not considered because these particles are mainly generated in the materials of the beam line and neutron dose has been reported to be less than 0.001% of the treatment dose [35].

No variation reduction techniques were used.

Table A.1: Monte Carlo simulations parameters.

Beam lines	Parameters						
	Beam energy (MeV/n)	Energy spread (MeV)	Beam size	Divergence (mrad)	Scoring radii	Delta-ray production	Neutron transport
CCC	62.5 (at the source)	0.28	0.4 cm (collimator diameter)	0.0	r_{ch}=0.75 cm r_{l}=10 cm	No	No
PTC Czech	180 (at the phantom surface)	0.90	single spot (FWHM = 1.33 cm)	0.0	r_{ch}=4.08 cm r_{l}=10 cm	No	Yes
TPTC	226.14 (at phantom surface)	0.67	single spot	1.3	r_{ch}=4.08 cm r_{l}=10 cm	No	Yes
GHMC	265 (at the phantom surface)	0.75	11x11 cm^2	0.0	rr_{ch}=0.75 cm	No	Yes

Bibliography

[1]H. Paganetti, ed., *Proton Therapy Physics*, Series in Medical Physics and Biomedical Engineering (CRC, Florida, US, 2011) (cit. on pp. 29, 31, 41, 87, 88).

[2]S. N. Boon, *Dosimetry and Quality Control of Scanning Proton Beams* (University Library Groningen, 1998) (cit. on p. 30).

[3]H. Suit, T. DeLaney, S. Goldberg, H. Paganetti, B. Clasie, L. Gerweck, A. Niemierko, E. Hall, J. Flanz, J. Hallman, and A. Trofimov, “Proton vs carbon ion beams in the definitive radiation treatment of cancer patients”, Radiotherapy and Oncology: Journal of the European Society for Therapeutic Radiology and Oncology **95**, 3–22 (2010) (cit. on p. 29).

[4]P. Andreo, D. T. Burns, K. Hohlfeld, M. S. Huq, T. Kanai, F. Laitano, V. G. Smith, and S. Vynckier, *Absorbed dose determination in external beam radiotherapy: an international code of practice for dosimetry based on standards of absorbed dose to water. IAEA Technical Report Series TRS-398* (IAEA, Vienna, 2000) (cit. on pp. 30, 32, 41, 43, 54, 65, 76, 77, 89, 93, 95, 97, 110, 111, 116).

[5]C. P. Karger, O. Jäkel, H. Palmans, and T. Kanai, “Dosimetry for ion beam radiotherapy”, Physics in Medicine and Biology **55**, R193 (2010) (cit. on pp. 30, 31, 139).

[6]H. Palmans, F. Verhaegen, J.-M. Denis, S. Vynckier, and H. Thierens, “Experimental pwall and pcel correction factors for ionization chambers in low-energy clinical proton beams”, Physics in Medicine and Biology **46**, 1187 (2001) (cit. on p. 30).

[7]H. Palmans, and F. Verhaegen, “Monte Carlo study of fluence perturbation effects on cavity dose response in clinical proton beams”, Physics in Medicine and Biology **43**, 65 (1998) (cit. on pp. 30, 34, 144).

[8]F. Verhaegen, and H. Palmans, “A systematic Monte Carlo study of secondary electron fluence perturbation in clinical proton beams (70-250 MeV) for cylindrical and spherical ion chambers”, Medical Physics **28**, 2088–2095 (2001) (cit. on pp. 30, 34, 43, 66, 144).

[9] G. X. Ding, D. W. Rogers, J. E. Cygler, and T. R. Mackie, “Electron fluence correction factors for conversion of dose in plastic to dose in water”, Medical Physics **24**, 161–176 (1997) (cit. on pp. 32, 39, 111).

[10] H. Palmans, J. E. Symons, J. M. Denis, E. A. Kock, D. T. L. Jones, and S. Vynckier, “Fluence correction factors in plastic phantoms for clinical proton beams”, Physics in Medicine and Biology **47**, 3055–71 (2002) (cit. on pp. 32, 34, 40, 62, 77, 97, 98, 105, 107, 108, 111).

[11] H. Palmans, L. Al-Sulaiti, P. Andreo, R. A. S. Thomas, D. R. S. Shipley, J. Martinkovič, and A. Kacperek, “Conversion of dose-to-graphite to dose-to-water in a clinical proton beam”, in Standards, Applications and Quality Assurance in Medical Radiation Dosimetry - Proceedings of an International Symposium, Vol. 1 (2011), pp. 343–355 (cit. on pp. 33, 39, 41).

[12] S. Rossomme, H. Palmans, D. Shipley, R. Thomas, N. Lee, F. Romano, P. Cirrone, G. Cuttone, D. Bertrand, and S. Vynckier, “Conversion from dose-to-graphite to dose-to-water in an 80 MeV/A carbon ion beam”, Physics in Medicine and Biology **58**, 5363–5380 (2013) (cit. on pp. 33, 39, 41, 46, 62–65, 71, 73, 111, 118).

[13] L. Al-Sulaiti, D. Shipley, R. Thomas, A. Kacperek, P. Regan, and H. Palmans, “Water equivalence of various materials for clinical proton dosimetry by experiment and Monte Carlo simulation”, Nuclear Instruments and Methods in Physics Research Section A: Accelerators, Spectrometers, Detectors and Associated Equipment **619**, 344–347 (2010) (cit. on pp. 34, 77, 79, 98, 106, 111).

[14] L. Al-Sulaiti, D. Shipley, R. Thomas, P. Owen, A. Kacperek, P. H. Regan, and H. Palmans, “Water equivalence of some plastic-water phantom materials for clinical proton beam dosimetry”, Applied Radiation and Isotopes: Including Data, Instrumentation and Methods for Use in Agriculture, Industry and Medicine **70**, 1052–1057 (2012) (cit. on pp. 34, 77, 97, 98, 106, 111).

[15] A. Lühr, D. C. Hansen, N. Sobolevsky, H. Palmans, S. Rossomme, and N. Bassler, “Fluence correction factors and stopping power ratios for clinical ion beams”, Acta Oncologica **50**, 797–805 (2011) (cit. on pp. 34, 38, 55, 62, 65, 77, 98, 106, 111, 121).

[16] A. Ferrari, P. R. Sala, A. Fassò, and J. Ranft, “FLUKA: a multi-particle transport code”, in CERN 2005-10, INFN/TC 05/11, SLAC-R-773 (2005) (cit. on pp. 38, 39, 44, 46, 60, 70, 93, 94, 115, 125, 129, 131, 132).

[17] T. Böhlen, F. Cerutti, M. Chin, A. Fassò, A. Ferrari, P. Ortega, A. Mairani, P. Sala, G. Smirnov, and V. Vlachoudis, “The FLUKA Code: Developments and Challenges for High Energy and Medical Applications”, Nuclear Data Sheets **120**, 211–214 (2014) (cit. on pp. 38, 39, 44, 46, 60, 70, 93, 94, 115, 125, 129, 131, 132).

[18]H. Palmans, M. Bailey, S. Duane, D. Shipley, and R. Thomas, “Development of a primary standard level proton calorimeter at NPL”, Radiotherapy and Oncology **84 (Suppl. 1) S135** (2007) (cit. on pp. 38, 62).

[19]H. Palmans, R. Thomas, M. Simon, S. Duane, A. Kacperek, A. DuSautoy, and F. Verhaegen, “A small-body portable graphite calorimeter for dosimetry in low-energy clinical proton beams”, Physics in Medicine and Biology **49**, 3737–49 (2004) (cit. on pp. 38, 62).

[20] AAPM, “Protocol for heavy charged-particle therapy beam dosimetry; a report of Task group 20 Radiation Therapy Committee, American Association of Physicists in Medicine Report 16”, American Institute of Physics (1986) (cit. on pp. 38, 62).

[21]S. Vynckier, D. E. Bonnett, and D. T. L. Jones, “Code of practice for clinical proton dosimetry”, Radiotherapy and Oncology **20**, 53–63 (1991) (cit. on pp. 38, 62, 110).

[22]S. Vynckier, D. E. Bonnett, and D. T. Jones, “Supplement to the code of practice for clinical proton dosimetry”, Radiotherapy and Oncology **32**, 174–179 (1994) (cit. on pp. 38, 62).

[23] ICRU, *Clinical proton dosimetry part I: beam production, beam delivery and measurement of absorbed dose Report 59* (IAEA TRS-398, 1998) (cit. on pp. 38, 62).

[24]H. Palmans, L. Al-Sulaiti, P. Andreo, D. Shipley, A. Lühr, N. Bassler, J. Martinkovič, J. Dobrovodský, S. Rossomme, R. a. S. Thomas, and A. Kacperek, “Fluence correction factors for graphite calorimetry in a low-energy clinical proton beam: I. Analytical and Monte Carlo simulations”, Physics in Medicine and Biology **58**, 3481–3499 (2013) (cit. on pp. 39–41, 43, 44, 54, 58, 62–64, 72, 77, 79, 83, 89, 90, 97, 105, 111, 117, 118).

[25]K. R. Kase, G. J. Adler, and B. E. Bjärngard, “Comparisons of electron beam dose measurements in water and polystyrene using various dosimeters”, Medical Physics **9**, 13–19 (1982) (cit. on p. 39).

[26]D. I. Thwaites, “Measurements of ionisation in water, polystyrene and a ’solid water’ phantom material for electron beams”, Physics in Medicine and Biology **30**, 41–53 (1985) (cit. on pp. 39, 111).

[27] ICRU, *Stopping Powers and Ranges for Protons and Alpha Particles Report 49* (Bethesda, MD: ICRU, 1993) (cit. on pp. 41, 43, 44, 49, 79, 93, 95, 116).

[28]C. Gomà, P. Andreo, and J. Sempau, “Spencer-Attix water/medium stopping-power ratios for the dosimetry of proton pencil beams”, Physics in Medicine and Biology **58**, 2509–2522 (2013) (cit. on p. 41).

[29]D. T. L. Jones, “The w-value in air for proton therapy beams”, Radiation Physics and Chemistry **75**, 541–550 (2006) (cit. on p. 43).

[30] G. Grosswendt, and W. Y. Baek, “W values and radial dose distributions for protons in TE-gas and air at energies up to 500 MeV”, Physics in Medicine and Biology **43**, 325–337 (1998) (cit. on p. 43).

[31] I. Rinaldi, A. Ferrari, A. Mairani, H. Paganetti, K. Parodi, and P. Sala, “An integral test of FLUKA nuclear models with 160 MeV proton beams in multi-layer Faraday cups”, eng, Physics in Medicine and Biology **56**, 4001–4011 (2011) (cit. on p. 46).

[32] T. T. Böhlen, F. Cerutti, M. Dosanjh, A. Ferrari, I. Gudowska, A. Mairani, and J. M. Quesada, “Benchmarking nuclear models of FLUKA and GEANT4 for carbon ion therapy”, Physics in Medicine and Biology **55**, 5833 (2010) (cit. on pp. 46, 70, 100, 116).

[33] D. E. Bonnett, A. Kacperek, M. A. Sheen, R. Goodall, and T. E. Saxton, “The 62 MeV proton beam for the treatment of ocular melanoma at Clatterbridge”, The British Journal of Radiology **66**, 907–914 (1993) (cit. on pp. 46, 93).

[34] C. Baker, D. Shipley, H. Palmans, and A. Kacperek, “Monte carlo modelling of a clinical proton beam-line for the treatment of ocular tumours”, Nuclear Instruments and Methods in Physics Research A: Accelerators, Spectrometers, Detectors and Associated Equipment **562**, 1005–1008 (2006) (cit. on pp. 46, 93).

[35] A. Kacperek, “Protontherapy of eye tumours in the UK: a review of treatment at Clatterbridge”, Applied Radiation and Isotopes: Including Data, Instrumentation and Methods for Use in Agriculture, Industry and Medicine **67**, 378–386 (2009) (cit. on pp. 46, 48, 92, 93, 144).

[36] ISO, *Guide to the Expression of Uncertainty in Measurement* (International Organization for Standardization (ISO), Geneva, 1995) (cit. on pp. 48, 116).

[37] ICRU, *Nuclear Data for Neutron and Proton Radiotherapy and for radiation Protection Report 63* (Bethesda, MD: ICRU, 2000) (cit. on pp. 49, 55, 80, 82, 83, 85, 98, 100).

[38] M. Schippers, *Proton beam production and dose delivery techniques - Principles and practice of proton beam therapy (AAPM 2015 Summer School)*, edited by I. J. Das, and H. Paganetti, (Madison WI, USA: Medical Physics Publishing, 2015) (cit. on p. 58).

[39] H. J. Brede, K.-D. Greif, O. Hecker, P. Heeg, J. Heese, D. T. L. Jones, H. Kluge, and D. Schardt, “Absorbed dose to water determination with ionization chamber dosimetry and calorimetry in restricted neutron, photon, proton and heavy-ion radiation fields”, Physics in Medicine and Biology **51**, 3667–3682 (2006) (cit. on p. 62).

[40] M. Sakama, T. Kanai, A. Fukumura, and K. Abe, "Evaluation of w values for carbon beams in air, using a graphite calorimeter", Physics in Medicine and Biology **54**, 1111–1130 (2009) (cit. on p. 62).

[41] J. Medin, "Implementation of water calorimetry in a 180 MeV scanned pulsed proton beam including an experimental determination of kQ for a Farmer chamber", Physics in Medicine and Biology **55**, 3287–3298 (2010) (cit. on p. 62).

[42] A. Sarfehnia, B. Clasie, E. Chung, H. M. Lu, J. Flanz, E. Cascio, M. Engelsman, H. Paganetti, and J. Seuntjens, "Direct absorbed dose to water determination based on water calorimetry in scanning proton beam delivery", Medical Physics **37**, 3541–3550 (2010) (cit. on p. 62).

[43] U. Schneider, P. Pemler, J. Besserer, M. Dellert, M. Moosburger, J. d. Boer, E. Pedroni, and T. Boehringer, "The water equivalence of solid materials used for dosimetry with small proton beams", Medical Physics **29**, 2946–2951 (2002) (cit. on p. 62).

[44] A. Lourenço, N. Wellock, R. Thomas, M. Homer, H. Bouchard, T. Kanai, N. MacDougall, G. Royle, and H. Palmans, "Theoretical and experimental characterization of novel water-equivalent plastics in clinical high-energy carbon-ion beams", Physics in Medicine and Biology **(in press)** (2016) (cit. on pp. 62, 70, 106).

[45] H. Paganetti, "Dose to water versus dose to medium in proton beam therapy", Physics in Medicine and Biology **54**, 4399–4421 (2009) (cit. on pp. 63, 111).

[46] E. Haettner, H. Iwase, M. Krämer, G. Kraft, and D. Schardt, "Experimental study of nuclear fragmentation of 200 and 400 MeV/u (12)C ions in water for applications in particle therapy", Physics in Medicine and Biology **58**, 8265–8279 (2013) (cit. on pp. 67, 71, 106, 118).

[47] M. Komori, T. Furukawa, T. Kanai, and K. Noda, "Optimization of Spiral-Wobbler System for Heavy-Ion Radiotherapy", Japanese Journal of Applied Physics **43**, 6463–6467 (2004) (cit. on pp. 69, 114).

[48] S. Yonai, N. Kanematsu, M. Komori, T. Kanai, Y. Takei, O. Takahashi, Y. Isobe, M. Tashiro, H. Koikegami, and H. Tomita, "Evaluation of beam wobbling methods for heavy-ion radiotherapy", Medical Physics **35**, 927–938 (2008) (cit. on pp. 69, 114).

[49] T. Ohno, T. Kanai, S. Yamada, K. Yusa, M. Tashiro, H. Shimada, K. Torikai, Y. Yoshida, Y. Kitada, H. Katoh, T. Ishii, and T. Nakano, "Carbon Ion Radiotherapy at the Gunma University Heavy Ion Medical Center: New Facility Set-up", Cancers **3**, 4046–4060 (2011) (cit. on pp. 69, 114).

[50] ICRU, *Stopping of Ions Heavier Than Helium ICRU Report 73* (Bethesda, MD: ICRU, 2005) (cit. on pp. 70, 117).

[51] J. Kempe, I. Gudowska, and A. Brahme, "Depth absorbed dose and LET distributions of therapeutic 1h, 4he, 7li, and 12c beams", Medical Physics **34**, 183–192 (2007) (cit. on pp. 71, 118).

[52] M. Hultqvist, M. Lazzeroni, A. Botvina, I. Gudowska, N. Sobolevsky, and A. Brahme, "Evaluation of nuclear reaction cross-sections and fragment yields in carbon beams using the SHIELD-HIT Monte Carlo code. Comparison with experiments", Physics in Medicine and Biology **57**, 4369–4385 (2012) (cit. on p. 72).

[53] M. F. Moyers, D. W. Miller, J. V. Siebers, R. Galindo, S. Sun, M. Sardesai, and L. Chan, "Water equivalence of various materials for 155 to 250 MeV protons", Medical Physics **19**, 829 (1992) (cit. on p. 77).

[54] M. F. Moyers, *The Modern Technology of Radiation Oncology: A Compendium for Medical Physicists and Radiation Oncologists*, edited by I. J. Dyk, (Wisconsin: Medical Physics Publishing, 1999) (cit. on p. 77).

[55] R. Zhang, P. J. Taddei, M. M. Fitzek, and W. D. Newhauser, "Water equivalent thickness values of materials used in beams of protons, helium, carbon and iron ions", Physics in medicine and biology **55**, 2481–2493 (2010) (cit. on pp. 77, 110).

[56] D. R. White, R. J. Martin, and R. Darlison, "Epoxy resin based tissue substitutes", The British Journal of Radiology **50**, 814–821 (1977) (cit. on pp. 77, 85, 91, 114).

[57] D. R. White, "Tissue substitutes in experimental radiation physics", Medical Physics **5**, 467–479 (1978) (cit. on pp. 77, 85, 91, 114).

[58] D. R. White, and A. K. Tucker, "A test object for assessing image quality in mammography", The British Journal of Radiology **53**, 331–335 (1980) (cit. on pp. 77, 85, 91, 114).

[59] C. Constantinou, F. H. Attix, and B. R. Paliwal, "A solid water phantom material for radiotherapy x-ray and gamma-ray beam calibrations", Medical Physics **9**, 436–441 (1982) (cit. on pp. 77, 85, 91, 114).

[60] ICRU, *Stopping Powers for Electrons and Positions Report 37* (Bethesda, MD: ICRU, 1984) (cit. on pp. 79, 82, 93, 95, 116).

[61] F. H. Attix, *Introduction to Radiological Physics and Radiation Dosimetry* (Wiley, 1986) (cit. on p. 79).

[62] A. Ferrari, and P. Sala, "The Physics of High Energy Reactions", in, Vol. 2 (1998) (cit. on pp. 83, 94, 100).

[63] G. Battistoni, F. Cerutti, R. Engel, A. Fassò, A. Ferrari, E. Gadioli, M. V. Garzelli, J. Ranft, S. Roesler, and P. R. Sala, "Recent developments in the FLUKA nuclear reaction models", in Proc. 11th Int. Conf. on Nucl. React. Mech. (2006), pp. 483–95 (cit. on pp. 83, 94, 100).

[64] Emilio Segre (Ed.), *Experimental Nuclear Physics Vol 1* (John Wiley, 1953) (cit. on p. 87).

[65] B. Gottschalk, "On the scattering power of radiotherapy protons", Medical Physics **37**, 352–367 (2010) (cit. on pp. 88, 95).

[66] S. Agostinelli, J. Allison, K. Amako, J. Apostolakis, H. Araujo, P. Arce, M. Asai, D. Axen, S. Banerjee, G. Barrand, F. Behner, L. Bellagamba, J. Boudreau, L. Broglia, A. Brunengo, et al., "Geant4—a simulation toolkit", Nuclear Instruments and Methods in Physics Research Section A: Accelerators, Spectrometers, Detectors and Associated Equipment **506**, 250–303 (2003) (cit. on p. 94).

[67] F. Fracchiolla, S. Lorentini, L. Widesott, and M. Schwarz, "Characterization and validation of a Monte Carlo code for independent dose calculation in proton therapy treatments with pencil beam scanning", Physics in Medicine and Biology **60**, 8601–8619 (2015) (cit. on p. 94).

[68] G. a. P. Cirrone, "Hadrontherapy. A Geant4-based tool for proton/ion-therapy studies", Prog. Nucl. Sci. Technol. **2**, 207–12 (2011) (cit. on p. 94).

[69] G. Folger, V. N. Ivanchenko, and J. P. Wellisch, "The Binary Cascade", The European Physical Journal A - Hadrons and Nuclei **21**, 407–417 (2004) (cit. on pp. 94, 100).

[70] P. R. Almond, P. Andreo, O. Mattsson, A. E. Nahum, and M. Roos, *The use of plane-parallel ionization chambers in high-energy electron and photon beams. An international Code of Practice for dosimetry IAEA Technical Report Series TRS-381* (IAEA, Vienna, 1997) (cit. on p. 95).

[71] C. Robert, G. Dedes, G. Battistoni, T. T. Böhlen, I. Buvat, F. Cerutti, M. P. W. Chin, A. Ferrari, P. Gueth, C. Kurz, L. Lestand, A. Mairani, G. Montarou, R. Nicolini, P. G. Ortega, et al., "Distributions of secondary particles in proton and carbon-ion therapy: a comparison between GATE/Geant4 and FLUKA Monte Carlo codes", Physics in Medicine and Biology **58**, 2879–2899 (2013) (cit. on p. 100).

[72] F. S. Rasouli, S. F. Masoudi, and D. Jette, "Technical Note: On the proton range and nuclear interactions in compounds and mixtures", Medical Physics **42**, 2364–2367 (2015) (cit. on p. 101).

[73] J. F. Janni, "Energy loss, range, path length, time-of-flight, straggling, multiple scattering, and nuclear interaction probability", Atomic Data and Nuclear Data Tables **27**, 341–529 (1982) (cit. on pp. 102, 107).

[74] M. F. Moyers, A. S. Vatnitsky, and S. M. Vatnitsky, "Factors for converting dose measured in polystyrene phantoms to dose reported in water phantoms for incident proton beamsa)", Medical Physics **38**, 5799–5806 (2011) (cit. on pp. 103, 108).

[75]N. Kanematsu, Y. Koba, and R. Ogata, “Evaluation of plastic materials for range shifting, range compensation, and solid-phantom dosimetry in carbon-ion radiotherapy”, Medical Physics **40**, 041724 (2013) (cit. on p. 110).

[76]H. Palmans, and F. Verhaegen, “Assigning nonelastic nuclear interaction cross sections to Hounsfield units for Monte Carlo treatment planning of proton beams”, Physics in Medicine and Biology **50**, 991–1000 (2005) (cit. on p. 111).

[77]T. Inaniwa, N. Kanematsu, Y. Hara, and T. Furukawa, “Nuclear-interaction correction of integrated depth dose in carbon-ion radiotherapy treatment planning”, Physics in Medicine and Biology **60**, 421–435 (2015) (cit. on p. 111).

[78]T. Inaniwa, N. Kanematsu, H. Tsuji, and T. Kamada, “Influence of nuclear interactions in body tissues on tumor dose in carbon-ion radiotherapy”, Medical Physics **42**, 7132–7137 (2015) (cit. on p. 111).

[79]N. Kanematsu, Y. Koba, R. Ogata, and T. Himukai, “Influence of nuclear interactions in polyethylene range compensators for carbon-ion radiotherapya)”, Medical Physics **41**, 071704 (2014) (cit. on p. 111).

[80]H. Palmans, and F. Verhaegen, “Calculated depth dose distributions for proton beams in some low-Z materials”, Physics in Medicine and Biology **42**, 1175–1183 (1997) (cit. on p. 111).

[81]F. M. Khan, K. P. Doppke, K. R. Hogstrom, G. J. Kutcher, R. Nath, S. C. Prasad, J. A. Purdy, M. Rozenfeld, and B. L. Werner, “Clinical electron-beam dosimetry: report of AAPM Radiation Therapy Committee Task Group No. 25”, Medical Physics **18**, 73–109 (1991) (cit. on p. 111).

[82]M. R. McEwen, and A. R. DuSautoy, “Characterization of the water-equivalent material WTe for use in electron beam dosimetry”, Physics in Medicine and Biology **48**, 1885–1893 (2003) (cit. on p. 111).

[83]J. Seuntjens, M. Olivares, M. Evans, and E. Podgorsak, “Absorbed dose to water reference dosimetry using solid phantoms in the context of absorbed-dose protocols”, Medical Physics **32**, 2945–2953 (2005) (cit. on p. 111).

[84]A. Lourenço, R. Thomas, H. Bouchard, A. Kacperek, V. Vondracek, G. Royle, and H. Palmans, “Experimental and Monte Carlo studies of fluence corrections for graphite calorimetry in low- and high-energy clinical proton beams”, Medical Physics **43**, 4122–4132 (2016) (cit. on p. 113).

[85]E. Sterpin, J. Sorriaux, K. Souris, S. Vynckier, and H. Bouchard, “A Fano cavity test for Monte Carlo proton transport algorithms”, Medical Physics **41**, 011706 (2014) (cit. on pp. 124, 125, 127).

[86]D. W. O. Rogers, “Fifty years of Monte Carlo simulations for medical physics”, Physics in Medicine and Biology **51**, R287 (2006) (cit. on p. 124).

[87] U. Fano, “Note on the Bragg-Gray Cavity Principle for Measuring Energy Dissipation”, Radiation Research **1**, 237–240 (1954) (cit. on p. 124).

[88] I. Kawrakow, “Accurate condensed history Monte Carlo simulation of electron transport. I. EGSnrc, the new EGS4 version”, Medical Physics **27**, 485–498 (2000) (cit. on p. 124).

[89] B. R. B. Walters, and I. Kawrakow, “Technical note: overprediction of dose with default PRESTA-I boundary crossing in DOSXYZnrc and BEAMnrc”, Medical Physics **34**, 647–650 (2007) (cit. on p. 124).

[90] I. Kawrakow, “Accurate condensed history Monte Carlo simulation of electron transport. II. Application to ion chamber response simulations”, Medical Physics **27**, 499–513 (2000) (cit. on p. 124).

[91] J. Sempau, P. Andreo, J. Aldana, J. Mazurier, and F. Salvat, “Electron beam quality correction factors for plane-parallel ionization chambers: Monte Carlo calculations using the PENELOPE system”, Physics in Medicine and Biology **49**, 4427–4444 (2004) (cit. on p. 124).

[92] C.-Y. Yi, S.-H. Hah, and M. S. Yeom, “Monte Carlo calculation of the ionization chamber response to 60co beam using PENELOPE”, Medical Physics **33**, 1213–1221 (2006) (cit. on p. 124).

[93] E. Poon, J. Seuntjens, and F. Verhaegen, “Consistency test of the electron transport algorithm in the GEANT4 Monte Carlo code”, Physics in Medicine and Biology **50**, 681–694 (2005) (cit. on pp. 124, 127).

[94] K. Zink, and J. Wulff, “Positioning of a plane-parallel ionization chamber in clinical electron beams and the impact on perturbation factors”, Physics in Medicine and Biology **54**, 2421–2435 (2009) (cit. on p. 128).

[95] M. Bailey, D. R. Shipley, and J. W. Manning, “Roos and NACP-02 ion chamber perturbations and water-air stopping-power ratios for clinical electron beams for energies from 4 to 22 MeV”, Physics in Medicine and Biology **60**, 1087 (2015) (cit. on p. 128).

[96] J. Medin, and P. Andreo, “Monte Carlo calculated stopping-power ratios, water/air, for clinical proton dosimetry (50 - 250 MeV)”, Physics in Medicine and Biology **42**, 89 (1997) (cit. on p. 132).